Modeling photonic effects induced by dynamic modulation of plasmonic resonances

Galaad Altares Menendez

Thesis presented in fulfilment of the requirements for the degree of
Doctor of Science

Thesis supervisor
Bjorn MAES

Supervisor

Prof. Bjorn Maes   Micro- and Nanophotonic Materials Group, University of Mons

Jury members

Prof. Michel Voué   Materials Physics and Optics Unit, University of Mons

Prof. Marc Wuilpart   Electromagnetism and Telecommunication, University of Mons

Dr. Gilles Rosolen   Micro- and Nanophotonic Materials Group, University of Mons

Prof. Bart Kuyken   INTEC Photonics Research Group, Ghent University

Prof. Branko Kolaric   Photonics Center, Institute of Physics, University of Belgrade

University of Mons
Faculty of Science

Micro- and Nanophotonic Materials Group (MMNP)
Place du Parc 20
7000 Mons
Belgium

Tel.: +32-65/37.33.85
http://www.umons.ac.be/nanophot

Contents

Acknowledgements

I would like to thank everyone who contributed to this thesis. I a really grateful for the support I had during the research, writing and defense of this work.

First of all I thank my supervisor Prof. Bjorn Maes for giving me the opportunity to pursue a PhD thesis in his group. I also thank him for the scientific advice he has always provided, for his guidance on the scientific literature, but also for his close attention to my progress through regular meetings. I also thank him for encouraging me to attend international conferences, and for allowing me to follow courses not directly related to my PhD work.

I also thank all the jury members that gave the time and effort to read this PhD thesis and to attend the PhD defense. I am thankful for the scientific discussion we had and for the advice concerning this manuscript. I especially thank Prof. Michel Voué and Prof. Marc Wuilpart for following the progress of my research as members of the Support Committee.

I would also like to thank all the friends and colleagues I worked with: Muluneh Abebe for honing my password resetting skills, Dr. Nicolas Rivolta for the door label of my office, Dr. Fabio Vaianella for his bad cards advice, Dr. Gilles Rosolen for reminding me to drink enough coffee, and Corentin Guyot for initiating chips Friday. I thank them for the support they always gave me and for their scientific advice. I especially thank Dr. Gilles Rosolen for his encouragements and for the scientific discussions we often had and that helped me more than he thinks.

My thanks are not restricted to the colleagues of my office: I also thank people from across the hall with who we shared a lot of good moments and sometimes a few drinks. The friendly atmosphere in the building made working here a pleasure.

Enfin, je remercie ma famille qui m'a toujours supporté quels que soient mes choix, et qui a toujours cru en moi. Je remercie aussi Dilan qui m'a encouragé dans les bons moments comme dans les plus difficiles.

Summary

In recent years, time-dependent materials have emerged as a powerful and versatile platform to achieve a wide variety of photonic effects, from frequency conversion and optical isolation to more exotic behaviours such as topological protection. The goal of this thesis is to study and combine time-dependent photonics and plasmonics. To this end, we employ analytical techniques, numerical tools and simulations to solve time-dependent systems.

First, we study frequency combs produced by a time-modulated graphene plasmonic cavity. We show that the combs are very efficiently produced by this setup, and can be tailored by the graphene and modulation parameters. Then we study the behaviour of propagating plasmons when the graphene properties suddenly change in time. We show that an incident plasmon creates a reflected and a transmitted plasmon, and that while their propagation constant is conserved, their frequency changes. We study this conversion for several temporal perturbations and validate our results via time domain finite-element simulations. We then extend the study of time-modulated resonances by considering a system with two coupled cavities. We show that a periodically modulated system supports so-called Floquet modes. We study these modes with analytical and numerical techniques and discuss how one can optimize the intermodal interaction to achieve selective frequency conversion. Finally, we examine in more detail the decay mechanisms of the Floquet modes and show that they can lead to a new type of bound states in the continuum. These states are modes that, even if coupled to a continuum of radiation channels, cannot leak because of destructive interference. We show that such modes can persist in a time-modulated two-cavity system, when the resonances are modulated in the correct way.

1

Introduction

1.1 Context

Now more than ever, we live in a world of information and technology. There has never been so much data generated by mankind, and transferred across the globe. Tremendous progress has been achieved in communication technologies: we have come from the first transatlantic cable laid in 1856, which could transfer a message in more than 17 hours, to fiber optic cables that reach speeds of more than one hundred terabits per second. Furthermore, the processing of data has also come a long way. Since 1965, Moore's law has correctly described the evolution of the density of transistors in integrated circuits. However, by its nature, an exponential law cannot last forever, especially because of the fundamental limit of electronics: the atomic scale [1].

While technological progress has without question changed humanity forever, numerous challenges are emerging. For example the power consumption of telecommunication systems is now requiring a significant amount of the global electricity production [2], and is expected to require even more energy in the years to come. To counter that augmentation, it is essential to develop new telecommunication technologies. To this end, new physical effects are investigated, to achieve functions such as frequency conversion, modulation and optical isolation.

Modulators are widely used in fiber optic communications, especially in optical interconnects that link two electronic circuits. In these devices, an electronic signal needs to be converted to an optical signal, generally by using and electro-optic modulator. These modulators usually use time-dependent properties to modulate a light beam. In telecommunication technology it is often important to achieve frequency conversion, amongst others for wavelength-division multiplexing, which sends multiple signals at different frequencies through the same optical fiber. Usually, frequency conversion is achieved with non-linear materials. However, this conversion is dependent on the light intensity and travelling distance and is difficult to implement. Another way to realize frequency conversion is to use time-modulated materials.

In optical systems it is extremely important to prevent light from reflecting back to the source. For example, a light beam reflected on an optical element in an optical setup can generate a feedback and perturb the laser cavity. To prevent this from happening, it is necessary to use a device that allows light to pass in only one direction. This type of device is called an optical isolator [3]. To build an optical isolator, it is required to break time-symmetry, either by using magneto-optical properties, non-linear materials or time dependent effects. All these technological challenges show that there is a common class of effects that can be a part of the solution: time-dependent materials [4].

Another field of research, plasmonics, has known a rapid emergence during the last decade. Plasmonics studies surface plasmons, quasi-particles created by the interaction of light and conduction electrons at the surface of a metal [5]. Plasmonic properties of materials were used as early as Roman times [6] to achieve stained glass colors. Surface plasmons exhibit interesting properties such as high confinement and strong field enhancement. These properties have found applications e.g. in biosensors [7], where they allow to measure adsorption of a material onto a metal surface. Surface plasmons can be employed as guided modes, like photonic waveguide modes, and it was envisioned that they could be used to create plasmonic circuits [8], capable of manipulating light at a deep subwavelength scale. However, losses in metals severely limit the practical use of such devices.

Recently, the experimental realization of graphene has opened new possibilities for the plasmonics community [9]. Graphene is a 2D crystal of carbon atoms that behaves as a metal for visible to far-infrared light. As such, it supports plasmonic modes that exhibit amazing properties such as an extreme confinement of the modes around the graphene sheet and high field enhancement. One striking property of graphene is its tunability: unlike metals, when carriers are injected in graphene, its conductivity properties drastically change. Graphene plasmonics is thus an ideal platform for tunable devices, and to achieve time-dependent effects.

In this thesis, the ambition is to combine the fields of plasmonics and time-dependent photonics. To this end, the versatile platform of graphene plasmonics is ideal. The high field confinement and tunability of graphene plasmons promise to enhance dynamic effects of time-modulated structures. We study the interaction of light, surface plasmons and time modulation with analytical models and rigorous numerical simulations. In the end, the systems we study throughout this work can be generalized to other kinds of time-modulated resonances.

1.2   Outline

This work is structured as follows. In Chapter 2, we give a brief overview of photonic systems using time-modulated materials. We essentially introduce three kinds of effects: frequency conversion, optical isolation and topological effects. Although these three subcategories are not independent (for example topological systems usually have optical isolation properties), they give an intuitive categorization of time-dependent effects already studied in the literature.

In Chapter 3, we introduce the general properties of graphene. We describe its crystal structure and give the expressions describing its conductivity. The latter is an essential concept since it governs the interaction between light and graphene, and is responsible for the existence of graphene plasmonic modes. We show that the conductivity can be described by a Drude model in a particular regime. We then describe the different methods to affect graphene conductivity. First we introduce chemical doping, where carbon atoms in the graphene crystal are replaced by other chemical species. The second method we mention is the electric field effect, where a gating voltage is used to modify the graphene Fermi level. The last technique we consider is the optical pumping, that uses a light beam to excite electrons from the valence band to the conduction band, modifying the occupation of electronic states in graphene and changing its optical properties. We then discuss fabrication issues, both for graphene sheets and patterned nanostructures, such as graphene nanoribbons.

Chapter 4 is a brief introduction to plasmonics. We start by deriving the Drude model for metals as it is needed to describe plasmonic modes. Then we describe surface plasmons at a dielectric-metal interface to describe the optical response of metals. This allows to find the dispersion relation linking the frequency and wavevector of metal surface plasmons, as well as their mode profile. We then investigate graphene plasmons and give their dispersion relation and mode profiles. While these two types of modes cannot be directly excited by plane waves (their dispersion lies below the light line), graphene plasmons are much more confined than metal plasmons. The dispersion is also a function of the Fermi level, which implies that the properties of propagation and the mode profiles can be changed via the Fermi level.

In Chapter 5 we discuss various methods and concepts used throughout the thesis. We start by introducing the Coupled Mode Theory (CMT) framework. CMT is a powerful tool that describes the evolution of single or multimode cavities coupled to ports. These cavities represent the resonant modes of a physical system. In photonics, these cavities often describe a resonator (a photonic crystal cavity or a ring resonator for example) or a plasmonic resonance. We discuss the conditions that the CMT system must obey, such as energy conservation and time reversal symmetry, and the constraints that they impose on the CMT parameters. Then we discuss Fano resonances, that occur when a resonant mode interacts with a continuum of states, and use the CMT framework to derive the well known Fano lineshape. We finish the chapter by describing a perturbation method used to investigate the eigenvalues of an Hamiltonian in a time-periodic potential.

In Chapter 6, we study the interplay of time modulation and plasmonic resonances in graphene gratings to efficiently generate frequency combs (work published

in [10]). By using rigorous simulations and a coupled-mode theory model, we show that the combs can be strongly tailored via both the grating and time modulation properties, and can range from the mid-infrared to far-infrared. The grating properties, via the resonance lifetime, strongly influence the conversion efficiency, while the temporal modulation defines the comb's frequency spacing and shape. We examine in detail the dynamics of this interplay between cavity and modulation. With the grating mechanism, a similar frequency comb generation is obtained with a modulation amplitude that is three orders of magnitude smaller than in the planar case.

We then study the behaviour of graphene plasmons incident on a time boundary in Chapter 7. A sudden change of material properties induces a special type of reflection and refraction at a temporal discontinuity (work published in [11]). We study the interaction of graphene plasmons with single and double temporal discontinuities or shocks, leading to controlled in-plane scattering. We analytically determine the Fresnel-like coefficients for graphene plasmons at these boundaries, and validate our results by rigorous numerical simulations. Temporally controlled doping of two-dimensional materials such as graphene thus leads to a new mechanism for planar and compact plasmonic devices.

In Chapter 8, we extend on the work presented in Chapter 6. We present a mechanism to achieve efficient and selective frequency conversion using a system of two time-modulated cavities. This setup allows to fine-tune the conversion process by controlling important parameters such as the inter-cavity coupling and the external excitation frequency. Both symmetric and asymmetric (up- or down-conversion) outputs can be targeted at will. We describe the processes extensively, with for example a leading role for the dynamic modes of the coupled system, the Floquet modes.

Finally in Chapter 9, we study the decay mechanisms of Floquet modes described in the previous chapter. We start by showing that a system of two cavities exhibit bound states in the continuum, modes that even though coupled to radiation channels do not emit radiation because of the interference between the cavity modes. We then show that the Floquet modes can also be bound states even in the presence of time modulation. Such a mode, once excited will stay trapped inside the cavity. Other Floquet modes however can still radiate through the output ports.

1.3   Publications

Publications in international journals

In this section we list all the contributions in international journals published or submitted during the PhD grant:

- G. Altares Menendez, G. Rosolen, B. Maes, "Graphene plasmons embedded in a gain medium: layer and ribbon plasmons", *Journal of Optics*, 18, 12, 125004, 2016.

- G. Altares Menendez, B. Maes, "Frequency comb generation using plasmonic

resonances in a time-dependent graphene ribbon array", *Physical Review B*, 95, 144307, 2017.

- G. Altares Menendez, B. Maes, "Time reflection and refraction of graphene plasmons at a temporal discontinuity" *Optics Letters*, 42, 23, 5006-5009, 308602, 2017.

- G. Altares Menendez, B. Maes, "Selective Frequency Conversion With Coupled Time-Modulated Cavities", *Physical Review B*, 100, 014306, 2019.

Contributions to international conferences

In this section we list contributions to conferences during the PhD grant:

- G. Altares Menendez, G. Rosolen, B. Maes, "Graphene plasmons embedded in a gain medium" in "20th Annual Symposium of the IEEE Photonics Benelux Chapter", Brussels, Belgium, 2016.

- G. Altares Menendez, B. Maes, "Frequency comb generation in a time-dependent graphene ribbon lattice" in "Meta '16 - 7th International Conference on Metamaterials, Photonic Crystals and Plasmonics", Malaga, Spain, 2016.

- G. Altares Menendez, B. Maes, "Frequency comb generation in a time-dependent graphene ribbon array" in "21st Annual Symposium of the IEEE Photonics Society Benelux Chapter", Ghent, Belgium, 2016.

- G. Altares Menendez, B. Maes, "Time-modulated graphene arrays for efficient frequency comb generation with plasmonic resonances" in "International Workshop on Optical Wave and Waveguide Theory and Numerical Modelling", Eindhoven, The Netherlands, 2017.

- G. Altares Menendez, B. Maes, "Time reflection and time refraction of graphene plasmons" in "The 11th International Congress on Engineered Material Platforms for Novel Wave Phenomena", Marseille, France, 2017.

- G. Altares Menendez, B. Maes, "Tunable frequency conversion with coupled time-modulated resonances" in "The 15th international conference on near-field optics, nanophotonics and related techniques", P3A3, Troyes, France, 2017.

- G. Altares Menendez, B. Maes, "Tunable frequency conversion with time-modulated cavities" in "12th International Congress on Artificial Materials for Novel Wave Phenomena - Metamaterials 2018", Espoo, Finland, 2018.

- G. Altares Menendez, B. Maes, "Efficient frequency conversion via Floquet modes in time-modulated cavities" in "23rd Annual Symposium of the IEEE Photonics Benelux Chapter", Brussels, 2018.

2

Time dependent photonics

In this chapter we briefly review three classes of phenomena induced by time modulation: frequency conversion, optical isolation and topological effects. While these effects are not new, their realization using time-modulated materials has certainly attracted much attention during the last few years. More specifically, the three phenomena previously required the use of non-linear materials, or magnetic fields. However, there are significant drawbacks to use non-linear materials (dependence on the field intensity) and magnetic materials (difficulty to integrate on chip). Time modulation therefore offers a new promising platform to implement these effects.

2.1 Frequency conversion

Frequency conversion is crucial for optical systems: it is possible to greatly enhance the bandwidth of optical interconnect architectures by using wavelength-division multiplexing. This application requires to perform frequency conversion at a chip scale, which is challenging. Typically, frequency conversion is performed with non-linear processes, using highly non-linear crystals, and depends on the light intensity and travel distance. These limitations render on-chip frequency conversion extremely difficult. However, it has been experimentally demonstrated in silicon waveguides [12] and in micro-rings [13] by using all-optical modulation effects.

A different way to achieve frequency conversion is to dynamically change the material properties. This idea was proposed in photonic crystals: if the crystal is suddenly compressed while light is propagating, the creation of a bandgap causes light to be reflected at a different frequency [14, 15]. Later, it was demonstrated that light trapped in a high-Q cavity can be converted to a different frequency by dynamically changing the cavity resonance frequency [16]. This effect can be achieved in photonic crystals by a change of the index of the material surrounding the cavity, or by applying a mechanical constraint to the photonic crystal [17]. This phenomenon corresponds to the adiabatic tuning of an oscillator. An analogy is often used for this effect: when a guitar string is plucked, it oscillates at the string resonance frequency and produces a corresponding pitch. If the string is shortened while vibrating, the string resonance frequency changes as well as the sound created.

This principle was then used to experimentally achieve frequency conversion of light trapped inside a silicon micro-ring resonator [18] using an electro-optic approach. The refractive index of the silicon ring was changed via the free carrier plasma dispersion effect [19] induced by short optical pulses. The free-carriers reduce the ring refractive index, and both the resonance and light trapped inside it are forced to blue-shift (Figure 2.1, left).

The works cited above mainly focus on the dynamical change of a cavity mode: light is trapped inside a single cavity and is constrained to follow the cavity resonance frequency. However, frequency conversion for propagative modes is also possible: it was shown [20, 21] that slow light in a photonic crystal waveguide can be frequency shifted during its propagation. This shift is achieved by changing the refractive in the silicon parts of the photonic crystal via an intense pump illumination [22].

Using a similar setup, indirect photonic transitions have been demonstrated [23]. This effect combines the frequency conversion in a photonic waveguide described above with a Doppler-like effect. A perturbation propagating through the crystal interacts with the signal and induces a change in frequency and wavevector. These 'indirect' photonic transitions are achieved by temporal and spatial perturbations, respectively. One way to realize this is to use a two step process [24]: first shift the light frequency by generating free-carriers and then change the wave vector at a spatial interface (see Figure 2.1, right).

2.2   Optical isolation

Optical isolators are devices that allow light to pass in one direction, but block it in the opposite direction. Optical isolators are crucial in optical systems where it is important to protect the source from backscattered light. An optical isolator is a device that must break Lorentz reciprocity [3], and possesses an asymmetric scattering matrix (Figure 2.2, top). Note that the scattering matrix links mode amplitudes between them, and not the total power going through different ports. There are three well-known ways of breaking Lorentz reciprocity: magneto-optic materials, non-linear materials and time-dependent materials. It is interesting that non-reciprocal devices can also be used to achieve isolators in other fields of physics, for example in accoustics [25].
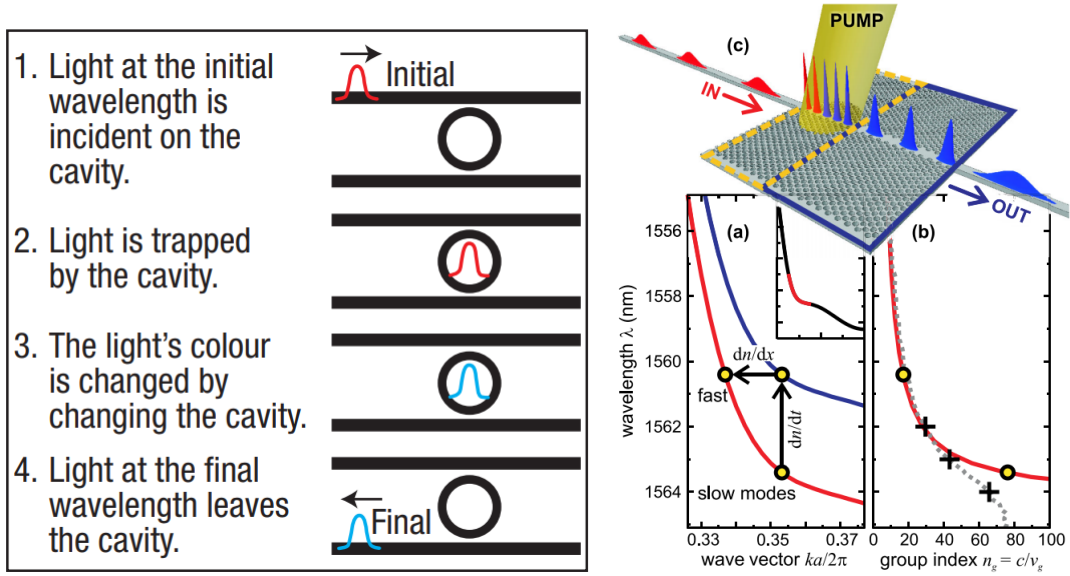
Figure 2.1: Left: Frequency conversion inside a resonator [18]. Right: (a) Two step process of an interband transition: light is frequency shifted by a temporal perturbation and the wavevector changes at a spatial interface. The vertical and horizontal arrows represent the changes induced by temporal and spatial perturbations, respectively. (b) Group index spectra of the photonic crystal. Red lines are simulation results and dashed lines are experimental measurements. (c) Representation of the experimental setup [21].

Because they rely on time-dependent material properties, indirect photonic transitions can be used to achieve optical isolation. When a well-designed spatiotemporal modulation is applied to a waveguide, a mode propagating in one direction will undergo an indirect transition, while the same mode propagating in the other direction will stay unchanged [26, 27]. The modulation of the waveguide relative permittivity is of the form [4]:

$$\varepsilon(x, y, z, t) = \varepsilon_{\text{static}}(x, y) + \Delta\varepsilon(x, y) \cos\left(\Omega t - \beta_m z\right) \tag{2.1}$$

where $\varepsilon_{\text{static}}(x, y)$ is the unperturbed waveguide permittivity profile, $\Delta\varepsilon(x, y)$ is the modulation profile, z is the propagation direction, Ω is the modulation frequency and β_m is the modulation wavenumber. The change in wavevector is achieved by the spatial modulation of the waveguide, while the frequency change is achieved by a temporal modulation. In this case, the time-dependence is essentially a travelling wave modulation.

To achieve an indirect transition, the phase matching conditions $\Omega = \omega_2 - \omega_1$ and $\beta_m = \beta_2 - \beta_1$ must be respected. The mode conversion is only possible in one direction because two modes with an opposite propagation direction have opposite wavenumbers ($-\beta_1$ and $-\beta_2$) and cannot meet the phase matching condition. This process is illustrated in the dispersion diagram of Figure 2.2 (bottom). The converted mode can then be absorbed by a frequency filter since it has a different frequency than the initial mode. This process has been experimentally demonstrated in parallel waveguides [28]. The advantage in that case is that the mode conver-

$$\begin{pmatrix} b_1 \\ b_2 \end{pmatrix} = \begin{bmatrix} 0 & 0 \\ 1 & 0 \end{bmatrix} \begin{pmatrix} a_1 \\ a_2 \end{pmatrix}$$
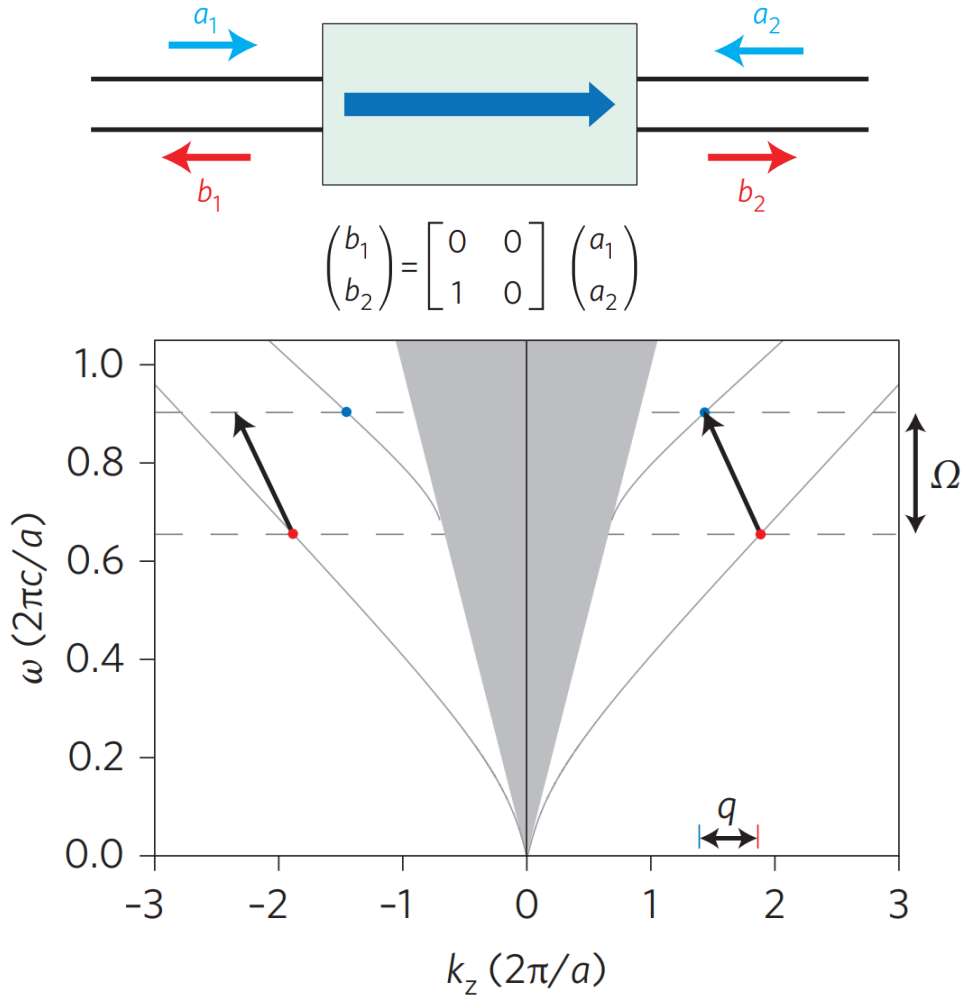
Figure 2.2: Top: Simple isolator between two single-mode waveguides. In this case, the scattering matrix is asymmetric and the device therefore an optical isolator [3]. Bottom: Dispersion diagram of a multimode photonic waveguide. The spatio-temporal modulation induces an indirect transition if the final state is a waveguide mode. This conversion process is relatively broadband because the photonic bands are nearly parallel [26].

sion occurs between the even and odd supermodes, which are separated by only a small frequency and wave number, and therefore require a relatively low modulation frequency (10 GHz) and a small modulation wavenumber to achieve an indirect transition.

This optical isolation process is completely linear and is independent of the phase, intensity and timing of the pulses in the system. In contrast, non-linear isolators only work at higher power [29, 30], and cannot provide complete optical isolation [31]. This setup has also the advantage of being easier to integrate on-chip: a traditional way to achieve optical isolation is to use magneto-optical effects, but these devices are usually bulky and not CMOS-compatible. To this extent, time-dependent structures are a promising alternative to realize optical isolation.

It is also possible to design optical isolators for graphene plasmonic devices

that are based on the same principle: a spatiotemporal modulation is applied to a graphene plasmonic waveguide, which induces an interband transition [32]. The modulation is implemented through graphene's field effect via a set of gating pads on the surface of the graphene waveguide. In regular plasmonic devices, modulation by a gating process is not possible because the carrier density cannot be sufficiently modulated. Instead, it is possible to achieve a time modulation using optomechanical techniques and piezoelectric materials. This can lead to frequency conversion in metallic plasmonic waveguides [33] and time modulation of plasmonic grating couplers [34].

2.3 Topological effects
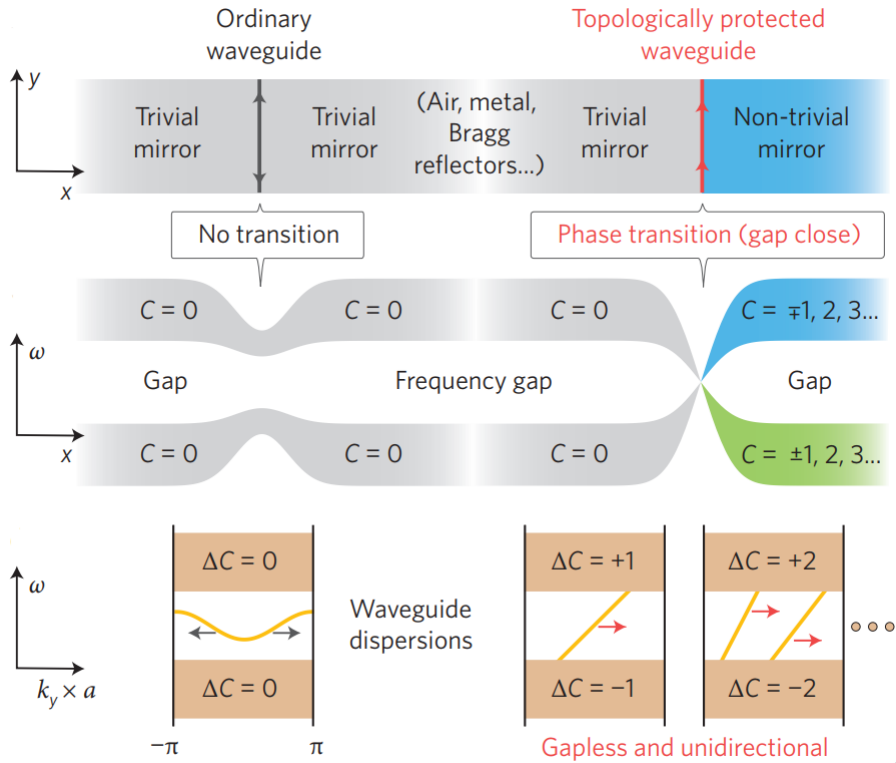
Figure 2.3: Top: A standard waveguide is formed by two topologically trivial mirrors. A topologically protected waveguide is formed at the interface of two bulk materials with different topological invariants. Center: At the interface of two materials with different topologies, a topological phase transition occurs and the gap frequency gap closes. This does not happen with materials that have the same topology. Bottom: In reciprocal space, the number of gapless edge states is equal to the change in Chern number at the interface [35].

Recently, topological photonic devices have attracted a lot of attention for their unique properties [4, 35]. Topological photonics explores the topological properties of photonic bands in materials. In particular, the edge modes in these structures are immune to backscattering caused by defects and sharp bends. Since these properties

come from the topology of the band diagram, topological edge modes are robust against defects and disorder. The immunity to backscattering makes topological devices a promising platform to achieve optical isolation.
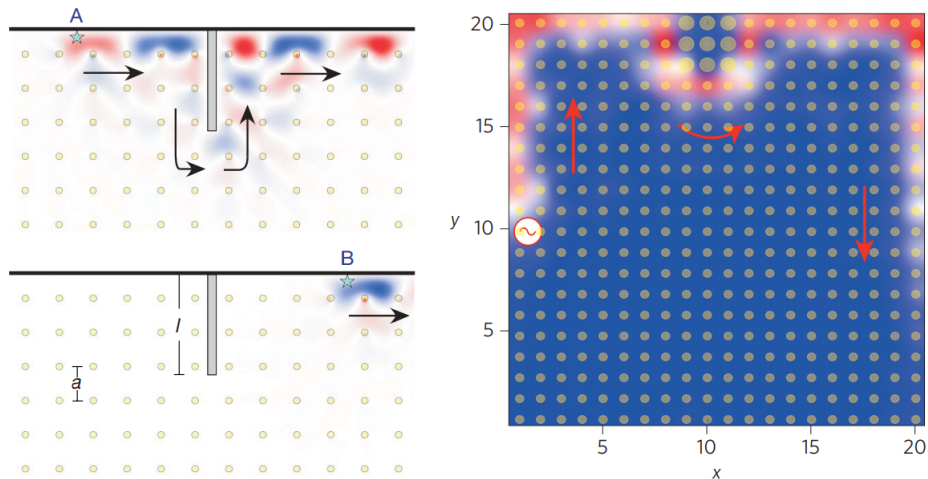
Figure 2.4: Left: Simulations of a 2D topological magneto-optic photonic crystal (operating in the microwave regime) [36]. The edge state propagates unidirectionally and is robust against metallic defects (the defects do not cause back reflection). Right: Simulations of an edge state propagating in a dynamically modulated resonator array where the coupling constants between the resonators are time-modulated [37]. The edge states are also unidirectional and immune to backscattering, even in the presence of sharp edges and defects.

The topology of a band is determined by the global behaviour of its wavefunctions and is characterized by a topological invariant called the Chern number. Since the Chern number is a topological invariant, it will not change under continuous deformations of the physical system, hence the robustness of topological states. The principle for the creation of a topologically protected state is highlighted in Figure 2.3.

Topological effects have been experimentally demonstrated. The first experiment used a 2D magneto-optical crystal in a magnetic field, fabricated in the microwave regime [36] (Figure 2.4). The edge modes propagating in that crystal were immune to backscattering, even when large metallic defects were introduced at the edges of the crystal. Topological edge states can also be realized using electromagnetic bianisotropy [38]. This constitutes a weaker form of topological protection since it does not break time-reversal symmetry. However, the modes created in these structures are also immune to backscattering and are immune to certain types of defects.

In electronic topological insulators, time symmetry is usually broken with a static magnetic field but time modulation can also be used to create topological effects, by creating a synthetic magnetic field. This was realized in a 2D array of coupled resonators, where the coupling constants are time-modulated [37]. This special form of phase control forces photons to move in circles, much like electrons in a static magnetic field. The time-symmetry breaking enables the edge states in that system to be robust against defects, and to be immune to backscattering (Figure 2.4).

3

Graphene

A few years ago graphene started to attract much attention, leading e.g. to a Nobel Prize in Physics in 2010 for K. S. Novoselov and A. K. Geim 'for groundbreaking experiments regarding the two-dimensional material graphene". Graphene is an exceptional material from many viewpoints: it is a true 2D material, which is extremely resistant and conducts heat and electricity. From an optical standpoint, it is for example remarkable that in the visible range an atomically thin layer absorbs 2.3% of the incident light [39].

Although graphene possesses a wide range of interesting features, we focus on its conductivity, as we will later use it to describe graphene plasmons. We also discuss the tunability of its properties, as this is an important building block for our later discussions. Finally, we briefly introduce graphene fabrication methods.

3.1   Graphene conductivity

Graphene is a 2D honeycomb crystal of carbon atoms. The electronic band structure of graphene is very interesting as its valence and conduction band touch at the K points of the 2D Brillouin zone. At these points the bands form Dirac cones, where the energy dispersion can be considered linear:

$$E^{\pm}(k) = \pm v_F \hbar |k| \tag{3.1}$$

where $E^{\pm}$ are the energy of the conduction (+) and valence (−) bands, k is the wavevector and v_F is the Fermi velocity ($v_F \approx 10^6$ m/s) [40, 41]. This particular band structure is the reason why graphene is often called a zero-gap semiconductor: the conduction and valence bands touch at the Dirac point where the density of states is zero.

In this section we are interested in the graphene conductivity expression as it can be used to describe graphene plasmons. From the band structure, the conductivity was derived in [40] and can be separated in two contributions. First, the conductivity term corresponding to the intra-band electron-photon scattering process (Figure 3.1, green arrow) can be expressed as (with the convention $e^{j\omega t}$):

$$\sigma_{\text{intra}}(\omega, E_F) = \frac{-2je^2 k_B T}{\pi \hbar^2 (\omega - j\tau^{-1})} \ln \left[2 \cosh \left(\frac{E_F}{2k_B T} \right) \right] \tag{3.2}$$

where T is the temperature, k_B is the Boltzmann constant, E_F is the Fermi level and τ is the electron scattering lifetime. This term actually corresponds to the Drude conductivity. Indeed, when $E_F \gg k_B T$, this conductivity takes the form:

$$\sigma_{\text{intra}}(\omega, E_F) = \frac{-je^2 E_F}{\pi \hbar^2 (\omega - j\tau^{-1})}. \tag{3.3}$$

The second contribution to the conductivity is due to interband electronic transitions (Figure 3.1, red arrow). In the case of zero temperature, this term reads:

$$\sigma_{\text{inter}}(\omega, E_F) = \frac{e^2}{4\hbar} \left[\theta(\omega - 2E_F) + \frac{j}{2\pi} \ln \frac{(\hbar\omega + 2E_F)^2}{(\hbar\omega - 2E_F)^2} \right] \tag{3.4}$$

where $\theta(\omega - 2E_F)$ is the step function. The interband terms is responsible for absorption for frequencies $\hbar\omega > 2E_F$, while the Drude contribution is responsible for graphene's metallic behaviour at lower frequencies ($\hbar\omega < E_F$).

$E_F = 1eV$
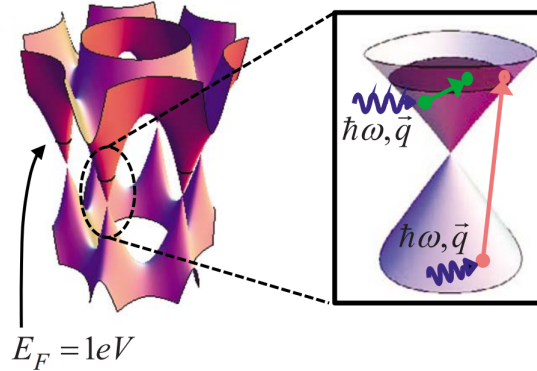
Figure 3.1: Graphene band structure and Dirac cones around the K points [9]. The electron-photon scattering process (green) and interband electronic transition (red) are depicted. Because of the particular graphene band structure and the Pauli exclusion principle, the interband transitions only occur for $\hbar\omega > 2E_F$.

For non-zero temperature, the step function must be replaced, and the interband

conductivity term now reads:

$$\sigma_{\text{inter}}(\omega, E_F) = \frac{e^2}{4\hbar} \left[\frac{1}{2} + \frac{1}{\pi} \arctan\left(\frac{\hbar\omega - 2E_F}{2k_B T} \right) + \frac{j}{2\pi} \ln \frac{(\hbar\omega + 2E_F)^2}{(\hbar\omega - 2E_F)^2 + (2k_B T)^2} \right].$$
$$(3.5)$$

The overall conductivity is then simply given by the sum of the two above contributions:

$$\sigma(\omega, E_F) = \sigma_{\text{intra}}(\omega, E_F) + \sigma_{\text{inter}}(\omega, E_F). \tag{3.6}$$

Graphene sheets can be modelled as a plane with a conductivity given by Equation 3.6. Alternatively, one can also consider graphene as a thin slab with a permittivity [5]

$$\varepsilon_r(\omega, E_F) = 1 - \frac{j\sigma(\omega, E_F)}{\varepsilon_0 \omega d} \tag{3.7}$$

where d is the effective thickness of graphene (≈ 0.5 nm). Depending on the situation we will choose different formulations in order to make simulations more efficient. For example if we want to avoid meshing problems due to the small effective thickness of graphene, we will prefer to describe graphene as a 2D conductivity plane.

3.2   Tunability

One of the many advantages of graphene (especially in the context of time modulation) is its tunability. There are three main ways to change the graphene Fermi level E_F: by chemical doping, by electrostatic gating or by optical pumping. This in turn modifies the conductivity and the optical properties of graphene.

3.2.1   Chemical doping

One can distinguish two main types of chemical doping: surface transfer doping and substitutional doping [42]. In surface transfer doping, electrons are exchanged between graphene and dopants that are adsorbed on its surface. This technique is rather general and was introduced to achieve doping at the surface of a bulk semiconductor [43]. Note that because of this mechanism, graphene is also an excellent sensor for gases and biomedical applications: molecules can adsorb on its surface and modify its conductivity [44, 45]. Because this process does not break any chemical bonds in graphene, it is reversible and adds to the tunability of graphene.

Another way to dope graphene is substitutional doping: removing carbon atoms from the honeycomb lattice and replacing them by other atoms that act as electron donors or acceptors [42]. For example, in [46] N-doped graphene was obtained by N^+ irradiation (introducing defects in the hexagonal crystal), subsequently occupied by N atoms after annealing in NH_3. This process is represented in Figure 3.2.

3.2.2   Electric field effect

A more physical way to change the electrical conductivity is to apply a gate voltage to the graphene sheet. This technique was introduced very early in the graphene
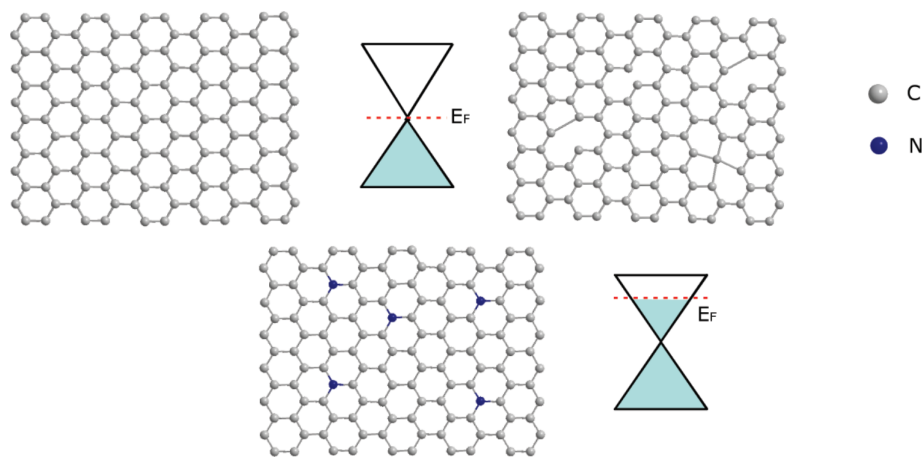
Figure 3.2: Representation of substitutional doping in graphene (from [46]). Top left:Undoped graphene is a zero gap semiconductor and its Fermi level is such that only the valence band is filled with electrons. Top right: Upon irradiation by N^+ ions, defects are created. Bottom: Then graphene is annealed in NH_3 and the vacancies are filled with N atoms, creating N-doped graphene.

reseach field by K. S. Novoselov and A. K. Geim in 2004 [47]. This effect was one of the reasons for the rapid emergence of graphene since it was envisioned that one could use this effect to create graphene based transistors. Note that it is not possible to use this effect in metals since their high bulk carrier concentration would require atomically thin layers for the electric field effect to be significant. The electric field effect allows to change not only the conductivity of graphene, but also its optical properties [48], as the optical response of graphene is governed by its conductivity. For that reason, graphene is often used for electro-optic applications and in modulators [49–51].

A common way to achieve the field effect in graphene is to use a top-gate gold contact in contact with an ion gel [52, 53]. A thin ITO layer deposited on an oxidized Si substrate is used as bottom gate. The graphene structure can then be placed in between, and its Fermi level can be controlled by the bias voltage. A schematic of this method is represented in Figure 3.3.
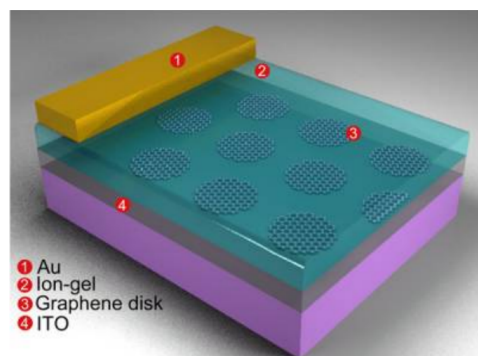
Figure 3.3: Gating of a graphene nanodisk array [53]. A graphene structure is placed in between two electrodes and surrounded by a polymer matrix (ion gel) containing mobile ions.

3.2.3   Optical pumping

A third way to tune the conductivity is to use optical pumping. An optical pump allows to change the electron and hole populations of the bands around the K point on an ultrafast timescale. Typically this is done by sending a pump pulse onto the graphene sheet, inducing intraband and interband transitions. This process was first studied through transient optical parameters (such as variations in transmission for example) of pumped graphene [54–57]. These studies were able to estimate the relaxation time of photo excited carriers (see Figure 3.4). However, this kind of optical measurements only gives indirect information about the energy and momentum of carriers.

More recently, measurements by static angle-resolved photoemission spectroscopy (ARPES) gave insight into the precise carrier dynamics taking place by monitoring the band occupation with a high temporal resolution [58–61]. Both the ARPES method and the transient optical parameter monitoring show excitation times of a few femtoseconds, while the relaxation times are of the order of a picosecond. This relaxation is due to electron-electron scattering, emission of optical phonons and coupling from electrons to accoustic phonons in the presence of defects.
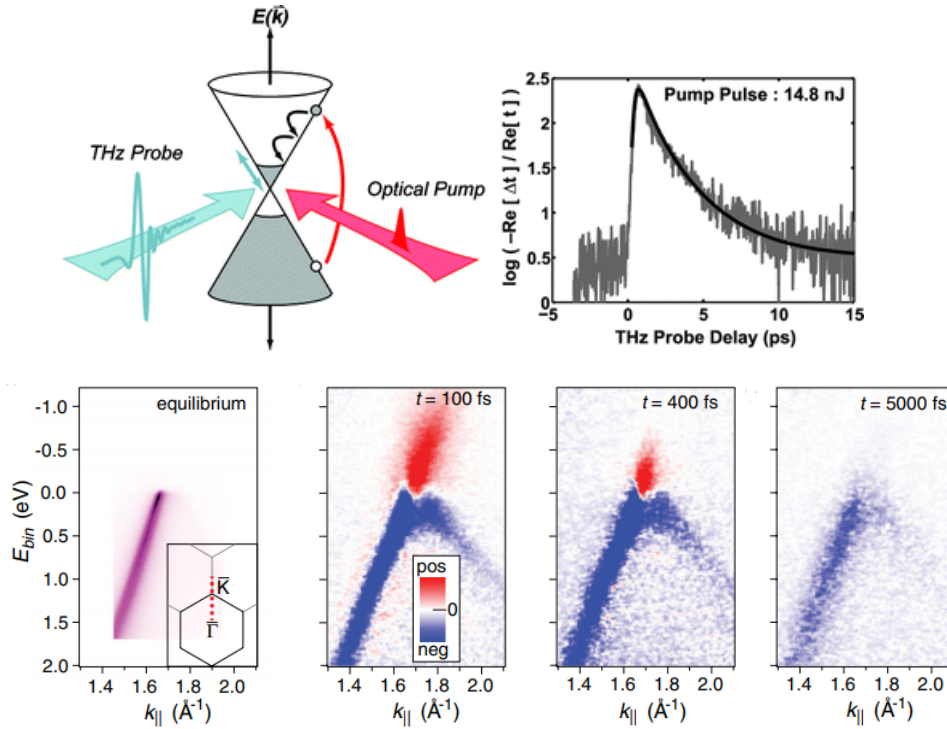
Figure 3.4: Top: Pump-probe investigation of carrier dynamics in graphene [54]. The relaxation process does not follow a simple exponential law, indicating that multiple mechanisms are responsible for carrier relaxation. Bottom: difference of ARPES measurements before and after the pump [58]. This allows to precisely measure the carrier dynamics inside the Dirac bands.

Optical pumping is particularly useful for applications that require a fast modulation of graphene conductivity. Interestingly, the limiting factor in the achievable

modulation speed is not the fast excitation of the carriers, but rather the slow relaxation times.

3.3   Fabrication

Initially, Novoselov and Geim used exfoliation to extract a graphene layer from graphite in 2004. This very simple technique allowed to produce graphene sheets, visible to the naked eye (since they absorb 2.3% of the visible light). Since then a lot of progress in the fabrication techniques has been made. In this section, we briefly introduce the most commonly used synthesis techniques, as well as patterning methods used to obtain graphene nanostructures.
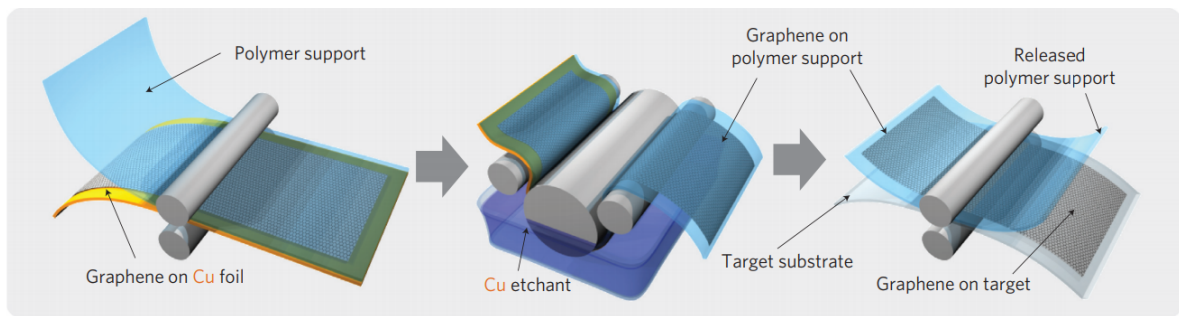
Figure 3.5: Illustration of the roll-to-roll process for transferring Cu grown graphene onto another substrate [62]. This process was used to create transparent flexible electrodes.

Chemical Vapor Deposition (CVD) is often used to fabricate graphene sheets. It can synthesize macroscopic graphene areas, typically to produce flexible and transparent electrodes for larger surfaces. For these reasons, graphene is a strong candidate to replace ITO films as a transparent electrode. CVD growth of graphene is usually performed on a metallic substrate (usually Ni and Cu). Although Ni is a good candidate for CVD graphene synthesis, the grain size of polycrystalline Ni is a limiting factor, leading to a lower graphene film quality. To improve uniformity, monocrystalline Ni(1,1,1) substrates have been used, taking the graphene monolayer percentage from 72.8% in the polycrystalline case to 91.4% [63]. Many other substrates have been explored, but the best substrates are arguably copper substrates [64]. With a copper substrate, this method allows to produce graphene areas with a >95% percentage of monolayer graphene. The reason why copper is such a good substrate for graphene growth is that carbon has a low solubility in copper. Whereas graphene formation on a Ni surface ressembles a segregation process (making the prevention of multilayer formation difficult), the growth on Cu is due to the catalytic decomposition of hydrocarbons. Because of this, the growth on Cu is a self limiting process: when the surface is covered by carbon atoms, there is no more hydrocarbon decomposition and graphene growth stops, making this process more effective at creating monolayer graphene.

Once synthesized, graphene can then be used on another substrate. Three steps are usually necessary: first a polymer is placed on top of graphene and adheres to it. Then the metallic film is etched and then the graphene layer is transferred
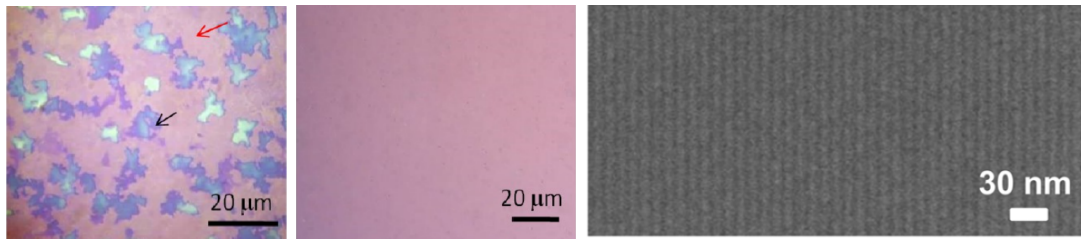
Figure 3.6: Left: Optical images of graphene transferred on a SiO$_2$/Si substrate (left: Ni, middle: Cu [63]). Right: 5 nm nanoribbons produced by HIBL from Cu grown graphene [65].

onto another substrate. In the case of graphene grown on copper foil (which are both flexible materials), this allows for large scale roll-to-roll production [62] (see Figure 3.5).

Once a graphene film has been placed on the desired substrate, it is also possible to pattern it. Electron beam lithography in pair with O$_2$ plasma etching can be used to produce high quality graphene ribbons, with widths ranging from 15 to 100 nm [66]. However, breaking the sub-10 nm resolution has been a great challenge for electron beam lithography. Another technique has since been used with great results: Helium Ion Beam Lithography (HIBL) [67]. Note that however this technique might contaminate the semiconductor substrates [68, 69]. With this method, patterning of graphene nanoribbons down to a 5 nm width has been achieved [65].

All these methods and results show that we have come a long way from the first exfoliation of graphene and that techniques to produce nanometer scale graphene structures are well-established.

4

Plasmonics

Plasmons (or plasmon-polaritons) are quasi-particles that arise from the interaction of metals with light. More specifically, in metals, electrons can sustain volume and surface oscillations at optical frequencies. This coupling of light with oscillating electrons at the surface of a metal is called a surface plasmon polariton. In this chapter we introduce plasmonics, as we will rely on these concepts for further developments. First we will discuss metal plasmons to describe the basic properties, before describing graphene plasmons in planar sheets, as well as in nanoribbons.

4.1 Drude model

To describe metal plasmons, we need a way to describe the response of a metal to an oscillating field. Maxwell's equations describe how charges and currents create electromagnetic fields, but to describe the interaction of these fields with materials, constitutive relations are needed. In a non-dispersive linear and isotropic medium, they are written as

$$\mathbf{D} = \varepsilon_0 \mathbf{E} + \mathbf{P} = \varepsilon_0 \varepsilon_r \mathbf{E} \tag{4.1}$$

$$\mathbf{B} = \mu_0(\mathbf{H} + \mathbf{M}) = \mu_0 \mu_r \mathbf{H} \tag{4.2}$$

where $\mathbf{D}$ is the electric displacement, $\mathbf{B}$ the magnetic induction, $\mathbf{P}$ the polarization, $\mathbf{M}$ the magnetization, ε_0 the vacuum permittivity, and μ_0 the vacuum permeability. The information about the materials' electromagnetic properties is contained in the parameters ε_r (the relative permittivity) and μ_r (the relative permeability). These two parameters can be frequency dependent in the case of dispersive media, wavevector dependent if they exhibit a non-local response, or non-linear if they depend on the field intensity. Typically, non-local effects are important for metallic objects with a dimension of the order of the electron mean free path. In this thesis, we will not consider non-local materials or non-linear materials. Moreover, we will not deal with magnetic materials (which is rare at optical frequencies) so we can set μ_r to 1.

The permittivity of a metal is often described by Drude's model [5]. In this model, the metal is a free electron gas and the equation of motion for an individual electron in a time harmonic field is:

$$m\frac{d^2\mathbf{r}(t)}{dt^2} + m\gamma_e\frac{d\mathbf{r}(t)}{dt} = -e\mathbf{E}(t) \tag{4.3}$$

where m is the (effective) electron mass, γ_e is the electron damping rate (due to electron-electron collisions e.g.) and $\mathbf{r}$ is the electron position. $\mathbf{E}(t) = \mathbf{E}_0 e^{j\omega t}$ is the amplitude of the driving electric field at frequency ω. By considering a solution of the form $\mathbf{r}(t) = \mathbf{r}_0 e^{j\omega t}$, one gets the electron response:

$$\mathbf{r}(t) = \frac{e}{m(\omega^2 - j\gamma_e\omega)}\mathbf{E}(t). \tag{4.4}$$

These electrons displaced by the driving field contribute to the *macroscopic* polarisation

$$\mathbf{P} = -ne\mathbf{r} = -\frac{ne^2}{m(\omega^2 - j\gamma_e\omega)}\mathbf{E}. \tag{4.5}$$

Using the constitutive relation $\mathbf{D} = \varepsilon_0\mathbf{E} + \mathbf{P}$,

$$\mathbf{D} = \varepsilon_0\left(1 - \frac{\omega_p^2}{\omega^2 - j\gamma_e\omega}\right)\mathbf{E} \tag{4.6}$$

where $\omega_p^2 = \dfrac{ne^2}{\epsilon_0 m}$ is the plasma frequency. By comparing this relation to Equation 4.1, one finds the relative permittivity of metals:

$$\varepsilon_r(\omega) = 1 - \frac{\omega_p^2}{\omega^2 - j\gamma_e\omega}. \tag{4.7}$$

This relation derived using the microscopic response of electrons can now be used in the macroscopic Maxwell's equations to describe the response of metals to a harmonic electric field.

In metals, bulk plasmons are a collective oscillation of the electron density at the plasma frequency ω_p, while the movement of positive ions in the metallic lattice is negligible [70]. These collective oscillations play an important role in the optical properties of metals. For frequencies below ω_p, the real part of the permittivity is negative and no propagative modes exist inside the metal. For frequencies higher than ω_p however, the metal behaves as a dielectric and propagative modes do exist.

4.2   Plasmons in standard metals

In this section, we will describe metal plasmons with the Drude permittivity for metals of Equation 4.7. We consider standard 3D metals first, as we will consider graphene (a 2D metal) in the next section. Here we suppose that materials are isotropic and non-magnetic. We also assume that the fields have an harmonic time dependence with the convention $e^{j\omega t}$. With these assumptions, Maxwell's equations read

$$\nabla \cdot \mathbf{D} = \rho \tag{4.8}$$

$$\nabla \cdot \mathbf{B} = 0 \tag{4.9}$$

$$\nabla \times \mathbf{E} = -j\omega \mathbf{B} \tag{4.10}$$

$$\nabla \times \mathbf{H} = \mathbf{J} + j\omega \mathbf{D}. \tag{4.11}$$

We now suppose that $\mathbf{J} = \sigma \mathbf{E} = 0$, meaning that all the response of metals is contained in the metal electric permittivity (Equation 4.7) and not in the metal conductivity. Equations 4.10 and 4.11 now take the form:

$$\nabla \times \mathbf{E} = -j\mu_0 \omega \mathbf{H} \tag{4.12}$$

$$\nabla \times \mathbf{H} = j\varepsilon_0 \varepsilon_r \omega \mathbf{E}. \tag{4.13}$$

We will investigate these equations in the context of propagative modes in structures that are invariant in the propagation direction and invariant in the transverse direction. These structures are described by their relative permittivity $\varepsilon_r(x)$, which only depends on x in this case. Equations 4.12 and 4.13 are rather general and can be used to describe stacks of dielectric and metallic layers (see Figure 4.1).
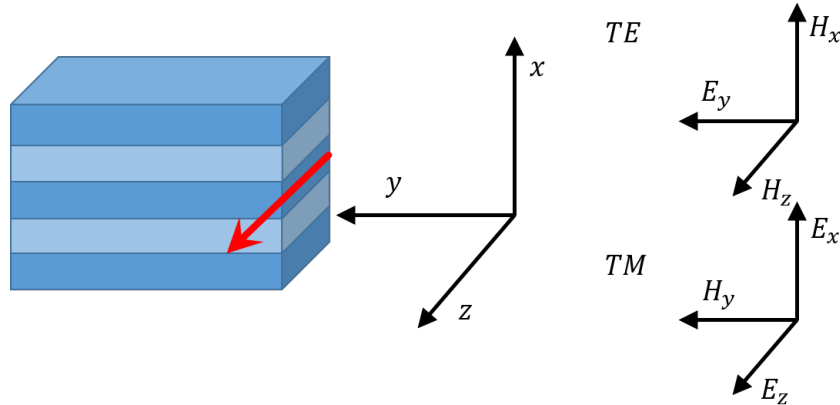
Figure 4.1: Left: Structure used to describe propagative modes. Invariant in the propagation direction (along z) and in the transverse direction (along y). The red arrow highlights the propagation direction. Right: TE (top) and TM (bottom) polarizations. The arrows represent non-zero field components in each case.

With the coordinate choice represented in Figure 4.1, the electric and magnetic fields can be expressed as:

$$\mathbf{E}(x, z) = \mathbf{e}(x)e^{-j\beta z} \tag{4.14}$$

$$\mathbf{H}(x, z) = \mathbf{h}(x)e^{-j\beta z}. \tag{4.15}$$

By injecting Equations 4.14 and 4.15 into Equations 4.12 and 4.13 and examining each individual component of the fields, one obtains two decoupled sets of three equations. These decoupled systems of equations describe the Transverse Electric (TE) and Transverse Magnetic (TM) polarizations (see Figure 4.1). For the TE polarization:

$$\beta e_y(x) = -\omega\mu_0 h_x(x) \tag{4.16}$$

$$\frac{de_y(x)}{dx} = -j\omega\mu_0 h_z(x) \tag{4.17}$$

$$\omega\varepsilon_0\varepsilon_r(x)e_y(x) = -\beta h_x(x) + j\frac{h_z(x)}{dx} \tag{4.18}$$

And for the TM polarization:

$$\beta h_y(x) = \omega\varepsilon_0\varepsilon_r(x)e_x(x) \tag{4.19}$$

$$\frac{dh_y(x)}{dx} = j\omega\varepsilon_0\varepsilon_r(x)e_z(x) \tag{4.20}$$

$$\omega\mu_0 h_y(x) = \beta e_x(x) - j\frac{e_z(x)}{dx}. \tag{4.21}$$

By eliminating the x and z components in the TE and TM equation systems, one obtains the following Helmholtz equations in each individual layer (by definition, the permittivity is constant within the layers):

$$\frac{d^2 e_y(x)}{dx^2} + k_0^2\varepsilon_r e_y(x) = \beta^2 e_y(x) \tag{4.22}$$

$$\frac{d^2 h_y(x)}{dx^2} + k_0^2\varepsilon_r h_y(x) = \beta^2 h_y(x) \tag{4.23}$$

for TE and TM polarizations, respectively. Even if the two equations 4.22 and 4.23 have an identical structure, their solutions are different because the boundary conditions are different for E and H fields. From Maxwell's equations, the boundary conditions are:

$$\mathbf{n} \times (\mathbf{E}_1 - \mathbf{E}_2) = 0 \tag{4.24}$$

$$\mathbf{n} \times (\mathbf{H}_1 - \mathbf{H}_2) = 0 \tag{4.25}$$

$$\mathbf{n} \cdot (\mathbf{D}_1 - \mathbf{D}_2) = 0 \tag{4.26}$$

$$\mathbf{n} \cdot (\mathbf{B}_1 - \mathbf{B}_2) = 0 \tag{4.27}$$

where $\mathbf{n}$ is a normal vector to the interface between two layers. These conditions impose that the $\mathbf{E}$ and $\mathbf{H}$ components tangent to the interface are continuous, while the $\mathbf{D}$ and $\mathbf{B}$ components normal to the interface are continuous.

We can use Equation 4.23 along with the boundary conditions to get the generic solution for modes in the TM polarization. The transverse profile is of the form

$$h_y(x) = Ae^{jk_x x} + Be^{-jk_x x} \tag{4.28}$$

inside a layer, where A and B are constants and $k_x = \sqrt{\varepsilon_r k_0^2 - \beta^2}$. Note that we are only interested in the TM polarization here because plasmonic modes only exist in that polarization.

We now discuss the case of a single interface between a dielectric with permittivity $\varepsilon_d > 0$ and a metal with permittivity $\varepsilon_m < 0$. This structure is represented in Figure 4.2. If we only consider solutions confined to the interface and evanescent in the x direction, we find by using Equation 4.28, along with the continuity of H_y (the y component of $\mathbf{H}$) and the definition of the total $\mathbf{H}$ field (Equation 4.15):

$$H_y(x, z) = A e^{-j\beta z} e^{-\delta x} \quad \text{for } x > 0 \tag{4.29}$$

$$H_y(x, z) = A e^{-j\beta z} e^{\gamma x} \quad \text{for } x < 0 \tag{4.30}$$

where $\delta = \sqrt{\beta^2 - \varepsilon_d k_0^2}$ and $\gamma = \sqrt{\beta^2 - \varepsilon_m k_0^2}$.
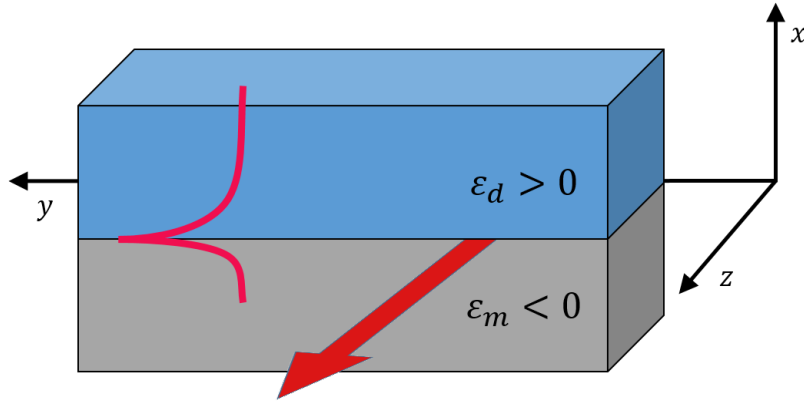
Figure 4.2: Interface between a dielectric and a metal and sketch of the plasmonic mode supported.

Using the TM equations and the continuity conditions, one can show that

$$\frac{\delta}{\gamma} = -\frac{\varepsilon_d}{\varepsilon_m}. \tag{4.31}$$

This means that since we require evanescent fields (δ and γ are real and positive), ε_d and ε_m must have opposite signs, meaning that this type of mode (confined to the interface) only exists between a dielectric and a metal. Equation 4.31 is actually the dispersion relation for surface plasmons at a dielectric metal interface. It can be rewritten as:

$$\beta = k_0 \sqrt{\frac{\varepsilon_d \varepsilon_m}{\varepsilon_d + \varepsilon_m}}. \tag{4.32}$$

This dispersion relation is plotted in Figure 4.3 for an arbitrary Drude metal. These plasmonic modes are confined and non-radiative modes: they are below the light line and thus cannot couple to radiation. For large wavevectors, the frequency of Surface Plasmon Polaritons (SPPs) approaches the surface plasmon frequency ω_{sp}:

$$\omega_{sp} = \frac{\omega_p}{1 + \sqrt{\varepsilon_d}}. \tag{4.33}$$

At this frequency, the propagation constant goes to infinity and the group velocity vanishes. This means that the plasmonic mode becomes extremely confined around the interface and that it becomes a static mode. For lower propagation constants, β approaches the light line and the plasmonic mode resembles a grazing-incidence plane wave, since it extends into the dielectric for many wavelengths. For frequencies higher than the plasmon frequency ω_p, the metal becomes transparent and the mode becomes radiative as it lies above the light line. Since we defined plasmonic modes as modes confined around the interface, this mode is no longer a SPP mode.
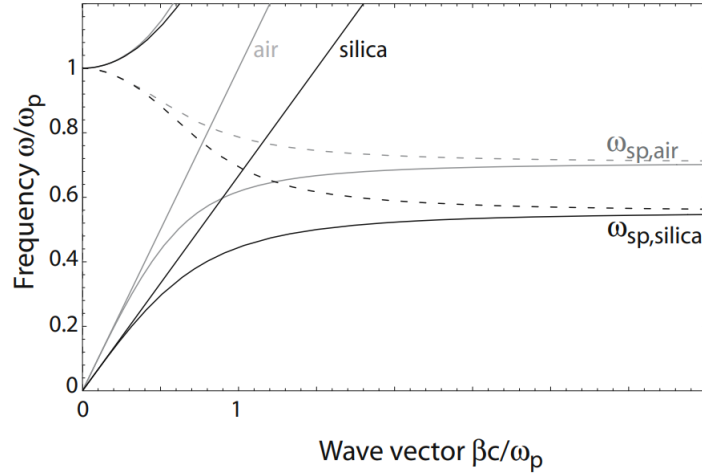
Figure 4.3: Dispersion plot for SPP at a single interface for two different dielectrics [5]. Here only lossless metals were considered so the damping rate $\gamma_e = 0$ in Equation 4.7. The dashed lines represent the imaginary part of the propagation constant, where plasmonic modes do not exist. In real metals, the non-zero damping rate prevents β from reaching infinite values.

4.3   Graphene plasmons

As discussed in Section 3.1, graphene behaves as a metal in the far- to near-infrared. Even though it is extremely thin, it can also support TM plasmonic modes in this range. Graphene can either be modelled as a plane with a surface conductivity, or as a (thin) slab with a Drude permittivity. In this section, we introduce graphene's plasmonic modes by considering the conductivity. The used geometry is represented in Figure 4.4: a graphene sheet between two semi-infinite dielectric layers. This structure is also invariant in the propagation direction and in the transverse direction, as in the previous Section 4.2.

Graphene plasmons are also TM modes and obey the Helmholtz Equation 4.23. Once again, we are interested in solutions of the form 4.28 confined at the graphene sheet. With this assumption for the field profile, the plasmonic mode can be written as [71]:

$$\mathbf{E}_i = (E_{i,x}, 0, E_{i,z})e^{-j\beta z}e^{-\delta_i|x|} \tag{4.34}$$

$$\mathbf{H}_i = (0, H_{i,x}, 0)e^{-j\beta z}e^{-\delta_i|x|} \tag{4.35}$$
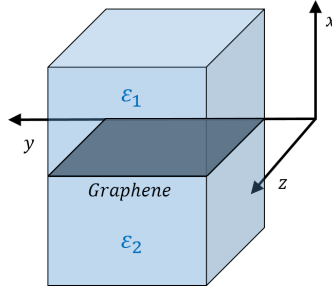
Figure 4.4: Graphene sheet surrounded by two semi-infinite dielectric layers. Graphene is modelled as a conducting plane.

where $i = 1, 2$ is the medium index (see Figure 4.4), β is the plasmon propagation constant and $\delta_i = \sqrt{\beta^2 - \varepsilon_i k_0^2}$. Unlike in Section 4.2, we need to use different boundary conditions. This is because graphene is described by its conductivity, while we described metals with their permittivity. The boundary conditions in this case read:

$$\mathbf{n} \times (\mathbf{E}_1 - \mathbf{E}_2) = 0 \tag{4.36}$$

$$\mathbf{n} \times (\mathbf{H}_1 - \mathbf{H}_2) = \mathbf{n} \times \mathbf{J} \tag{4.37}$$

$$\mathbf{n} \cdot (\mathbf{D}_1 - \mathbf{D}_2) = \rho \tag{4.38}$$

$$\mathbf{n} \cdot (\mathbf{B}_1 - \mathbf{B}_2) = 0 \tag{4.39}$$

where ρ is the charge density and $\mathbf{J} = \sigma(\omega, E_F)\mathbf{E}_t$ is the surface current. Note that $\mathbf{E}_t$ is the electric field projected on the graphene plane, as electrons are confined to this surface. Since we consider a TM polarized mode (so only E_z lies in the graphene plane), Equation 4.37 reduces to $H_{1,y} - H_{2,y} = \sigma E_z = J_z$. Using these new boundary conditions, the graphene plasmon relation is derived [9]:

$$
\begin{aligned}
\frac{j\sigma(\omega, E_F)}{\omega \varepsilon_0} &= \frac{\varepsilon_1}{\delta_1} + \frac{\varepsilon_2}{\delta_2} \\
&= \frac{\varepsilon_1}{\sqrt{\beta^2 - \varepsilon_1 k_0^2}} + \frac{\varepsilon_2}{\sqrt{\beta^2 - \varepsilon_2 k_0^2}}.
\end{aligned}
\tag{4.40}
$$

In this thesis, we work in the frequency range from mid- to far-infrared. At these frequencies, graphene plasmons are extremely confined and lie far below the light line. This corresponds to the non-retarded regime ($\beta \gg k_0$). In this regime, we can safely make the approximation that $\delta_i = \sqrt{\beta^2 - \varepsilon_i k_0^2} \approx \beta$. The dispersion relation of Equation 4.40 reduces to

$$\beta = -\frac{\varepsilon_1 + \varepsilon_2}{2} \frac{2j\omega \varepsilon_0}{\sigma(\omega, E_F)}. \tag{4.41}$$

We can further simplify Equation 4.41 by dropping the interband term in the graphene conductivity. In Section 3.1 we showed that $\sigma(\omega, E_F) = \sigma_{\text{intra}}(\omega, E_F) + \sigma_{\text{inter}}(\omega, E_F)$ and that the interband terms becomes significant for frequencies such that $\hbar\omega > E_F$. Since we work in the non-retarded regime, this condition will always be satisfied and we can neglect the interband term and only use the Drude

conductivity of Equation 3.3. The dispersion relation of Equation 4.41 then reads

$$\beta = \frac{\varepsilon_1 + \varepsilon_2}{2} \frac{2\pi\hbar^2\varepsilon_0}{e^2 E_F} \omega \left(\omega - j\tau^{-1}\right). \tag{4.42}$$

The graphene plasmon dispersion is represented in Figure 4.5 for both the exact form (Equation 4.40) and the Drude approximation (Equation 4.42), for several values of the Fermi level E_F. All the dispersions lie far below the light line, meaning that the modes are extremely confined, even compared to metal plasmons. Note the small difference between the exact form and the Drude approximation for large frequencies ω and small Fermi level E_F. This is because interband transitions (that are not accounted for in the Drude conductivity) start to take place. At larger frequencies (and smaller Fermi levels), the assumption $\hbar\omega < E_F$ is no longer satisfied and the Drude conductivity no longer correctly describes the graphene conductivity.
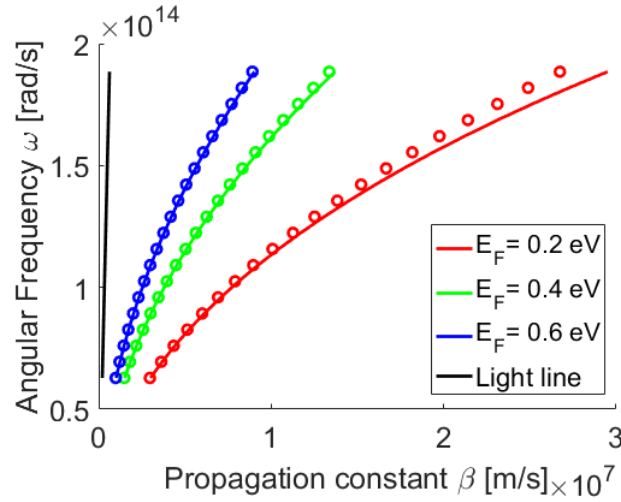
Figure 4.5: Free-standing graphene plasmon dispersion for several Fermi levels E_F (with $\varepsilon_{1,2} = 1$). Solid lines are the exact form of Equation 4.40, while circles represent Equation 4.42. The whole dispersion curve lies below the light line, indicating that graphene plasmons are extremely confined and do not couple with plane waves.

4.4   Graphene ribbon arrays

Graphene plasmons in a 2D sheet cannot be directly excited by an incident plane wave, as they are far from the light cone. However, graphene nanostructures support plasmonic modes that can couple to radiation, either in single elements or in arrays. Since the plasmon wavelength λ_p is much smaller than the free-space wavelength, resonance effects can occur at sub-wavelength scale. Moreover, because of the extreme confinement of the fields around graphene, plasmonic resonances can be used, amongst others, for SERS applications [72, 73], allowing to investigate the infrared signature of biomolecules. Plasmonic resonances can also be exploited to enhance the interaction of light with graphene. A planar graphene sheet 'only' absorbs 2.3 % of visible light, but plasmonic resonances allow to increase this absorption. Resonant enhancement of absorption has been proposed and demonstrated in [74–76].

In future chapters, we will also use graphene plasmonic resonances to improve the interaction of light with a time modulation. In the remainder of this section, we will focus on one type of resonant structure: graphene nanoribbons.
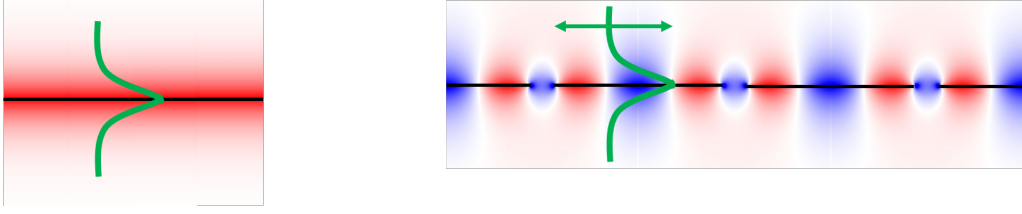
Figure 4.6: Left: Sketch of a propagative plasmonic mode in a graphene sheet. Right: Fabry-Pérot resonance created by a plasmon reflecting at the edges of a graphene ribbon in a graphene ribbon array.

In optics, a Fabry-Pérot (FP) cavity typically consists of two parallel highly-reflecting mirrors. Its transmission spectrum consists of peaks with high transmission, corresponding to resonances in the cavity. These resonances occur when constructive interferences are created between the light beams inside the cavity. Plasmonic resonances in graphene nanoribbons can be seen as FP cavities (see Figure 4.6). When a graphene plasmon is incident on the nanorribon edge, it is reflected with almost 100% amplitude [77, 78] and nearly no light is radiated. However, the reflection phase is non-trivial [79] and thus, the conditions for a resonant cavity mode read:
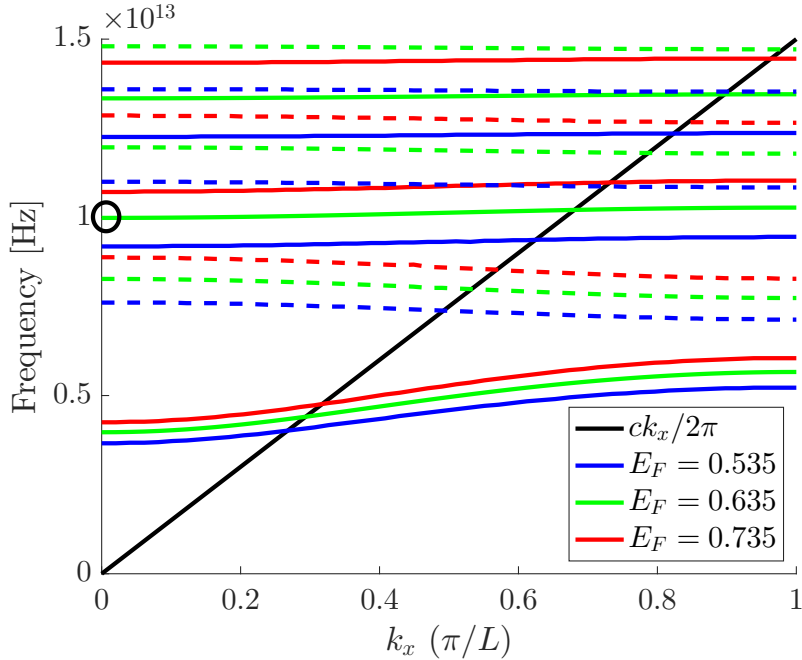
Figure 4.7: Dispersion of the lattice modes ($L = 10\,\mu m$ and $D = 8.75\,\mu m$) for several E_F values. Even modes that couple with incident light are shown with solid lines while odd modes are only shown with dashed lines. The mode of interest in this thesis is the third mode at normal incidence indicated by a black circle.
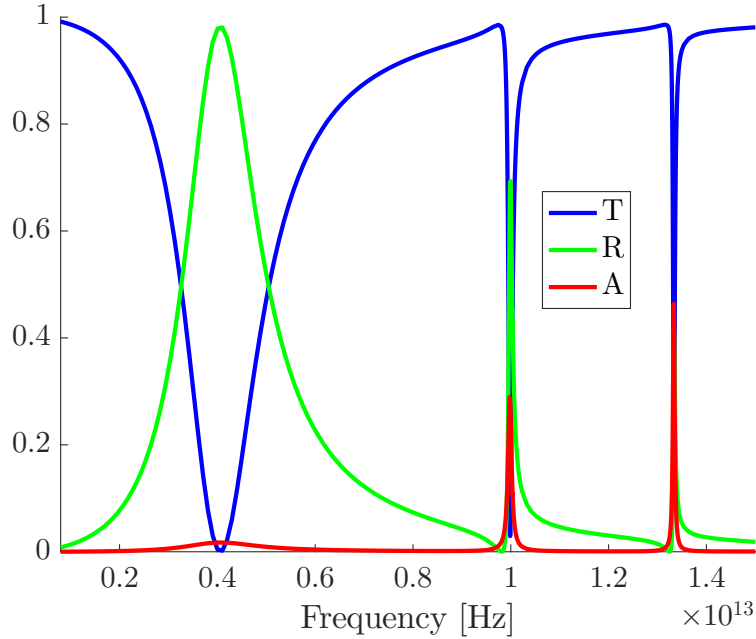
Figure 4.8: Transmission T, reflection R and absorption A spectra of a graphene nanoribbon array under normal incidence. The Fermi level is $E_F = 0.635$ eV, the ribbon width is $D = 8.75$ μm and the period is $L = 10$ μm. Each dip in transmission corresponds to a plasmonic resonance in the graphene nanoribbon array. Only even modes are excited by incident light at normal incidence because of the mode parity.

$$2\beta D + 2\Phi_R = 2\pi n \tag{4.43}$$

where D is the ribbon width, β is the plasmon propagation constant (in a lossless graphene sheet), Φ_R is the non-trivial reflection phase and n is an integer representing the mode order. The phase Φ_R can be approximated to $-3\pi/4$ rad and does not depend on the dielectric environment, doping level or plasmon frequency. By injecting Equation 4.41 into Equation 4.43, one can find the frequencies corresponding to each FP mode by solving

$$\omega = \frac{(n + 3/4)\pi \Im\left[\sigma\left(\omega, E_F\right)\right]}{2\varepsilon_0 \varepsilon_r D} \tag{4.44}$$

where ε_r is the surrounding medium relative permittivity. This method is an effective way to estimate the resonance frequency of graphene ribbons. This resonance frequency is a function of the surrounding medium permittivity, nanoribbon length and Fermi level. These parameters can be chosen by design and will determine the optical properties of a graphene nanoribbon. In graphene nanoribbon arrays, each separate ribbon has localized Fabry-Pérot type modes (three are visible in the range of Figure 4.8), which originate from the graphene plasmon propagating back and forth. The vertically incident light (at $k_x = 0$) can excite these array modes: they are above the lightline, they are compatible with the incident polarization, and the underlying Fabry-Pérot modes are 'leaky' or radiative.

In Figure 4.7 we plot the simulated dispersion of the Bloch modes in the lattice. Even if plasmonic modes exist for all k_x, they can only be excited if they lie above the light line (black line in Figure 4.7). Moreover, at normal incidence ($k_x = 0$) only the even modes are excited because of the parity of the incident light. Therefore, half of the modes from the dispersion are not present in the spectra of Figure 4.8.

There is also the typical tight-binding lattice effect: the localized modes can couple with each other because the ribbon interspacing is relatively small ($D/L = 0.875$ where D is the ribbon length and L is the lattice period). This causes the sine-like shape of the dispersion curves around the resonance frequency of a single ribbon mode. Note that the curvature is stronger for lower order modes, because the overlap of adjacent ribbon modes is larger in that case.

Unlike plasmons supported by a graphene sheet, the plasmonic resonances in graphene nanoribbons are leaky modes. This means that they can couple to radiation, provided that the plasmonic mode has a matching parity (only even modes can couple to radiation at normal incidence). The coupling of light with a plasmonic resonance is important in the context of this thesis: light couples to a plasmonic mode, which in turn interacts with a time modulation and then couples to radiation, at a different frequency for example. Since graphene plasmonic modes strongly depend on system parameters, graphene nanoribbons are an ideal platform for tunable plasmonic responses, especially for dynamic modulation via the Fermi level. We will exploit this property in Chapter 6 to dynamically modulate the resonance frequency of a ribbon array.

5

Optical concepts

5.1 Coupled Mode Theory

In this section we briefly introduce Coupled Mode Theory (CMT) as it will be applied in many different cases throughout this thesis. This theory is particularly useful to describe physical systems involving a resonant mode that is coupled to input and output ports [80]. We will use this framework in the context of plasmonics and photonics, but its range of application is much larger (acoustics, phononics, etc.).

5.1.1 Single mode resonator

In the following, we describe the formalism used to model a single mode optical resonator coupled to m ports. The dynamic equation for the mode amplitude a is given by [81, 82]:

$$\frac{da(t)}{dt} = \left(j\omega_{\mathrm{res}} - \frac{1}{\tau}\right) a(t) + (\langle\kappa|^*) |s_+(t)\rangle \tag{5.1}$$

$$|s_-(t)\rangle = C |s_+(t)\rangle + a(t) |d\rangle \tag{5.2}$$

where ω_{res} is the cavity mode resonance frequency and τ is the total cavity decay rate. The input and output ports are represented by the components of $|s_+\rangle$ and $|s_-\rangle$, respectively:

$$|s_+\rangle = \begin{pmatrix} s_{1+} \\ s_{2+} \\ \vdots \\ s_{m+} \end{pmatrix}, \ |s_-\rangle = \begin{pmatrix} s_{1-} \\ s_{2-} \\ \vdots \\ s_{m-} \end{pmatrix}, \tag{5.3}$$

The coupling between the cavity mode a and the input ports is the vector $\langle\kappa|^*$ containing the coupling constants κ_i for each input port, with i ranging from 1 to m. The cavity mode is also coupled to the output ports by the coupling constants d_i inside $|d\rangle$. In addition to these two coupling mechanisms, the model also includes a direct pathway between input and output ports via the scattering matrix C. The compact Dirac notation allows to simultaneously describe all the couplings in the system. Explicitly the coupling matrices are given by

$$\langle\kappa|^* = \begin{pmatrix} \kappa_1 \\ \kappa_2 \\ \vdots \\ \kappa_m \end{pmatrix}, \ |d\rangle = \begin{pmatrix} d_1 \\ d_2 \\ \vdots \\ d_m \end{pmatrix}. \tag{5.4}$$

This single mode system is represented in Figure 5.1. Since C accounts for a direct pathway between the ports, the matrix needs to be unitary (to ensure energy conservation) and symmetric (to respect time reversal symmetry). The cavity mode amplitude a is normalized so that $|a|^2$ is equal to the energy inside the cavity. The validity of coupled mode theory is limited to the case were the width of the resonance is far smaller than the resonance frequency [81], which will be the case each time we use this model.
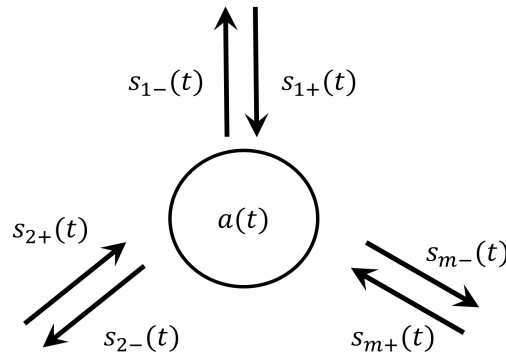
Figure 5.1: Single mode resonator with mode amplitude $a(t)$ coupled to input and output ports $s_{i\pm}(t)$.

The coefficients $|\kappa\rangle$, $|d\rangle$, $|\tau\rangle$ and C are not independent, but they follow a set of rules set by conservation of energy and time reversal symmetry constraints. Moreover one can also use the geometric symmetries of the system and for example impose that the resonant mode decays symmetrically or anti-symmetrically into specific ports.

For an incident excitation $|s_-\rangle$ at frequency ω, the output $|s_-\rangle$ can be expressed as

$$|s_-\rangle = \left[C + \frac{|d\rangle \langle \kappa|^*}{j(\omega - \omega_{\text{res}}) + 1/\tau} \right] |s_+\rangle \equiv S |s_+\rangle \tag{5.5}$$

where S is defined as the scattering matrix that links input and output ports. Because of time reversal symmetry, S has to be symmetric. This constraint imposes that

$$\langle d|\kappa \rangle^* = \langle \kappa|d \rangle^* . \tag{5.6}$$

The resonant mode amplitude in that case is given by

$$a = \frac{(\langle \kappa|^*) |s_+\rangle}{j(\omega - \omega_{\text{res}}) + 1/\tau}. \tag{5.7}$$

When considering a resonator that is not coupled to any input excitation, but that has a non-zero mode amplitude at $t = 0$, energy conservation requires that all the energy will leak out into the output ports. When considering the variation of energy in the resonator and imposing that all this energy leaks through the ports ($\langle s_-|s_-\rangle$ is the total power leaking from the resonator), one finds

$$\frac{d|a|^2}{dt} = -\frac{2}{\tau} |a|^2 = - \langle s_-|s_- \rangle . \tag{5.8}$$

When considering Equation 5.2 in the case where no excitation is present, one finds

$$\langle s_-|s_- \rangle = |a|^2 \langle d|d \rangle , \tag{5.9}$$

which along with Equation 5.8 imposes that

$$\langle d|d \rangle = 2/\tau. \tag{5.10}$$

We now consider the time-reversed case of Equation 5.8. Now the resonator is excited through $|s_-\rangle^*$ by an exponentially growing incident wave at frequency $\omega = \omega_0 - j(1/\tau)$. The time-reversed solution to this system must be the time-reversed version of Equation 5.7 with $\omega = \omega_0 - j(1/\tau)$:

$$a^* = \frac{(\langle \kappa|s_-\rangle)^*}{2/\tau} = \frac{(\langle \kappa|d\rangle \, a)^*}{2/\tau} \tag{5.11}$$

where we used Equation 5.2 with no excitation. This imposes that

$$\langle \kappa|d \rangle = 2/\tau = \langle \kappa|d \rangle^* . \tag{5.12}$$

This along with Equation 5.6 and 5.10 leads to

$$|\kappa\rangle = |d\rangle . \tag{5.13}$$

The exponentially growing excitation $|s_-\rangle^*$ in the time-reversed case must also satisfy the constraint that no outgoing wave leaks through $|s_+\rangle$. To insure this, we must have in the time-reversed Equation 5.2

$$0 = C |s_-\rangle^* + a^* |d\rangle = a^* C |d\rangle^* + a^* |d\rangle , \tag{5.14}$$

leading to one last constraint:

$$C \left| d \right\rangle^* = - \left| d \right\rangle . \tag{5.15}$$

These considerations show that the coupling coefficients are connected to the direct scattering process because of energy conservation and time reversal symmetry. When designing a CMT model, one needs to account for all these constraints.

Until now we did not consider losses. In Equation 5.8, the resonator only loses its energy through the ports and there are no absorptive losses inside the cavity. To account for losses, a new term must be added to Equation 5.1:

$$\frac{da(t)}{dt} = \left(j\omega_{\text{res}} - \frac{1}{\tau} - \frac{1}{\tau_0} \right) a(t) + \left(\left\langle \kappa \right|^* \right) \left| s_+(t) \right\rangle \tag{5.16}$$

where τ_0 is the cavity lifetime if the resonant mode does not couple to ports [81]. This $1/\tau_0$ term is not constrained by energy conservation, and is independent from the coupling coefficients and from the direct scattering process. A common practice is to find a set of CMT parameters consistent with time reversal and energy conservation and to add losses to that model [83].

5.1.2   Multimode resonator

In Section 5.1.1, we showed how to describe a single mode resonator coupled to multiple ports with a CMT model. In this section, we will extend this case to multimode resonators, again coupled to multiple ports, following [84]. We now consider a cavity supporting n modes. In this case, the mode amplitude is now a vector $\boldsymbol{a}(t)$ (with n rows) and the resonance frequency ω_0 of the single mode case becomes a $n \times n$ matrix Ω with the respective frequencies as the diagonal elements. The mode amplitudes, when not coupled to any ports, obey the equation

$$\frac{d\boldsymbol{a}(t)}{dt} = j\Omega\boldsymbol{a}. \tag{5.17}$$

The modes in $\boldsymbol{a}$ are typically coupled to each other and this coupling is determined by the off-diagonal elements of Ω. As in Section 5.1.1, $|a_i|^2$ is normalized so that it corresponds to the energy stored inside the i-th mode. If there is no loss or gain in the resonator, the energy is conserved and Ω must be Hermitian. If the system is connected to m ports, the CMT equations for the multimode resonator are similar to those of the single mode resonator. In matrix notation, they read

$$\frac{d\boldsymbol{a}(t)}{dt} = \left(j\Omega - \Gamma \right) \boldsymbol{a}(t) + K^T \left| s_+ \right\rangle \tag{5.18}$$

$$\left| s_- \right\rangle = C \left| s_+ \right\rangle + D\boldsymbol{a} \tag{5.19}$$

where Γ is an $n \times n$ Hermitian matrix representing the decay rates, K and D are $m \times n$ coupling matrices, and C is an $m \times m$ scattering matrix describing the direct scattering pathway. Time reversal and energy conservation impose a set of constraints on these matrices. With arguments similar as those developed in 5.1.1, one can show that the following relations must be respected:

$$D^+D = 2\Gamma \tag{5.20}$$

$$K = D \tag{5.21}$$

$$CD^* = -D. \tag{5.22}$$

5.2 Fano resonances

In this section we will derive the transmission, reflection and absorption coefficients of a lossy single-mode cavity coupled to two ports using the framework of Section 5.1. We will then compare these results to the well-known Fano resonance lineshape, where a discrete state (here the mode a with resonance frequency ω_{res}) interacts with a continuum of modes (here the radiation through the ports). This model will be used in Chapter 6 to describe a graphene nanoribbon array. In that case, the mode amplitude a will represent the plasmonic mode inside the plasmonic resonance (see Figure 5.2). We suppose that light is incident only from port 1 (so $s_{2+} = 0$).
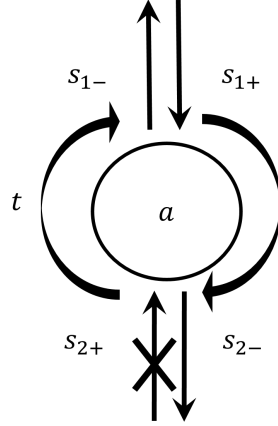
Figure 5.2: Diagram of the coupled mode system used to describe a graphene plasmonic array resonance. The incident and transmitted/ reflected light is represented by the four ports. If one wants to compute the transmission, reflection and absorption coefficients, one of the input port must be set to 0. The plasmonic mode is represented by the mode amplitude $a(t)$ and can couple to light through all the ports.

Moreover, since the system possesses mirror symmetry, we suppose that $d_1^2 = d_2^2$. Then by only considering even plasmonic modes (with respect to the mirror plane), we can set $d_1 = d_2 = d$. From the previous section, we know that d must have the form $\sqrt{2/\tau}e^{j\theta}$ where θ is real. In this case, the scattering matrix also acquires the special form

$$C = e^{j\phi} \begin{pmatrix} r & jt \\ jt & r \end{pmatrix} \tag{5.23}$$

where r, t and ϕ are real and $r^2 + t^2 = 1$. By using Equations 5.10 and 5.15, one finds that the constraint

$$t = \sin(\phi - 2\theta) \tag{5.24}$$

must be respected. For this setup, Equations 5.1 and 5.2 become

$$\frac{da(t)}{dt} = \left(j\omega_{\text{res}} - \frac{2}{\tau} - \frac{1}{\tau_{\text{abs}}} \right) a(t) + \sqrt{\frac{2}{\tau}} e^{j\theta} s_{1+}(t) \tag{5.25}$$

$$s_{2-}(t) = jte^{i\phi} s_{1+} + \sqrt{\frac{2}{\tau}} e^{j\theta} a(t) \tag{5.26}$$

$$s_{1-}(t) = re^{i\phi} s_{1+} + \sqrt{\frac{2}{\tau}} e^{j\theta} a(t). \tag{5.27}$$

Note that here we added a $1/\tau_{\text{abs}}$ to account for losses inside the plasmonic cavity. This loss parameter is not connected to κ and d and is not constrained by energy conservation [83]. We suppose that the incident light in port 1 has a harmonic time dependence $e^{j\omega t}$. Since in this case there are no non-linear properties or time-dependent parameters, $a(t)$ has the same harmonic time-dependence. This allows to rewrite Equation 5.25 as

$$a = \frac{\sqrt{\frac{2}{\tau}} e^{j\theta} s_{1+}}{j\left(\omega - \omega_{\text{res}}\right) + \left(\sqrt{\frac{2}{\tau}} + \sqrt{\frac{1}{\tau_{\text{abs}}}} \right)} \tag{5.28}$$

The transmittance, reflectance and absorptance (T, R, and A respectively) are then given by

$$T = \frac{|s_{2+}|^2}{|s_{1+}|^2}, \quad R = \frac{|s_{1-}|^2}{|s_{1+}|^2}, \quad A = 1 - T - R. \tag{5.29}$$

By using Equations 5.24 to 5.28, one finds the coefficients from Equation 5.29:

$$T(\omega) = \frac{[t(\omega - \omega_{\text{res}}) + r(2/\tau)]^2 + t^2(1/\tau_{\text{abs}})^2}{(\omega - \omega_{\text{res}})^2 + [(2/\tau) + (1/\tau_{\text{abs}})]^2} \tag{5.30}$$

$$R(\omega) = \frac{[r\left(\omega - \omega_{\text{res}}\right) - t\left(2/\tau\right)]^2 + r^2\left(1/\tau_{\text{abs}}\right)^2}{\left(\omega - \omega_{\text{res}}\right)^2 + [(2/\tau) + (1/\tau_{\text{abs}})]^2} \tag{5.31}$$

$$A(\omega) = \frac{(4/\tau)(1/\tau_{\text{abs}})}{(\omega - \omega_{\text{res}})^2 + [(2/\tau) + (1/\tau_{\text{abs}})]^2}. \tag{5.32}$$

This specific type of resonance prevents the transmission to reach a 0 value when losses are present in the cavity. In the lossless case however (when $1/\tau_{\text{abs}} = 0$), Equations 5.30 and 5.31 are the well-known Fano asymmetric lineshapes.

A Fano resonance typically occurs when a discrete energy state interacts with a continuum of energy states. This phenomena was first described by Ugo Fano in 1961 [85] but a special case of Fano resonances had already been studied in 1935 [86]. The Fano resonance extinction cross-section $\sigma(E)$ is described by the general formula [87]

$$\sigma(E) = D^2 \frac{(q + \Omega)^2}{1 + \Omega^2} \tag{5.33}$$

where E is the energy, $q = \cot\delta$ is the Fano parameter describing the asymmetry of the lineshape, δ is the phase shift of the continuum, $\Omega = 2(E - E_0)/\Gamma$ where E_0 and

Γ are the resonator resonance frequency and width, respectively, and $D^2 = 4\sin^2\delta$. This form of $\sigma(E)$ can describe different optical spectra, such as the transmission and scattering, and thus appears in a wide variety of photonic phenomena. For example the scattering of dielectric spheres, rods and stacks of dielectric layers can all be considered as Fano resonances [88–90]. A typical photonic design achieving a Fano resonance is a waveguide coupled to a cavity resonance or to a defect [91, 92]. In the case of a side-coupled cavity, the transmission can be expressed using the Fano formula. The demonstration in the beginning of this Section can actually describe a waveguide coupled to a side-cavity (with losses). This shows that CMT models are fairly general in their formulation and can be used to describe a wide range of coupled systems.

The Fano parameter q is responsible for the symmetric or asymmetric lineshape of the transmission and reflection coefficients. Figure 5.3 shows how the phase shift δ and Fano parameter q affect that lineshape. For cases where $q = \pm\infty$ (or $\delta = n\pi$, with n an integer), the external field does not couple to the continuum. When $q = 0$ (or $\delta = \pi/2 + n\pi$, with n an integer), the cavity mode does not couple to the continuum. These two cases yield symmetric Lorentzian lineshapes. For all other q values, the lineshape is asymmetric and is called a Fano lineshape. In this thesis, the coupled resonances we consider (graphene plasmonic resonances) have a Fano lineshape, because the incident field is coupled to the cavity modes as well as to the continuum modes.

5.3 Perturbation method

In this section, we will describe a method to find an approximate expression for the eigenvalues of a Hermitian matrix. This method is useful to describe non-degenerate eigenvalues, but also very appropriate for two nearly degenerate eigenvalues. This will be employed in Chapter 8 when we deal with an infinite Floquet Hamiltonian, where the unperturbed modes cross and give rise to nearly degenerate eigenvalues. These two unperturbed branches lead to an anti-crossing, and we will use this perturbation method to approximate the eigenvalues in those specific cases.

This section is based on the perturbation method developed by J. Shirley in his thesis [93] in the context of atomic physics, where the coupling between atomic states in an intense field is considered as a time-dependent variable [94]. In this thesis, we will consider time-dependent resonance frequencies (diagonal elements in the initial Hamiltonian) instead of time-dependent coupling coefficients (off-diagonal elements in the initial Hamiltonian), but the perturbation method remains identical.

We start by considering the eigenvalue equation

$$\left(E^0 + V\right) A = AE \tag{5.34}$$

where E^0 and V are given Hermitian matrices, A is the unitary matrix of eigenvectors and E is the diagonal matrix with the unknown eigenvalues. In this equation, the initial Hamiltonian is separated into an unperturbed matrix E^0 and the perturbation matrix V. We also suppose that E^0 is already diagonal. We rewrite Equation 5.34

$$AE - E^0 A = VA \tag{5.35}$$
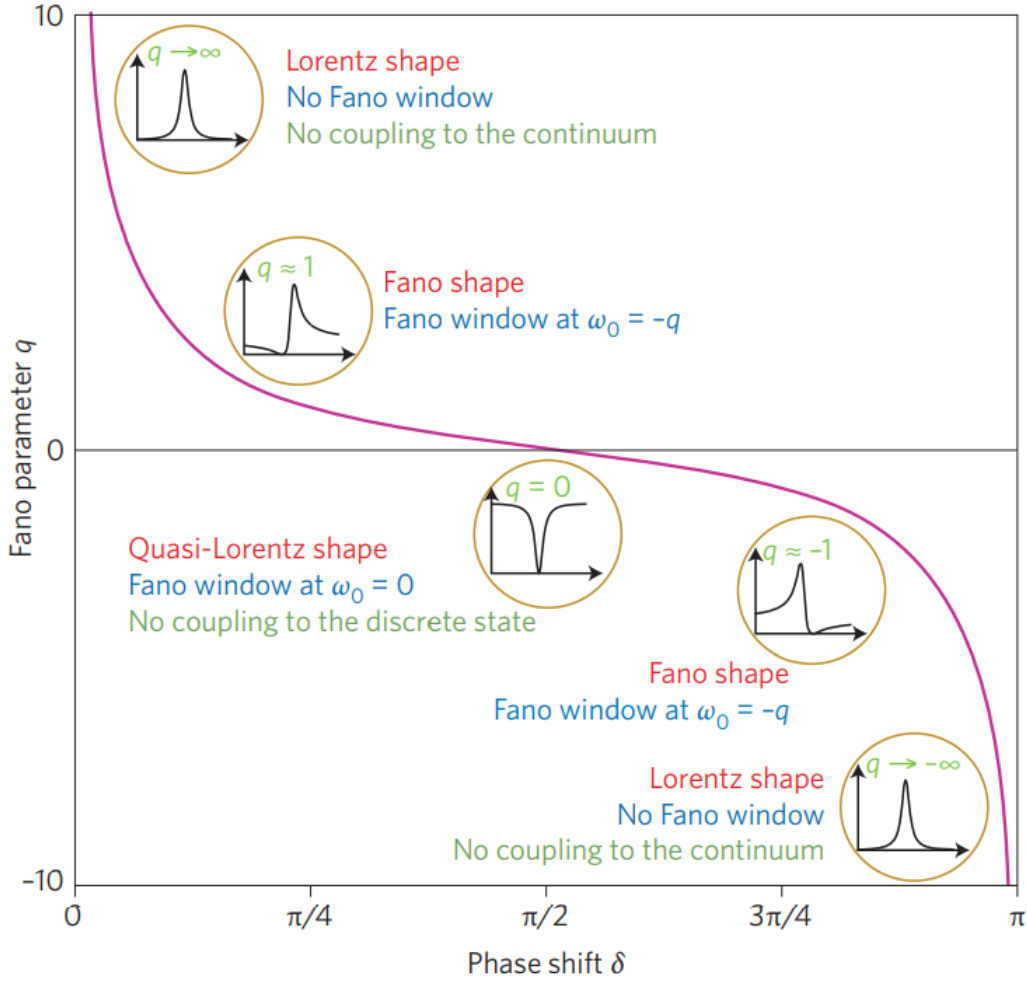
Figure 5.3: Fano parameter as a function of the continuum phase shift and different lineshapes in the corresponding cases [87]. Fano asymmetric lineshapes occur when the Fano parameter is different than 0 and does not take infinite values.

and by writing it out component by component, we find

$$\sum_k \left(A_{ik} E_k \delta_{kp} - E_i^0 \delta_{ik} A_{kp} \right) = \sum_k V_{ik} A_{kp} \tag{5.36}$$

$$A_{ip} E_p - E_i^0 A_{ip} = \sum_k V_{ik} A_{kp}. \tag{5.37}$$

By solving for the eigenvectors A_{ip}, we find

$$A_{ip} = \sum_k \frac{V_{ik} A_{kp}}{E_p - E_i^0}. \tag{5.38}$$

In this notation, p denotes a column (so a particular eigenvector), so A_{ip} is a specific unknown eigenvector component, associated with the unknown eigenvalue E_p. Equation 5.38 is a transcendental equation and we will use approximations to solve it.

We now suppose that two eigenvalues in the unperturbed initial Hamiltonian E^0 are nearly degenerate. This means that terms $E_p - E_i^0$ are small compared to components of V except for two indices $i = p$ and $i = q$. Now when considering Equation 5.38, one notices that two terms (in A_{pp} and A_{qp}) will be large compared to the rest of the sum. We can explicitly separate these terms from the rest of the sum:

$$A_{ip} = \frac{V_{ip} A_{pp}}{E_p - E_i^0} + \frac{V_{iq} A_{qp}}{E_p - E_i^0} + \sum_{k'} \frac{V_{ik'} A_{k'p}}{E_p - E_i^0} \tag{5.39}$$

where k' runs over all the matrix indices except for p and q. The next step is to solve the implicit Equation 5.39 by iteration:

$$
\begin{aligned}
A_{ip} = {}& \left(\frac{V_{ip}}{E_p - E_i^0} + \sum_{j'} \frac{V_{ij'} V_{j'p}}{(E_p - E_i^0)(E_p - E_{j'}^0)} + ... \right) A_{pp} \\
&+ \left(\frac{V_{iq}}{E_p - E_i^0} + \sum_{j'} \frac{V_{ij'} V_{j'q}}{(E_p - E_i^0)(E_p - E_{j'}^0)} + ... \right) A_{qp}.
\end{aligned} \tag{5.40}
$$

By setting $i = p$ in Equation 5.40 and multiplying by $(E_p - E_p^0)$ we find

$$E_p A_{pp} = E_p^0 A_{pp} + \mathcal{V}_{pp}(E_p) A_{pp} + \mathcal{V}_{pq}(E_p) A_{qp} \tag{5.41}$$

with

$$\mathcal{V}_{pp}(E) = V_{pp} + \sum_{i'} \frac{V_{pi'} V_{i'p}}{E - E_{i'}^0} + \sum_{i'} \sum_{j'} \frac{V_{pi'} V_{i'j'} V_{j'p}}{(E - E_{i'}^0)(E - E_{j'}^0)} + ... \tag{5.42}$$

$$\mathcal{V}_{pq}(E) = V_{pq} + \sum_{i'} \frac{V_{pi'} V_{i'q}}{E - E_{i'}^0} + \sum_{i'} \sum_{j'} \frac{V_{pi'} V_{i'j'} V_{j'q}}{(E - E_{i'}^0)(E - E_{j'}^0)} + ... \tag{5.43}$$

We cannot yet solve Equation 5.41 because we cannot cancel A_{pp} terms because of the presence of an A_{pq} term. We need another equation that we obtain by considering Equation 5.40 for $i = q$, and multiplying by $(E_p - E_q^0)$. This gives

$$E_p A_{qp} = E_p^0 A_{qp} + \mathcal{V}_{qp}(E_p) A_{pp} + \mathcal{V}_{qq}(E_p) A_{qp} \tag{5.44}$$

where $\mathcal{V}_{qp}$ and $\mathcal{V}_{qq}$ are defined by similar relations as Equations 5.42 and 5.43. Equations 5.41 and 5.44 can be combined into an equation system:

$$
\begin{pmatrix} E_p^0 + \mathcal{V}_{pp}(E) & \mathcal{V}_{pq}(E) \\ \mathcal{V}_{qp}(E) & E_q^0 + \mathcal{V}_{qq}(E) \end{pmatrix} \begin{pmatrix} A_{pp} \\ A_{qp} \end{pmatrix} = E \begin{pmatrix} A_{pp} \\ A_{qp} \end{pmatrix} \tag{5.45}
$$

which is an implicit equation for the eigenvalues E_p and E_q of the initial eigenvalue problem of Equation 5.34. By diagonalizing the 2 by 2 matrix, we can find these eigenvalues. To solve this implicit equation, we will choose a starting point for E corresponding to an unperturbed energy and compute the $\mathcal{V}_{ij}$ to the first order, to obtain a relatively simple analytical expression. The same procedure can be applied to more than two-fold degenerate cases, but the complexity of the expressions rapidly increases.

5.4   Finite Element Method

In this thesis, we study complex electromagnetic structures both in frequency domain and in time domain. We use numerical simulations methods such as the Finite Element Method (FEM) to solve problems in both cases. We use a commercial package called COMSOL Multiphysics [95, 96] where these numerical tools are readily available.

FEM methods are used to compute the approximation of a Partial Differential Equation (PDE). First the simulation space is divided in a large number of volume elements. This division is called a mesh. All these elements do not have to be equal in size, or in shape. The mesh structure can be chosen depending on the expected form of the solution. Typically, plasmonic modes exhibit a high field enhancement around sharp edges (at the end of ribbons in graphene for example). In those cases, one needs to choose a mesh with smaller elements around these sharp features, while larger mesh elements in free space suffice (typically 10 1D mesh elements per wavelength is adequate). Usually, tetrahedral elements are used in FEM because they allow to closely follow curved boundaries (see Figure 5.4 for a mesh example). However, depending on the symmetry of the structure, other types of elements can be used.
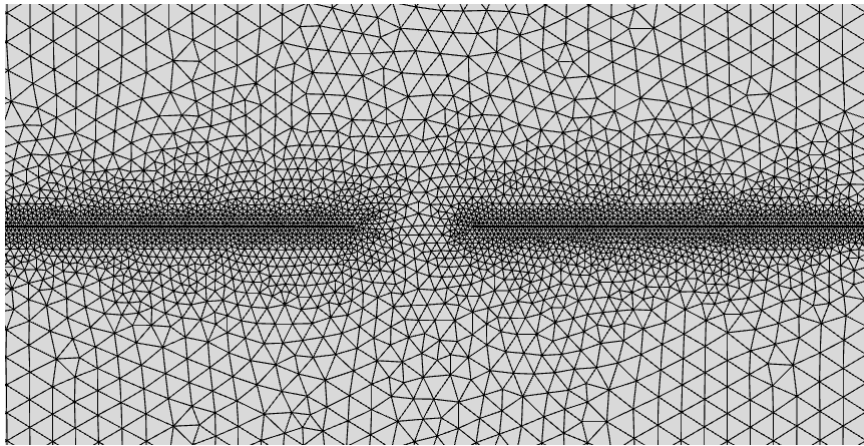
Figure 5.4: Mesh used for a graphene ribbon array. Mesh elements close to the ribbon edges are smaller so the sharp field features occurring at these positions are accurately described. Mesh elements further away become larger but still remain smaller than the vacuum wavelength.

In 2 dimensions, the unknown solution $\psi(x, y)$ is then approximated for each element by

$$\psi(x, y) = \sum_{i=1}^{M} u_i b_i(x, y) \tag{5.46}$$

where b_i is one of the M basis functions chosen for a specific structure. To solve the problem, one needs to find the coefficients u_i for each of the K mesh elements. Then, constraints are introduced at the boundaries to find $M * K$ equations connecting the u_i. Then one needs to find a functional J with variable ψ such that the function ψ that minimizes J will be a solution of the physical problem. Typically, J is

connected with the total power in the system. Since the basis function b_i are chosen in advance, J only depends on the parameters u_i. In other words, one only needs to find the u_i that minimize J, for example by solving the linear system $\partial J / \partial u_i = 0$.

This technique is useful to solve eigenmode and eigenfrequency problems, as well as to obtain numerical values for the scattering matrix of a structure. In this thesis, we used COMSOL Multiphysics where the numerical method described above is readily implemented. We used COMSOL's Stationary solver to find the eigenvalues and eigenmodes of plasmonic structures as well as their response to an external field (to compute transmission, reflection and absorption coefficients).

In addition to these stationary techniques, we used time-dependent FEM to describe the evolution of plasmonic systems when a time-dependent modulation is applied to the system's material properties. We used the Time-Dependent COMSOL solver for these cases. Note that here the method used to solve the problem is different: one needs to solve dynamic PDEs. For these, numerical methods such as Backward Differentiation Formulas (BDF), generalized-α or Runge-Kutta methods can be used. We chose to use the generalize-α methods because they include strategies to minimize losses for high-frequency components. We also imposed a stepsize of $\Delta t = T/40$, where T is the period corresponding to the center frequency of the initial pulse.

Now we will briefly explain how these methods are used throughout this thesis. First, eigenfrequencies and eigenmode results from FEM simulations are used to compute the resonance frequency of plasmonic modes. For example, the resonance frequencies of plasmonic modes in graphene ribbon arrays can be calculated, as well as their dispersion diagram. We also used these to compute the mode profiles in a graphene plasmonic waveguide for Chapter 7. The stationary solver can also be used to get the scattering matrix of a structure. This feature was used to compute the transmission, reflection and absorption spectra of graphene plasmonic arrays. These spectra are then used to extract the CMT parameters of the simulated structure by fitting the CMT transmission expression to the numerical results. This allows us to study the system with the CMT model when CMT parameters are a function of time, as we do in Chapter 6.

The time dependent solver was used to study plasmonic structures where a parameter depends on time. We used this Solver in Chapters 6 and 7. This allows us to compare time-dependent CMT results to time-dependent FEM simulations, and to check that CMT stays accurate when a time dependence is introduced in the system. We also used this solver to study propagative graphene plasmons when graphene properties change dynamically. It is important to note that these simulations are not stationary: a wide range of frequency components are present in the system and with this solver, we are able to describe their evolution, and to characterize frequency changes that occur during the simulation time.

6

Frequency comb generation

Graphene plasmonics has been under intensive investigation these past years [97], as described in Chapter 4. The particular plasmonic modes exhibit very interesting properties such as a strong confinement, a large tunability via the graphene Fermi level and relatively low losses [98]. Arrays of graphene elements like disks [99] or ribbons [76, 100] lead to remarkable properties such as coherent perfect absorption [75].

In another line of research time modulation is studied to realize very special optical functions, such as optical isolation [26], wavelength conversion [16, 101], effective magnetic fields [37, 102], topological states of light [35, 38] and more recently comb generation [103, 104]. Indeed, time modulation proves useful to break certain symmetry constraints, for example in metasurfaces [105]. Furthermore, experimental devices have already been built, amongst others to realize interband photonic transitions in waveguides [28] or non-reciprocal acoustic circulators [25], demonstrating the experimental feasibility of such modulations.

Recently, time modulation and graphene were combined to achieve non-reciprocal graphene devices [32], electro-optic modulators with a modulation of 30 GHz [51], and to introduce a new mechanism for frequency comb generation [106]. The latter work shows that a frequency comb can be achieved by sending a monochromatic pulse through a non-patterned graphene sheet with a time-dependent conductivity, generating an output composed of evenly spaced frequency components. These

different spectral lines are separated by the frequency of the modulation applied to the graphene sheet. In essence, the input signal becomes interrupted or screened by the sheet in its high-conductivity state, leading to a modulated transmission, and new frequency components.

In this chapter we expand upon this comb mechanism by using the interplay of light with a graphene plasmonic cavity. Here, the cavity mode corresponds to the plasmonic resonance of a patterned graphene ribbon grating with a time-dependent conductivity. The grating structure is needed to obtain a resonance, as the incoming light cannot excite plasmonic modes in a pristine graphene sheet.

With suitable parameters the grating mode drastically enhances comb generation requiring smaller Fermi level modulations, in comparison with the planar sheet. In our method we tune the incoming signal close to a strong resonance, and the graphene modulation periodically switches the signal in and out of resonance, leading to strong transmission modulations. Because the procedure works with a shifting resonance, instead of a non-resonant screen modulation, we need much smaller modulations of the graphene Fermi level.

For this analysis we employ an accurate and efficient temporal coupled-mode theory (CMT) model [81, 82], which is validated with finite element method (FEM) simulations. With CMT we can show how the frequency comb is tuned via the grating's structural parameters. Subsequently, the interplay between the cavity mode lifetime and the modulation time is elucidated. We first examine the general optical properties of graphene gratings (Section 6.1) and show that the plasmonic resonances in these arrays exhibit a high sensitivity to the Fermi level (Section 6.2). We demonstrate how these systems can be modelled with CMT first in the 'static' case (Section 6.3) and we compare our theoretical model with realistic simulations to extract the parameters of our CMT model. Then we extend the model to dynamical structures, where the resonant frequency of the system becomes a function of time and generates frequency combs (Section 6.4). We compare FEM simulations with the CMT predictions and show an excellent agreement between those two approaches. Furthermore, using the CMT model we provide insight into the cavity dynamics and its coupling with incoming light. Next we compare the combs of graphene gratings with those of a non-patterned sheet and show that the patterned case is a significant improvement since the Fermi level modulations needed to achieve similar combs are smaller by three orders of magnitude (Section 6.5). In the penultimate section we link the grating and time modulation parameters to the generated frequency combs (Section 6.6) before concluding. This chapter is based on the work published in [10].

6.1   Graphene ribbon lattice

In this section we briefly describe the structure under investigation: a lattice of graphene nanoribbons under normal light incidence (Figure 6.1). The structure is periodic in the direction of the ribbon small axis (x), and infinite in the direction of the ribbon long axis (z). This type of grating can be fabricated by chemical vapor deposition, optical lithography and plasma etching [76]. Nanoribbon arrays can also be produced using helium ion beam lithography [65], achieving ribbon widths down to 5 nm with remarkable precision, as described in Chapter 3.
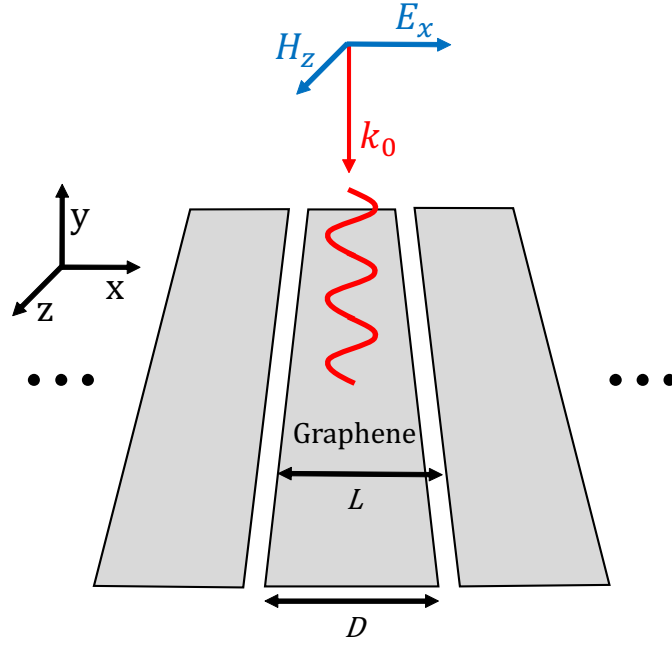
Figure 6.1: Infinite lattice of graphene ribbons, with lattice period L and ribbon width D. We use normal TM incidence to couple with the leaky plasmonic modes of the lattice (fields are depicted in blue, k_0 is the free space propagation constant).

For the two-dimensional FEM simulations graphene is modelled as a current line with conductivity that follows a Drude-like model [41, 107]:

$$\sigma(\omega) = \frac{e^2 E_F}{\pi \hbar^2} \frac{-j}{\omega - j\tau_{\text{gra}}^{-1}} \tag{6.1}$$

This expression is valid when the graphene Fermi level $E_F \gg k_B T$, with $k_B T \approx 0.026$ eV at room temperature. The parameter τ_{gra} accounts for electron scattering (we use $\tau_{\text{gra}} = 10$ ps [74]). Since this expression only takes into account intraband electronic transitions, it is valid for $\hbar\omega \ll E_F$. As we work in the infrared range and with rather high Fermi levels this assumption is satisfied. The graphene conductivity as a function of the frequency is represented in Figure 6.2. It is clear that the conductivity depends on the Fermi level, therefore, in later sections we will exploit a time-dependent Fermi level for dynamic modulation of the conductivity.

We first investigate the (static) optical properties of the grating by carrying out FEM simulations with COMSOL Multiphysics [95] to compute the transmittance, reflectance and absorptance spectra (Figure 6.3) for a graphene grating with period $L = 10\,\mu\text{m}$, ribbon width $D = 8.75\,\mu\text{m}$ and $E_F = 0.635$ eV. We obtain three resonances: a broad fundamental mode at low frequency, and two narrower higher-order modes. The higher-order modes have slightly asymmetric lineshapes, which is characteristic of Fano resonances. It indicates the interference between a broadband, 'background' transmission, with the narrowband mode [83, 108] (as described in Chapter 5).

For the incident light frequency and grating period we consider, there are no (non-zeroth) Bragg diffraction orders in the surrounding air (the incident light has
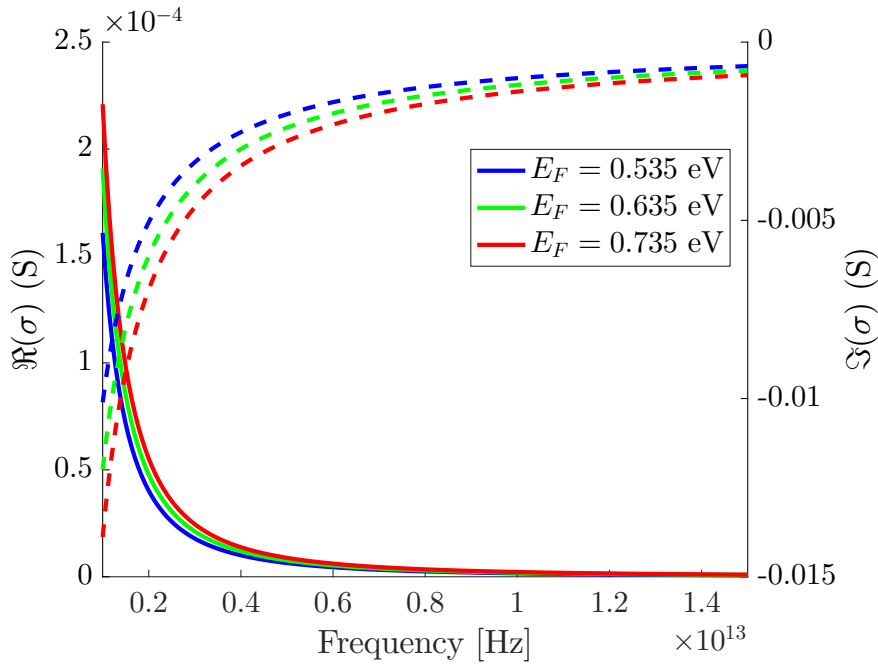
Figure 6.2: Real (solid lines) and imaginary parts (dashed lines) of the graphene conductivity of Equation 6.1 for various Fermi levels. At these frequencies graphene is metallic and supports plasmonic modes in graphene sheets and graphene ribbon lattices.

a frequency of the order of 10 THz that gives a vacuum wavelength of 30 μm and the lattice period is $L = 10$ μm giving a ratio $L/\lambda = 0.3$). One should note that only even modes are excited because of the parity of the incident light [109]. We can understand each resonance in Figure 6.3 as a coupling to a plasmonic cavity array mode.

6.2   Dependence on the Fermi level

A key element required to generate frequency combs in this setting is that the resonances of Figure 6.3 are sensitive to the graphene Fermi level. This will allow us to modulate E_F and change the resonance frequencies of the plasmonic modes. Thus we need to know the dependence of the modal parameters on the Fermi level to develop an analytic model describing this comb generation mechanism.

We compute with FEM the transmittance of the grating as a function of the frequency and the Fermi level (Figure 6.4). The resonance frequency strongly depends on the Fermi level, whereas the other parameters τ and τ_{abs} (influencing the shape of the resonance) are fairly independent of E_F. Moreover, we obtain a linear expression $f_{\text{res}}(E_F) = 1.46 \times 10^{13}$Hz eV$^{-1}E_F + 6.23 \times 10^{11}$Hz that links the resonance frequency to the Fermi level for a given lattice geometry (green line in Figure 6.4).

The lattice resonances lead to a transmission that depends much more strongly on the Fermi level than in the planar case. To show this in detail we look at the transmission of a free-standing graphene sheet [110], and compare it with the lattice
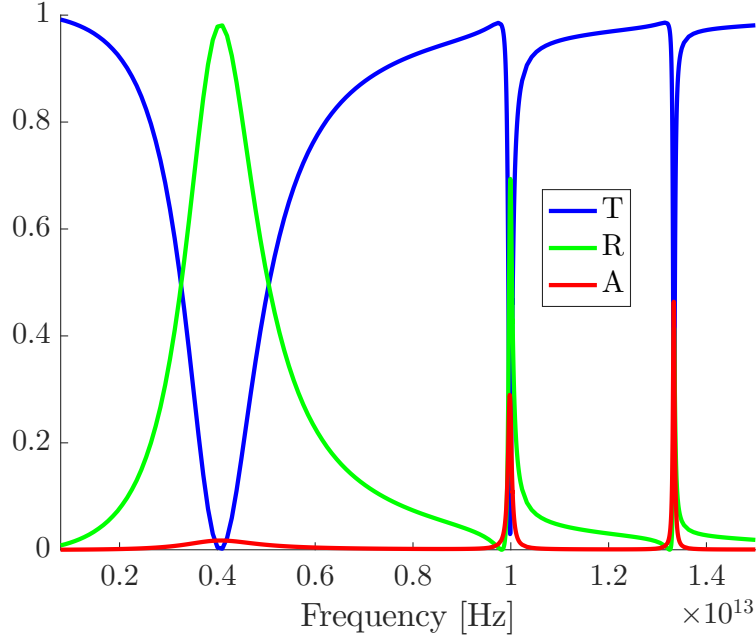
Figure 6.3: Transmittance T, reflectance R and absorptance A of a graphene grating with $L = 10\,\mu m$, $D = 8.75\,\mu m$ and $E_F = 0.635$ eV calculated with FEM. Each dip in transmission indicates the presence of a plasmonic mode that matches the parity of incident light and lies above the light line thus allowing coupling with radiation.

case. The Fresnel coefficients for free standing graphene are

$$f_{\text{fresnel}}(\omega, E_F) = 1 - r_{\text{fresnel}}(\omega, E_F) \tag{6.2}$$

$$r_{\text{fresnel}}(\omega, E_F) = \frac{\sigma(\omega, E_F)\eta}{[\sigma(\omega, E_F)\eta + 2]} \tag{6.3}$$

where f_{fresnel} and r_{fresnel} are the Fresnel transmission and reflection coefficients, respectively, and η is the vacuum impedance. These Fresnel coefficients give the transmittance and reflectance via: $T = |f_{\text{fresnel}}|^2$ and $R = |r_{\text{fresnel}}|^2$. In Figure 6.5 we compare Equations 6.2 and 6.3 (solid lines) to FEM simulation results (dots) where we use the Drude conductivity of Equation 6.1 with $\omega = 2\pi \times 10^{13}$ rad/s, $E_F = 0.635$ eV and $\tau_{\text{gra}} = 10^{-11}$ s. These results are obtained at normal incidence. We also plot the transmittance and reflectance from FEM simulations for the grating considered in the previous section (dashed lines). From Figure 6.5 it is clear that the transmission does not change significantly with small E_F variations in the planar case, whereas the lattice case exhibits a strong sensitivity on the Fermi level.

6.3 CMT model of graphene ribbon arrays

We can fit each resonance of the spectrum in Figure 6.3 with a CMT model [81, 82], which allows us to extract the cavity properties (such as its resonance frequency, coupling coefficients and absorption losses). We only need a model with a single resonant mode with amplitude $a(t)$, coupled to two ports $s_{1,2\pm}(t)$, as introduced in
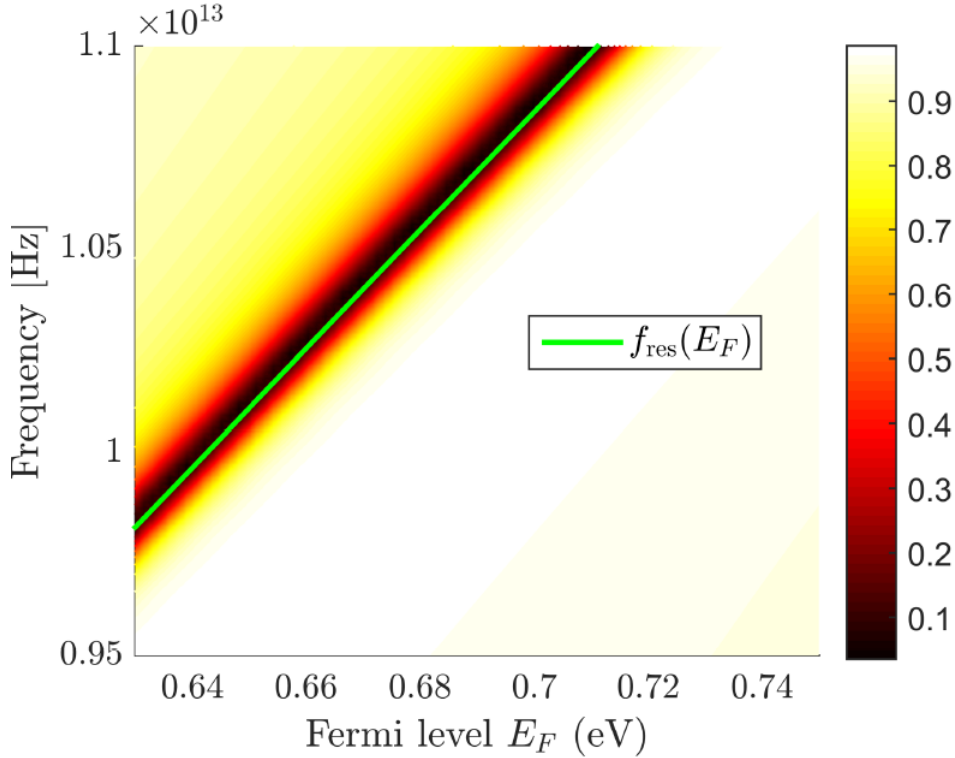
Figure 6.4: Transmittance as a function of incident frequency and Fermi level. The dip in transmittance corresponds to a plasmonic resonance (middle peak in Figure 6.3). The resonance frequency is a linear function of the Fermi level (green line). The shape of the resonance remains unchanged, meaning that the coupling coefficients do not depend on E_F.

Chapter 5 (see Figure 6.6). These quantities are normalized so that $|a(t)|^2$ is the energy inside the cavity, and $|s_{1,2\pm}(t)|^2$ is the power flowing through the ports.

In our situation, incident light only comes from the top of our structure (port 1), so $s_{2+} = 0$. Furthermore, the system is symmetric so that the cavity coupling is the same for both ports: $\kappa_1 = \kappa_2 = \kappa$ and $d_1 = d_2 = d$. In a lossless cavity time-reversal symmetry also requires that $\kappa = d$. Here, our system exhibits losses so we add a term $1/\tau_{\text{abs}}$ accounting for absorption in the cavity, which is separate from the cavity external coupling: the total cavity decay rate $1/\tau_{\text{tot}} = 2/\tau + 1/\tau_{\text{abs}}$ is the sum of the decay rates from the coupling to the (two) outgoing ports $1/\tau$ and the absorption rate in the cavity $1/\tau_{\text{abs}}$.

Furthermore, the slightly asymmetric Fano lineshapes indicate a direct transmission channel f, for light passing the structure without interaction with the particular mode. With these assumptions the CMT equations become:

$$\frac{da(t)}{dt} = \left(j\omega_{\text{res}} - \frac{1}{\tau_{\text{tot}}} \right) a(t) + \kappa s_{1+}(t) \tag{6.4}$$

$$s_{2-}(t) = \kappa a(t) + j e^{j\phi} f s_{1+}(t) \tag{6.5}$$

where ω_{res} is the resonance frequency of the cavity. Time-reversal arguments and energy conservation require that $\kappa = e^{j\theta}\sqrt{2/\tau}$ [81, 83]. One of the phases θ or ϕ can
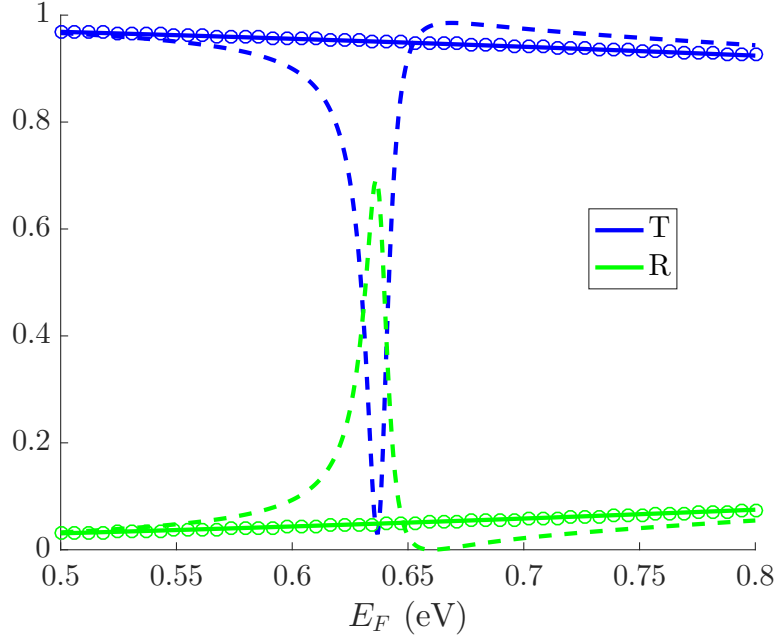
Figure 6.5: Transmittance T and reflectance R of a graphene sheet as a function of E_F from Equations 6.2 and 6.3 (solid lines), and from FEM simulations (dots). FEM simulation results for the lattice case with $L = 10\,\mu\text{m}$ and $D = 8.75\,\mu\text{m}$ are shown in dashed lines. The lattice case exhibits a strong dependence on the Fermi level whereas in the planar case this dependence is much weaker.

be chosen arbitrarily by a choice of reference planes, but time-reversal arguments require that $\theta = [\arcsin(f) + \phi - \pi]/2 + k\pi$, where k is an integer.

This model allows to find expressions for the transmittance, reflectance and absorptance spectra of such a cavity. They read:

$$T(\omega) = \frac{|s_{2-}|^2}{|s_{1+}|^2} = \frac{[f(\omega - \omega_{\text{res}}) + r(2/\tau)]^2 + f^2(1/\tau_{\text{abs}})^2}{(\omega - \omega_{\text{res}})^2 + [(2/\tau) + (1/\tau_{\text{abs}})]^2} \tag{6.6}$$

$$R(\omega) = \frac{|s_{1-}|^2}{|s_{1+}|^2} = \frac{[r(\omega - \omega_{\text{res}}) - f(2/\tau)]^2 + r^2(1/\tau_{\text{abs}})^2}{(\omega - \omega_{\text{res}})^2 + [(2/\tau) + (1/\tau_{\text{abs}})]^2} \tag{6.7}$$

$$\begin{aligned} A(\omega) &= 1 - T(\omega) - R(\omega) \\ &= \frac{(4/\tau)(1/\tau_{\text{abs}})}{(\omega - \omega_{\text{res}})^2 + [(2/\tau) + (1/\tau_{\text{abs}})]^2} \end{aligned} \tag{6.8}$$

where $r = \sqrt{1 - f^2}$. We then fit the parameters for the CMT spectrum (a fit to the transmittance spectrum of Equation 6.6 suffices to extract all parameters) around a specific resonance to the FEM simulations (Figure 6.7). This analysis is easily generalized for other resonances by adjusting the CMT model parameters accordingly. Finally, the obtained parameters are $\tau = 4.67 \times 10^{-12}$ s, $\tau_{\text{abs}} = 1.01 \times 10^{-11}$ s, $f = -0.98$ and $\omega_{\text{res}} = 2\pi\, 1.08 \times 10^{13}$ rad/s. Here, we use a dispersionless graphene sheet: we work around a frequency of 10 THz ($\omega = 2\pi \times 10^{13}$ rad/s) so we use a conductivity value corresponding to that frequency for the forthcoming results.
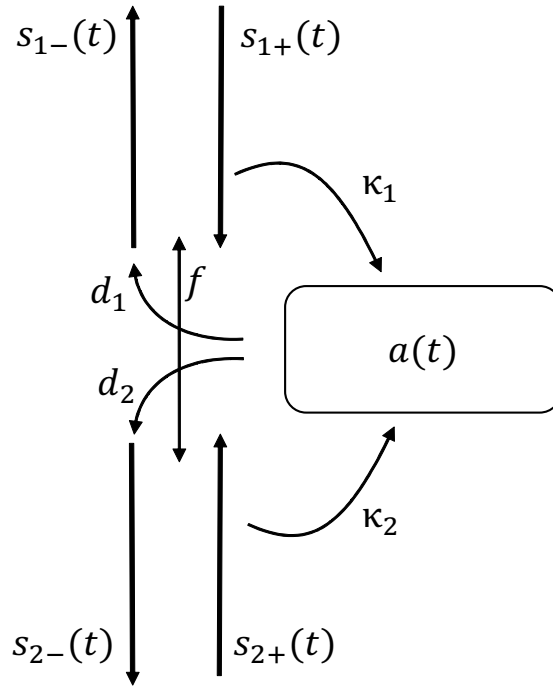
Figure 6.6: Schematic of the CMT model. The cavity models a single plasmonic resonance of the lattice coupled to two ports. The direct channel (f) accounts for light that passes through the grating without interacting with the plasmonic mode.

We use this assumption because the graphene conductivity is not very dispersive at these frequencies.

We now know the CMT parameters for the graphene ribbon arrays. These parameters are tunable via the lattice properties such as the ribbon spacing [74] or the graphene Fermi level E_F, as we exploit in the next sections.

6.4 Dynamic CMT model

The main focus of this chapter is frequency comb generation. In order to achieve this, we use the graphene lattice and apply a dynamic modulation: the Fermi level E_F (and thus conductivity) of the graphene ribbons will be a function of time. This can be achieved by applying a gating voltage to the graphene lattice [48, 50, 76, 111]. The exceptional tunability with gating voltage originates both from graphene's 2D structure and the low density of states around the Fermi level, allowing carrier concentration changes to significantly shift the Fermi level [49].

As seen in Figure 6.4, the cavity resonance frequency ω_{res} strongly depends on E_F so ω_{res} will indirectly be a function of time. Explicitly, we adjust the CMT Equation 6.4 as:

$$\frac{da(t)}{dt} = \left\{ j\omega_{\text{res}}[E_F(t)] - \frac{1}{\tau_{\text{tot}}} \right\} a(t) + \kappa s_{1+}(t) \tag{6.9}$$

while Equation 6.5 is unchanged. Thus, we suppose that the coupling coefficients, decay rates and direct transmission do not depend on the Fermi level (indeed, the
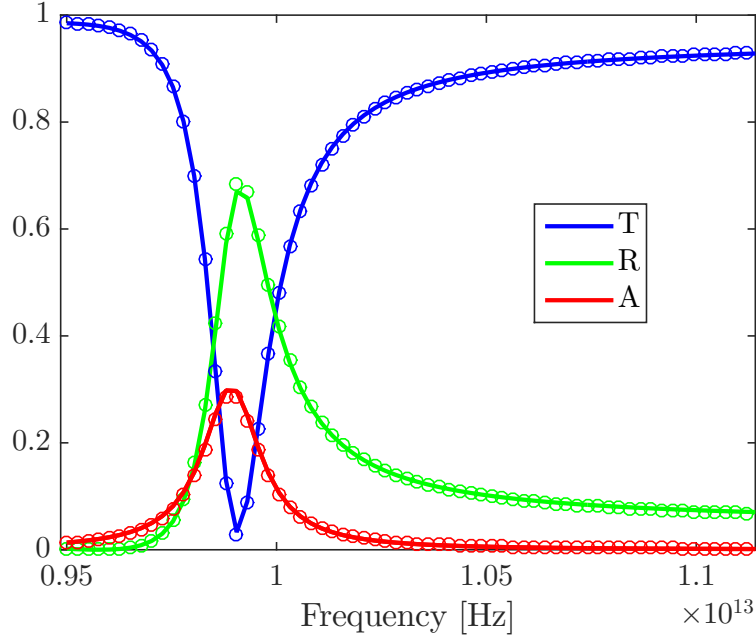
Figure 6.7: FEM simulation results (dots) and CMT fit (solid lines) of the transmittance, reflectance and absorptance spectra of a graphene grating near a plasmonic resonance (second peak in Figure 6.3). The CMT model allows for a good fit with the FEM results.

shape of the transmission spectrum remains unchanged with respect to E_F in Figure 6.4).

We solve Equation 6.9 with a nearly monochromatic Gaussian input pulse:

$$s_{1+}(t) = \exp\left[-(t - t_0)^2/q^2\right] \exp\left[j\omega_0(t - t_0)\right], \tag{6.10}$$

where q gives the width of the pulse, ω_0 is the pulse central angular frequency, t_0 is the pulse center time. For the dynamics we use a sinusoidal modulation $E_F(t)$:

$$E_F(t) = \frac{E_{F\max} - E_{F\min}}{2} \sin(\omega_{\mathrm{mod}}t) + \frac{E_{F\max} + E_{F\min}}{2}, \tag{6.11}$$

where $E_{F\min}$ ($E_{F\max}$) is the minimum (maximum) Fermi level of the grating during the modulation, and ω_{mod} is the modulation frequency.

The Fermi level and resonance frequency are linked: ω_{res} is a linear function of E_F (Figure 6.4). Thus ω_{res} has the same periodicity as $E_F(t)$, and since we know the exact dependence $\omega_{\mathrm{res}}[E_F(t)]$ we can numerically solve Equation 6.9. The cavity amplitude $a(t)$ is then injected in Equation 6.5 to get the output $s_{2-}(t)$.

The peak chosen for Figures 6.4 and 6.7 exhibits a strong dependence on the Fermi level. This is a key element to enable frequency comb generation: if the resonance frequency of the plasmonic mode does not strongly depend on the Fermi level, there will be no efficient modulation of the resonance frequency, then the response via the graphene conductivity changes only slightly, leading to similar results as in the planar case. One can show that the resonance frequency dependence on the Fermi level becomes stronger as the mode order increases (this can be seen in

Figure 4.7 for example). The peak chosen here is the result of a trade-off: it is not too narrow (we do not need to have a sharp pulse in the frequency domain and thus not an excessively long simulation time) and it exhibits a dependence on the Fermi level sufficient to enable efficient frequency comb generation. However this analysis can be applied to any of the (even) plasmonic resonances of the graphene array.

Now we compare results predicted by our CMT model with FEM simulations. The static graphene lattice parameters are the same as in Section 6.1. For the modulation we use $E_{F\min} = 0.62$ eV, $E_{F\max} = 0.65$ eV and $\omega_{\mathrm{mod}} = 2\pi \times 10^{11}$ rad/s. For the pulse parameters $\omega_0 = 2\pi\, 0.99 \times 10^{13}$ rad/s and $q = 1250/\omega_0$. These parameters are chosen so that ω_0 is close to the dynamic resonance frequency $\omega_{\mathrm{res}}(t)$ during the modulation, and the pulse length q is longer than the modulation period. This allows the peaks in the frequency comb to be separate from each other: q is linked to the frequency width of the pulse, and the spacing between the comb peaks is given by the modulation frequency.

In order to validate the CMT model, we compare it with rigorous time domain FEM simulations using COMSOL Multiphysics. By fitting the transmission from the CMT model (Equation 6.6) to our static simulation results (Figure 6.7), we already established the parameters for the CMT model for a graphene grating with $L = 10\,\mu$m, $D = 8.75\,\mu$m and $E_F = 0.635$ eV.

We then numerically solve the CMT equations with the pulse from Equation 6.10. The pulse $s_{1+}(t)$ is a nearly monochromatic signal whereas the output $s_{2-}(t)$ is a frequency comb (Figures 6.8(a) and 6.8(c)).

In FEM simulations, the pulse is a TM wave sent at normal incidence on the graphene grating (as shown in Figure 6.1), so the electric field $E_x(t)$ in the input port is a gaussian pulse given by Equation 6.10. The output field amplitude E_x obtained in the output port from FEM simulations is then represented in Figures 6.8(b) and 6.8(c) in time and frequency domain, respectively.

The output s_{2-} from CMT is represented in Figures 6.8(a) and 6.8(c) in time and frequency domain, respectively. The spacing between the frequency peaks of the comb is exactly equal to the modulation frequency ω_{mod} applied to the graphene grating. The output field amplitude E_x from FEM simulations is represented in Figures 6.8(b) and 6.8(c) in time and frequency domain, respectively. All the results in the frequency domain are normalized with the incident pulse maximum amplitude.

Results obtained using the very simple CMT model are in excellent agreement with the simulation results both in time and frequency domain. The time and frequency features are almost perfectly replicated by Equations 6.9 and 6.5 even though the physical process is a complex interplay between time modulation, a graphene plasmonic resonance, and the incident light. Since the main condition for this comb generation mechanism is the modulation of a resonance frequency, this method can be generalized to many other physical systems that meet these requirements. Furthermore, the CMT model is very simple to solve numerically, therefore we will use it now to analyze the comb mechanism in detail.

In the remainder of this section, we provide insight into the modulated cavity dynamics using the CMT model. Figure 6.9(a) shows the solution $|a(t)|^2$ (in blue) for a smaller modulation frequency $f_{\mathrm{mod}} = 0.01$ THz and a longer pulse ($q = 12500/\omega_0 \ll 1/\omega_{\mathrm{mod}}$ which is needed so that the cavity goes through several
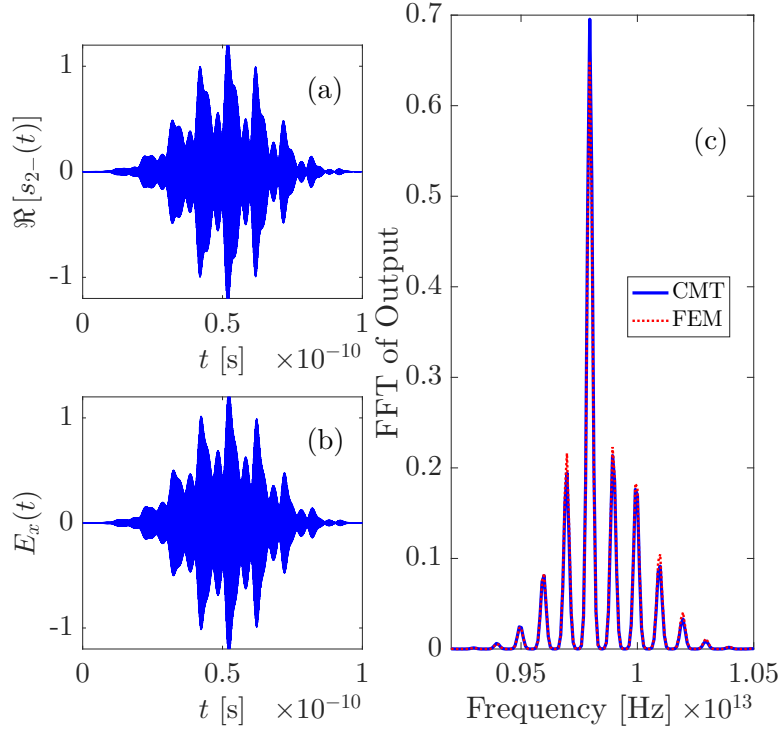
Figure 6.8: (a) Result of CMT calculations for the output $\Re(s_{2-})$ in time domain and (b) result of FEM simulations for the outgoing electric field E_x in time domain. (c) Results of FEM simulations for the outgoing electric field E_x in frequency domain (red) and CMT calculations for the output $\Re(s_{2-})$ in frequency domain (blue). The CMT model allows to perfectly replicate the FEM results both in time and frequency domains.

modulation periods during the pulse) with the same parameters as in the beginning of the section: $E_{F\text{min}} = 0.62$ eV, $E_{F\text{max}} = 0.65$ eV and $\omega_0 = 2\pi\,0.99 \times 10^{13}$ rad/s. A measure of the instantaneous absorption of the cavity, which we call $A_{\text{inst}}(t)$, is represented in red in Figure 6.9(a). This is the absorptance value (red curve in Figure 6.7) where the static resonance frequency is replaced by the instantaneous cavity resonance frequency $\omega_{\text{res}}(t)$ at a given time.

This figure illustrates the mechanisms taking place: when the cavity resonance frequency ω_{res} matches the frequency of the incident light ω_0, the instantaneous absorption coefficient increases because light couples to the lossy cavity ($|a(t)|^2$ increases). When ω_{res} and ω_0 are different, light does not interact with the cavity and the field amplitude decays with the rate $1/\tau_{\text{tot}}$. During this decay new frequency components are generated because the light is trapped inside the cavity and follows its time-dependent resonance frequency.

This mechanism is also illustrated in Figure 6.9(b), showing the dynamic resonance frequency of the cavity as a function of time $f_{\text{res}}(t)$, and the constant incident light frequency f_0 (horizontal blue line). When those two frequencies are equal, so when f_{res} sweeps through f_0, we see that $A_{\text{inst}}(t)$ increases (Figure 6.9(a)) and light couples into the cavity.
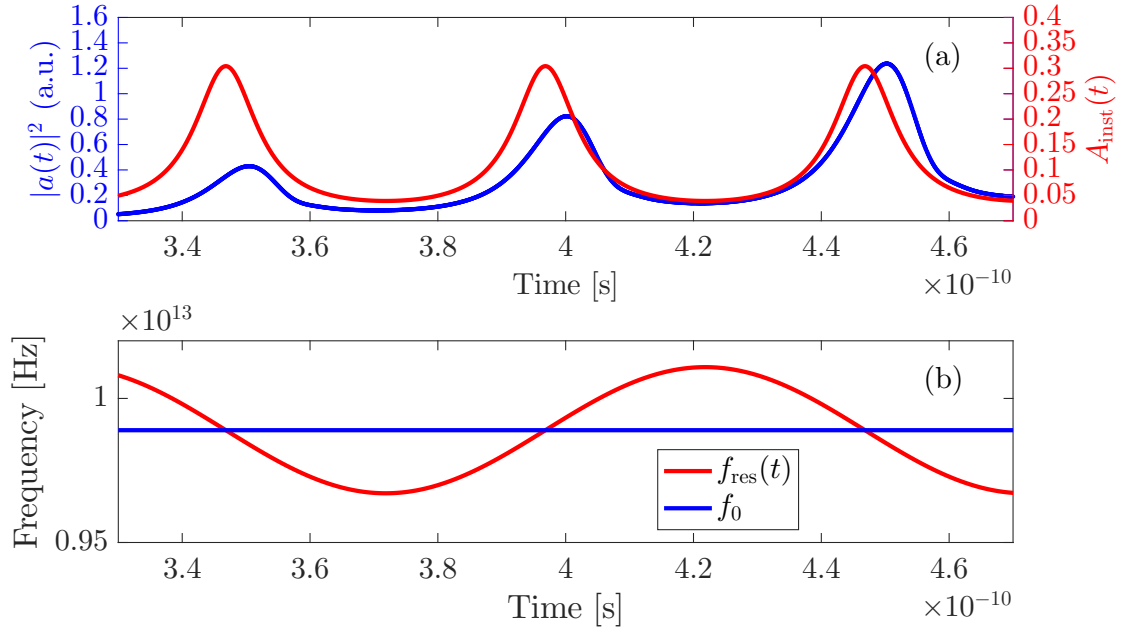
Figure 6.9: (a) Solution $|a(t)|^2$ of the CMT equations in blue. The instantaneous absorption of the cavity is represented in red. (b) Dynamically modulated resonance frequency of the cavity ($f_{res}(t)$ in red) and incident light frequency f_0 (in blue). When these two frequencies are equal, light couples into the cavity.

6.5 Limitations of planar graphene for comb generation

In this section we compare frequency combs generated by a graphene grating and a pristine graphene sheet [106]. The planar mechanism relies on a large change of the sheet conductivity, thus changing considerably the transmission and acting as a shutter for the incident light. On the other hand, the grating effect is quite different, as it exploits plasmonic resonances that cannot be excited by incident light in a planar sheet. The resonances are extremely sensitive to the grating properties, therefore a slight change in Fermi level (also meaning a slight change in conductivity) will lead to a large transmission change, achieving frequency comb generation for a smaller modulation of E_F than in the planar case. Furthermore, other temporal phenomena take place when there are resonances, as we described in Section 6.4 regarding the cavity dynamics. We will determine that the combs generated by the graphene grating require lower Fermi level modulations than in the planar case (of course for specifically chosen parameters: if one were to modulate the grating around frequencies where no plasmonic resonances exist, the effects would be similar for the planar and grating case).

In order to model comb generation in the planar case we use a time dependent Fresnel transmission coefficient [110], and use the same notation for the input $s_{1+}(t)$ and output $s_{2-}(t)$ as we use for the CMT model. The link between the two ports is

now:

$$s_{2-}(t) = f_{\text{fresnel}}\left[E_F(t)\right] s_{1+}(t) \tag{6.12}$$

where f_{fresnel} is the Fresnel transmission coefficient of a free standing graphene sheet at normal incidence [110] of Equation 6.2.

To compare the combs produced by gratings and planar sheets, we examine two similar combs produced by the two structures (Figure 6.10), and check the needed modulation amplitude. To match a comb produced by a graphene lattice (Figure 6.10(a)) with a modulation of $\Delta E_F = 0.03$ eV, one needs a modulation of $\Delta E_F = 10$ eV (not a physically attainable value) in the planar case (Figure 6.10(b)).
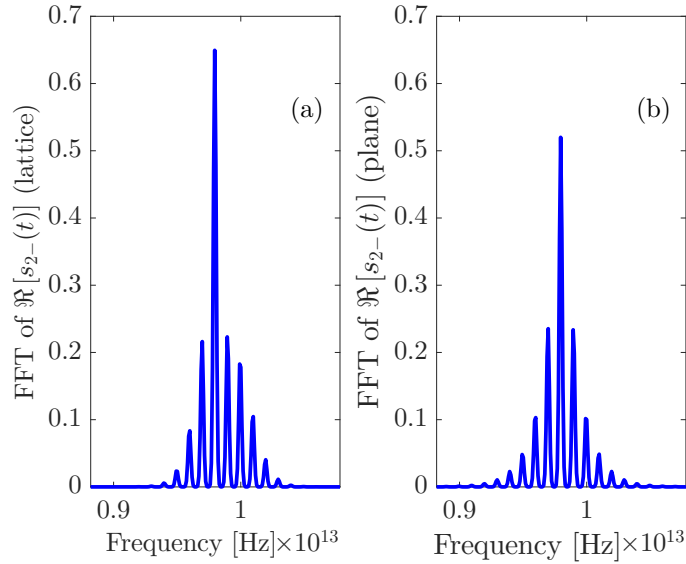
Figure 6.10: Generated frequency combs with (a) a graphene nanoribbon array ($L = 10\,\mu$m, $D = 8.75\,\mu$m and $f_0 = 0.99 \times 10^{13}$ Hz) with Fermi level modulated between 0.62 eV and 0.65 eV (dynamic CMT model results) and with (b) a planar graphene sheet with Fermi level modulated between 0 eV and 10 eV. The lattice case needs Fermi level modulation amplitudes that are three order of magnitude smaller than in the planar case.

This significant improvement occurs because we exploit the sharp spectral features of a graphene grating to efficiently generate frequency combs, whereas the transmission of a graphene sheet is almost constant for a small variation of E_F in the planar case (Figure 6.5). The drastic change in transmission in the lattice case is due to the strong dependence of the cavity resonance frequency, while the change in transmission in the planar case only happens because of the conductivity change.

Note also that the combs in the planar case can only be tuned by choosing the input frequency and the modulation frequency, leading to symmetric outputs, whereas it is possible to obtain asymmetric combs in the lattice case, as discussed in the next section.

6.6   Connecting grating and comb properties

The generated frequency combs in gratings are widely tunable because of the numerous lattice and time modulation degrees of freedom. For the lattice, the ribbon width D, lattice period L, electron relaxation time τ_{gra} and Fermi level E_F determine the shape of the transmission spectrum [74]. Here we have additional parameters concerning the modulation such as its frequency ω_{mod} and bounds $E_{F\text{min}}$ and $E_{F\text{max}}$. In this section we determine how these parameters influence the shape of the generated frequency combs.

Firstly, the different frequency components in the comb are always separated exactly by the modulation frequency. Figure 6.11 shows several outputs produced with different modulation frequencies $f_{\text{mod}} = \omega_{\text{mod}}/(2\pi)$: from $f_{\text{mod}} = 10^{11}$ (foremost curve) to $f_{\text{mod}} = 10^{12}$ Hz (curve at back). The output signal is basically a modulated version of the incident pulse consisting of smaller pulses separated by the period of the modulation (see Figure 6.8(a)). In the frequency domain this corresponds to a frequency comb where the spacing between frequency components is given by the modulation frequency.
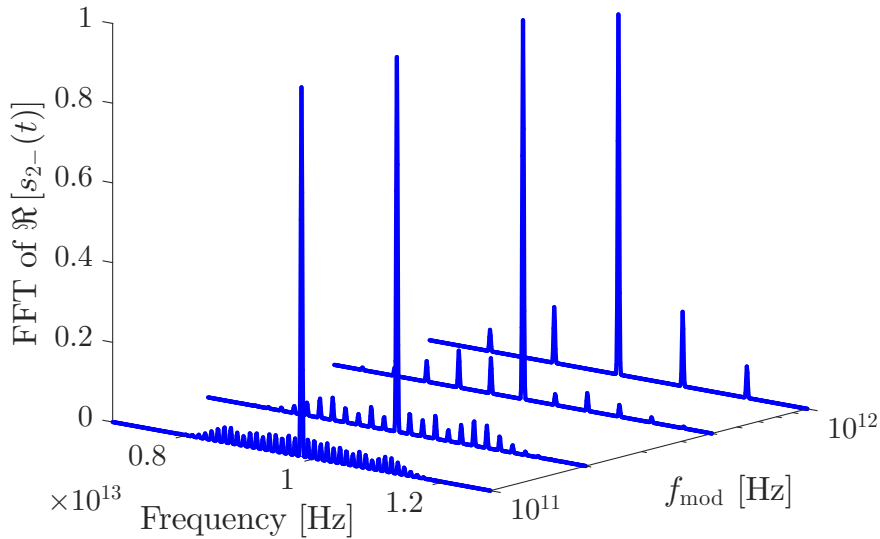
Figure 6.11: Frequency combs generated for several values of f_{mod}. Cavity parameters are the same as those described in Figure 6.7, the pulse is the same as in the beginning of Section 6.4, the modulation has the form of Equation 6.11 with $E_{F\text{min}} = 0.535$ eV and $E_{F\text{max}} = 0.735$ eV. The frequency spacing between the different components of the comb is always equal to f_{mod}.

Furthermore, it turns out that the symmetry of the comb around the input frequency f_0 depends on the minimum and maximum frequency of the cavity during the modulation ($f_{\text{min}} = f_{\text{res}}(E_{F\text{min}})$ and $f_{\text{max}} = f_{\text{res}}(E_{F\text{max}})$, respectively). If one chooses modulation bounds such that $(f_{\text{min}} + f_{\text{max}})/2 = f_0$, the comb will be symmetric with respect to the incident light frequency. By tuning these frequency bounds,

one can shift the comb in the frequency domain (Figure 6.12). When $f_{\max} = f_0$, the maximum frequency of the cavity during the modulation is equal to the incident light frequency (foremost curve in Figure 6.12). The generated frequencies are mainly below f_0, as the cavity resonance remains below f_0 during modulation. For the back curve in Figure 6.12, $f_{\min} = f_0$ so the cavity resonance frequency does not pass below f_0 and the generated frequency components are higher than f_0. This allows to tune the particular frequencies inside the comb and its shape.
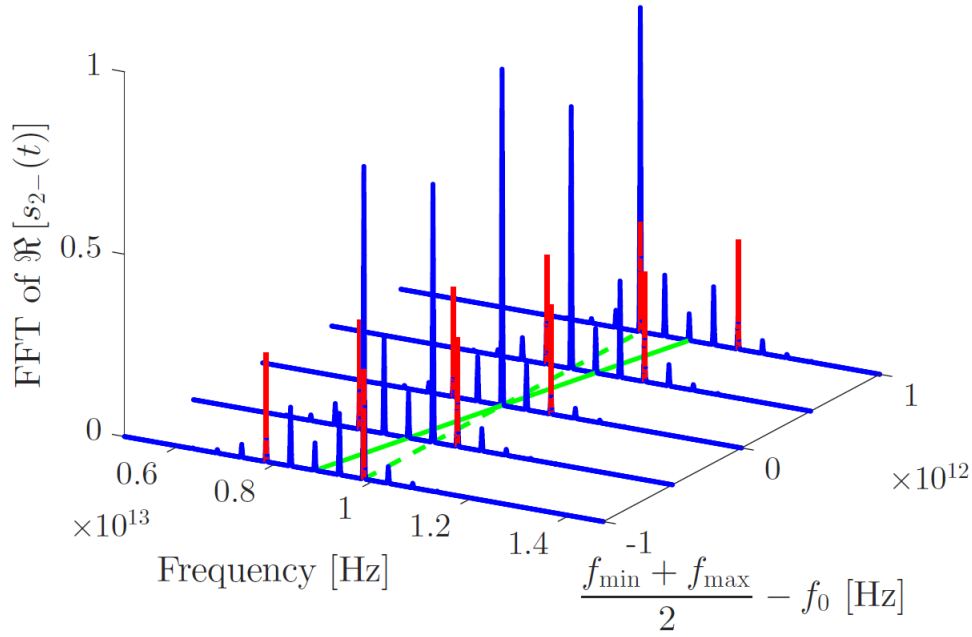
Figure 6.12: Frequency combs generated for different E_F modulation bounds. The vertical red lines represent the modulation bounds $f_{\min} = f_{\mathrm{res}}(E_{F\min})$ and $f_{\max} = f_{\mathrm{res}}(E_{F\max})$, and the green dashed and solid line represent f_0 and $\frac{f_{\min}+f_{\max}}{2} - f_0$, respectively. In this figure $f_{\max} - f_{\min} = 2$ THz is a constant so the comb width remains the same for all the combs.

In addition to shifting the modulation bounds, one can also choose the amplitude of the Fermi level modulation $\Delta E_F = E_{F\max} - E_{F\min}$. In Figure 6.13 we show the frequency combs obtained for different ΔE_F (we choose $f_{\min}$ and $f_{\max}$ so that $(f_{\min} + f_{\max})/2 = f_0$ and thus the combs are symmetric with respect to f_0). As ΔE_F increases, more side frequencies are generated since the cavity frequency goes further away from f_0.

Another important parameter is the external coupling time of the cavity τ (Figure 6.14). If τ increases, the incident light will couple more slowly into the cavity, but will be trapped longer (higher quality factor). If τ decreases, the incident light will couple more rapidly with the cavity, but will also outcouple faster, leading to less build-up. There is a balance between coupling to the cavity and conversion efficiency inside the cavity: if the coupling is very fast (small τ), light does not stay in the cavity long enough to generate frequency components far from f_0 ($\tau = 5 \times 10^{-14}$ s, foremost curve in Figure 6.14): since $1/\tau \gg f_{\mathrm{mod}}$, the light outcouples before the
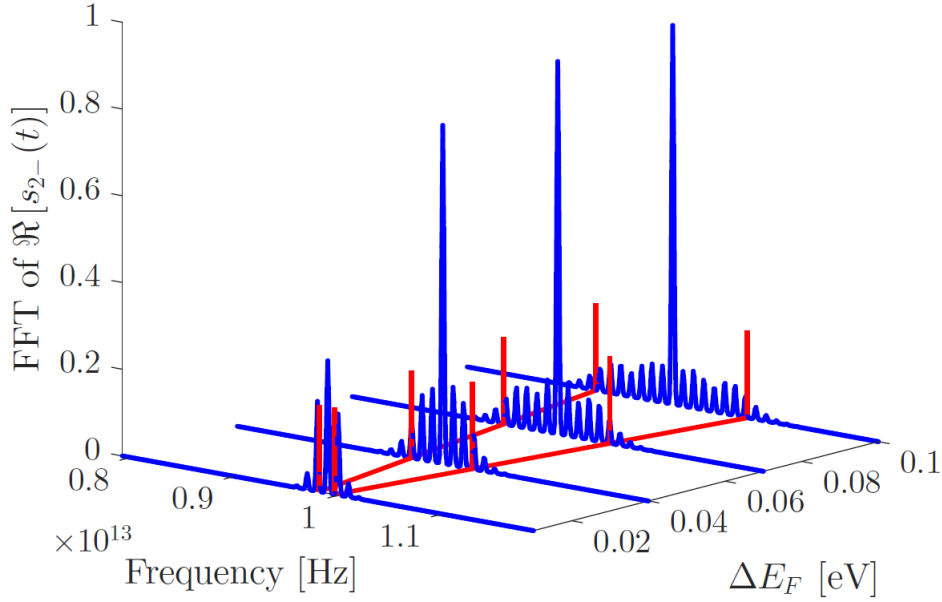
Figure 6.13: Frequency combs generated for different ΔE_F modulation amplitudes from 0.01 eV to 0.1 eV with $f_{\mathrm{mod}} = 10^{11}$ Hz. Red solid lines are a guide to the eye that indicate the frequency modulation bounds, in addition to the vertical red dashed lines. As ΔE_F increases, the combs become wider and more side frequencies are generated.

cavity can reach the bounds of the modulation. As τ increases, the coupling becomes slower, so light stays in the cavity during an entire or multiple modulations. The comb amplitude is weaker, but wider because light stays in the cavity long enough to generate frequency components far from f_0 ($1/\tau > f_{\mathrm{mod}}$, back curve in Figure 6.14 with $\tau = 10^{-11}$ s). There is a trade-off between coupling efficiency (for short τ) and conversion efficiency (long τ) so the frequency comb generation process is overall stronger in-between those two regimes.

It is also possible to tune the comb position in the infrared range. The resonance frequency of a graphene ribbon array can range from near-infrared to far-infrared by choosing the right grating parameters [74]. Since the generated frequency components of the comb have frequencies close to the cavity resonance frequency, it is therefore possible to design graphene devices that can achieve frequency comb generation for a specific frequency range. One should note that for this mechanism to work, the incident light frequency must be close to the resonance frequency of the cavity so light can excite the plasmonic mode.

The proposed mechanism thus allows for tunable frequency combs with a stable inter-peak separation that is given by the modulation frequency. A small spacing between comb peaks is achieved by a lower modulation frequency that is easier to achieve experimentally and of more interest for comb applications. The frequency comb generated with this method can contain a broad range of frequencies and its
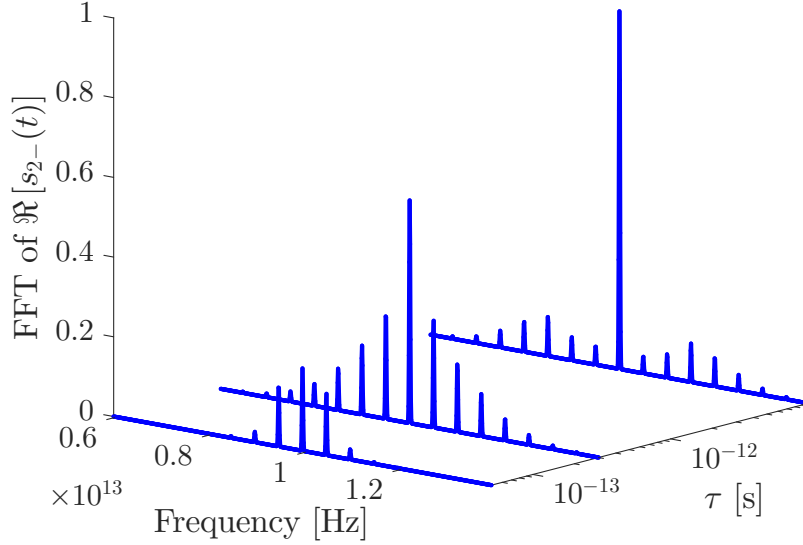
Figure 6.14: Frequency combs generated for different cavity coupling times $\tau = 5 \times 10^{-14}$ s (front curve), 3×10^{-13} s, 1×10^{-11} s (back curve). Here $\tau_{\mathrm{mod}} = 1/f_{\mathrm{mod}} = 2 \times 10^{-12}$ s. For small τ (front curve) the cavity outcouples too rapidly, so generation is less efficient. For large τ (back curve) the cavity couples too slowly, so the combs become weaker again.

bounds broaden by using larger Fermi-level modulations, allowing to bridge over frequency regions in the near and far-infrared.

6.7 Conclusion

We conclude that frequency comb generation can be achieved much more efficiently than with a planar graphene sheet by using the interaction between a plasmonic mode and time modulation, requiring modulation amplitudes that are three orders of magnitude smaller. We study the modes of a graphene grating with a time-dependent Fermi level, and present a simple model based on CMT to describe its properties. The rigorous FEM simulations are in excellent agreement with our CMT model, both in the static and dynamic cases.

Using CMT we show that the frequency combs are highly tunable. The spacing between the different frequency components inside the comb is always equal to the modulation frequency applied to the grating. The frequency bounds of the comb can be chosen by tuning the Fermi level modulation bounds. The coupling coefficient of the cavity determines how strongly light will interact with the plasmonic mode and thus how efficiently light will be converted to new frequency components. Finally the resonant mode in the graphene grating can be chosen over a wide range of wavelengths, ranging from mid-infrared to far-infrared, because of the tunability of the geometry and the material.

We compare the grating results with non-patterned graphene sheets, the former leading to much more efficient frequency comb generation, even for small Fermi level modulations. This is a consequence of the underlying mechanism. In the grating case the plasmonic mode is tuned in and out of resonance, which can be achieved by modest gating changes. In the planar case the non-resonant screen needs to become opaque, requiring much stronger modulations.

In the end, highly tunable and efficient frequency comb generation should be achievable in the mid- and far-infrared using graphene structures. Moreover, the mechanism is fairly general and can be applied to any cavity with a time-modulated resonance frequency that couples efficiently to input and output ports.

7

Time reflection and time refraction of graphene plasmons

In this chapter, we study the interaction of graphene plasmons with single and double temporal discontinuities or shocks, leading to controlled in-plane scattering. We show that a dynamical change of material properties during graphene plasmon propagation induces reflection and refraction at the temporal interface. We analytically determine the Fresnel-like coefficients for graphene plasmons at these boundaries, and validate our results by rigorous numerical simulations. Temporally controlled doping of two-dimensional materials such as graphene thus leads to a new mechanism for planar and compact plasmonic devices.

Graphene plasmonics is an ideal platform for temporal interfaces, because the plasmonic modes are widely tunable, show extreme confinement, and suffer relatively low losses [48, 49, 107]. In parallel studies, dynamical modulation of materials was shown to provide for a broad variety of unusual phenomena such as wavelength conversion [10, 15, 16, 18, 101, 106], optical isolation [23, 26] and topological effects [35, 37] (see Chapter 2). In this context, the behaviour of electromagnetic waves incident on 'time boundaries' is known for a long time [112], and often referred to as 'time reversal' [113]. These phenomena are very general, as works on surface plasmons [114] and a recent implementation of time reflection for water waves illustrate [115].
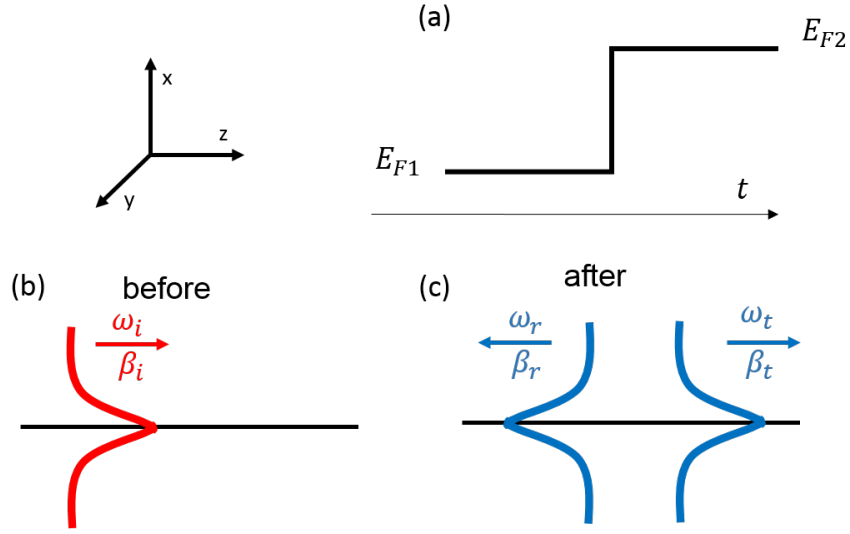
Figure 7.1: (a) Representation of a time step temporal boundary, where the Fermi level changes from E_{F1} to E_{F2}. Effect of a step time boundary on a propagating graphene plasmon: an incident plasmon (a) generates a reflected and transmitted plasmon (b) at a different frequency.

However, graphene plasmonic waveguides with time discontinuities were not yet addressed. Therefore, in this work we merge the fields of time boundaries with graphene plasmons, leading to an interesting way to reflect plasmons in two-dimensional compact circuits. These plasmons are highly suitable for this application, as the Fermi level can be modulated rapidly. Additionally, the nature of the plasmonic modes leads to straightforward expressions for the reflection and transmission properties at single or double discontinuities (so-called temporal slabs). Importantly, the phenomena and the analysis we report is general and valid for other types of guided modes.

We study plasmons propagating in a graphene sheet incident on two types of time boundaries: a single time step (Figure 7.1(a)), and a double time step (or slab). The phenomenon at a single time step is sketched in (Figure 7.1(b)-(c)): a forward propagating plasmonic mode (or pulse) is split into a backward (reflected) and forward (transmitted) wave after the temporal boundary (an abrupt change of the Fermi level E_{F}).

Here, the time boundaries are abrupt changes in the Fermi level E_{F} of the graphene sheet. We employ a the Drude-like model for the graphene conductivity introduced in Chapter 3 (Equation 3.3):

$$\sigma(\omega, E_{\text{F}}) = \frac{e^2 E_{\text{F}}}{\pi \hbar^2} \frac{-j}{\omega - j\tau_{\text{gra}}^{-1}}, \tag{7.1}$$

which is valid for $E_{\text{F}} \gg k_B T$, with $k_B T \approx 0.026$ eV. Since this conductivity only takes into account intraband transitions, we also require that $\hbar\omega \ll 2E_{\text{F}}$. Close to a time interface (so without long propagation distances), we can ignore the losses and set $\tau_{\text{gra}}^{-1} = 0$. However, the phenomena remain even with losses, as they do not depend on the mode amplitude.

The graphene plasmon dispersion in the nonretarded regime ($\beta \gg \omega/c$ with β the mode propagation constant) directly depends on E_{F} [9]:

$$\mathrm{Re}(\beta) = \frac{2\varepsilon_0\varepsilon_r\pi\hbar^2\omega^2}{e^2 E_{\mathrm{F}}},\tag{7.2}$$

where ε_r is the permittivity of the surrounding medium (we use $\varepsilon_r = 1$).

Graphene plasmons are TM modes. In this chapter, we consider plasmonic modes propagating along the z direction (see Figure 7.2 for the coordinate system). In this case, the transverse magnetic field component is H_y (see Figure 7.2 for all the graphene plasmon field profiles). We consider graphene plasmons in the non-retarded regime, where the mode profiles are extremely confined around the interface.
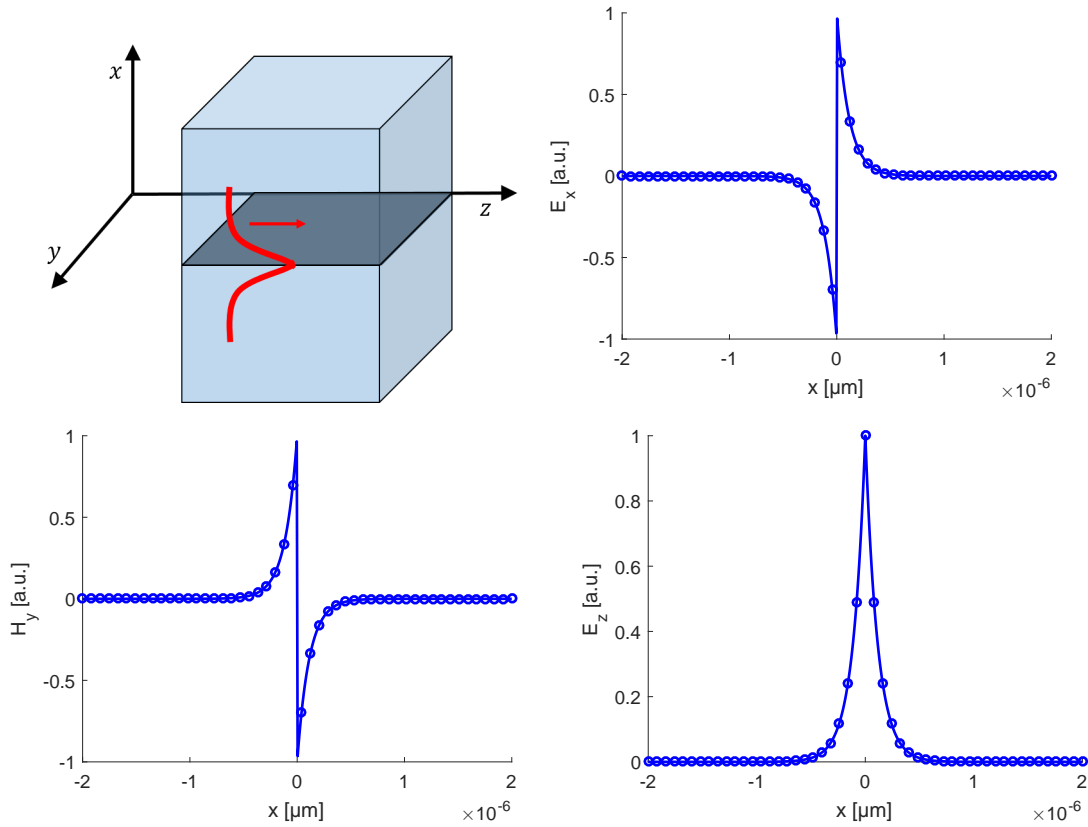
Figure 7.2: Top left: Graphene sheet and coordinate system used to describe graphene plasmonic modes. Top right: E_x, bottom left: H_y and bottom right: E_z. Solid lines are the exact modes (Equations 4.34 and 4.35) and circles represent the $\kappa \approx \beta$ approximation used in the non-retarded regime. For these field profiles, $E_{\mathrm{F}} = 0.6$ eV and the graphene plasmonic mode frequency is 30 THz (10 µm vacuum wavelength).

To describe graphene plasmons incident on a time boundary, different approximations have been used in the literature. In the first one [11], a quasi-static approach is used: **H** and its derivative are supposed continuous across the temporal boundary and the plasmon is entirely described by its transverse magnetic field. In another

quasi-static approach [116], **E** and **H** are supposed continuous at the time boundary. It is also possible to describe the temporal discontinuity in graphene by considering microscopic transport equations [117]. In this last approach, a jump in current due to the sudden removal of carriers is considered, leading to a discontinuity in **J**. This discontinuity occurs when carriers are removed (when E_{F} diminishes) so this approach was only developed for steps where the Fermi level suddenly decreases.

By combining the results from these 3 studies, one can get a better understanding of the application scope of each of these approximations. The quasi-static approaches using the continuity of **E** and J_z are suitable to describe upward steps ($E_{\mathrm{F1}} < E_{\mathrm{F2}}$ and $\gamma > 1$, where E_{F1} and E_{F2} are the Fermi levels before and after the temporal interface, respectively and $\gamma = \sqrt{E_{\mathrm{F2}}/E_{\mathrm{F1}}}$), while microscopic carrier removal considerations better describe downward steps ($E_{\mathrm{F1}} > E_{\mathrm{F2}}$ and $\gamma < 1$). Note that it is also possible to take into account the (typically small) amount of radiation and evanescent modes generated at the temporal interface by using more complex theories, however, the quasi-static models seem to offer a good approximation.

7.1　Upward steps

To describe upward steps, it is appropriate to employ the continuity of the field **E**. We also use a microscopic condition for the current J_z. After the shock, more free carriers are available to contribute to the current upon excitation by an electric field. However, the injected electrons do not have an initial speed and do not immediately form a current. This is why we employ the continuity condition $J_z(0^-) = J_z(0^+)$ for the current. This approach uses the methods of [117] and produces results similar to [116] where the continuity of E and H fields was used. Using continuity of **E** and J_z (and convention $e^{j\omega t}$):

$$E_{i,z}^{(\omega_i)} e_{i,z}^{(\omega_i)}(x) e^{-j\beta_i z} = E_{r,z}^{(\omega_r)} e_{r,z}^{(\omega_r)}(x) e^{-j\beta_r z} + E_{t,z}^{(\omega_t)} e_{t,z}^{(\omega_t)}(x) e^{-j\beta_t z}. \tag{7.3}$$

The continuity condition for $J_z = \sigma(\omega, E_{\mathrm{F}}) E_z$ with $\sigma(\omega, E_{\mathrm{F}})$ from Equation 7.1 at $t = 0$ reads:

$$-j \frac{e^2}{\pi \hbar^2} \frac{E_{\mathrm{F1}}}{\omega_i} E_{i,z}^{(\omega_i)} = -j \frac{e^2}{\pi \hbar^2} \left(\frac{E_{\mathrm{F2}}}{\omega_t} E_{t,z}^{(\omega_t)} + \frac{E_{\mathrm{F2}}}{\omega_r} E_{r,z}^{(\omega_r)} \right). \tag{7.4}$$

where $E_{\alpha,z}^{(\omega_\alpha)}$ is the mode amplitude, $e_{\alpha,z}^{(\omega_\alpha)}(x)$ the mode profile and β the propagation constant. Superscripts (ω_α) indicate the frequency, and subscripts $\alpha = i, r, t$ stand for incident, reflected or transmitted.

At a regular spatial interface (a change of index in space), the frequency is conserved across the spatial discontinuity. In contrast, for a temporal discontinuity the wavevector is conserved [118]: the z dependence in Equation 7.3 imposes that all the propagation constants β_α are equal:

$$\beta_i = \beta_t = \beta_r. \tag{7.5}$$

Since we change the Fermi level at the time interface, the frequency of the incident mode has to adapt to keep the wavevector unchanged (see Equation 7.2 and

Figure 7.3). Consequently, when an incident mode with a propagation constant β_i is incident on a time boundary (so when the medium suddenly changes), it produces a reflected and a transmitted ('refracted') mode with the same propagation constants (β_r, β_t), but at a different frequency. Using the dispersion (Equation 7.2) we link the frequencies to the Fermi levels around the temporal interface:

$$\gamma \omega_i = \omega_t = -\omega_r \tag{7.6}$$

where ω_i, ω_r and ω_t are the incident, reflected and transmitted frequencies, respectively. The minus sign accounts for backward propagation. $\gamma = \sqrt{E_{F2}/E_{F1}}$ is the shock amplitude, with E_{F1} (E_{F2}) the Fermi level before (after) the time boundary.
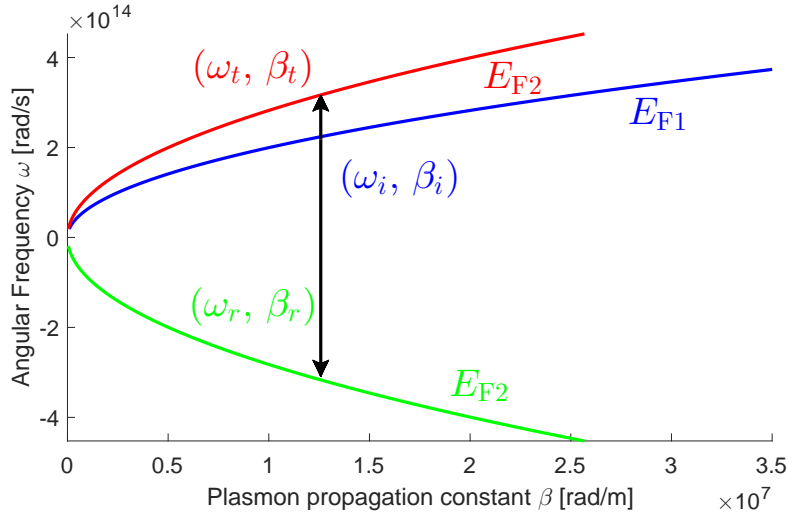
Figure 7.3: Time step and plasmon dispersion: the propagation constant is conserved while the frequency changes. For transmitted plasmons (red), the frequency remains positive since the plasmon is propagating in the same direction as the incident plasmon (blue). However, for the reflected plasmon the frequency becomes negative as its propagation direction is reversed. Here $E_{F2} > E_{F1}$.

Since β is conserved and we are in the nonretarded regime, the plasmonic mode profiles $e_{\alpha,z}^{(\omega_\alpha)}(x)$ are very similar on both sides of the temporal interface. This is why we cancel them out in the remainder (using the same normalization $e_{\alpha,z}^{(\omega_\alpha)}(x = 0^+) = 1$), which is a very useful approximation stemming from the extreme confinement of graphene plasmons. For lower-index modes this assumption should be reconsidered.

We define the Fresnel-like reflection and transmission coefficients as:

$$E_{r,z}^{(\omega_r)} = r_E E_{i,z}^{(\omega_i)}, \qquad E_{t,z}^{(\omega_t)} = t_E E_{i,z}^{(\omega_i)}. \tag{7.7}$$

The continuity of E_z at the temporal boundary ($t = 0$), along with Equation 7.7, imposes a first condition on r_E and t_E:

$$r_E + t_E = 1, \tag{7.8}$$

where we used the approximation that the field profiles are identical on both sides of the interface. This assumption is justified because we are in the non-retarded regime

and β is conserved. Using the continuity of J_z along with Equations 7.7 and 7.6, we find that

$$t_E - r_E = \frac{1}{\gamma}. \tag{7.9}$$

Equations 7.8 and 7.9 give the expressions for reflection and transmission for the E_z field at a temporal upward step boundary:

$$r_E = \frac{1 - \gamma}{2\gamma}, \quad t_E = \frac{1 + \gamma}{2\gamma}. \tag{7.10}$$

The transmittance and reflectance are then given by

$$R = \frac{(1 - \gamma)^2}{4\gamma^2}, \quad T = \frac{(1 + \gamma)^2}{4\gamma^2}. \tag{7.11}$$

The transmittance and reflectance of Equations 7.11 are represented in Figure 7.4 as a function of γ.
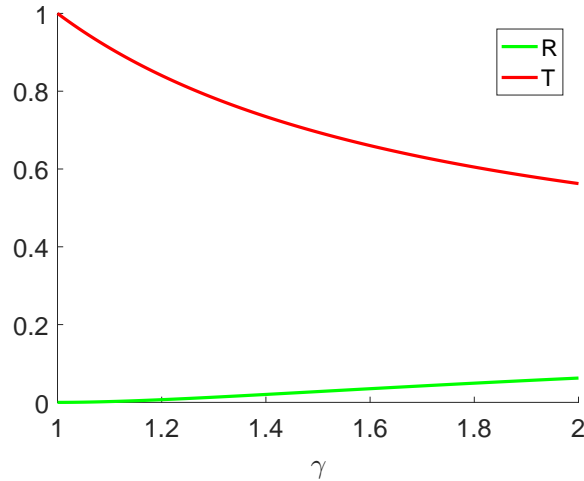
Figure 7.4: Transmittance and reflectance for upward step temporal interfaces (Equation 7.11).

The expressions of Equation 7.11 can be used at a step interface where the final Fermi level is higher than the initial Fermi level. For other types of step interfaces, other approximations are needed. Since this derivation only depends on the continuity of the fields, one can use the standard Finite Element Method (FEM) simulations in time domain to simulate upward steps. We run FEM simulations [95] to validate our results. We record (in time domain) the field profiles at two specific points in space, and then separate incident, reflected and transmitted pulses as shown in Figure 7.5.

Figure 7.6 shows simulated snapshots of a plasmon pulse at a temporal step, visualizing clearly the reflection and transmission effects. Notice the dispersion effects: modes with a lower β (so higher effective wavelength) propagate faster in graphene sheets (see leading edge of the 'transmitted' pulse, Figure 7.6(c)). In contrast, the reflected pulse is exactly like the incident pulse, showing the dispersion compensation [115]. Note that the simulations are spatially two-dimensional (x, z),
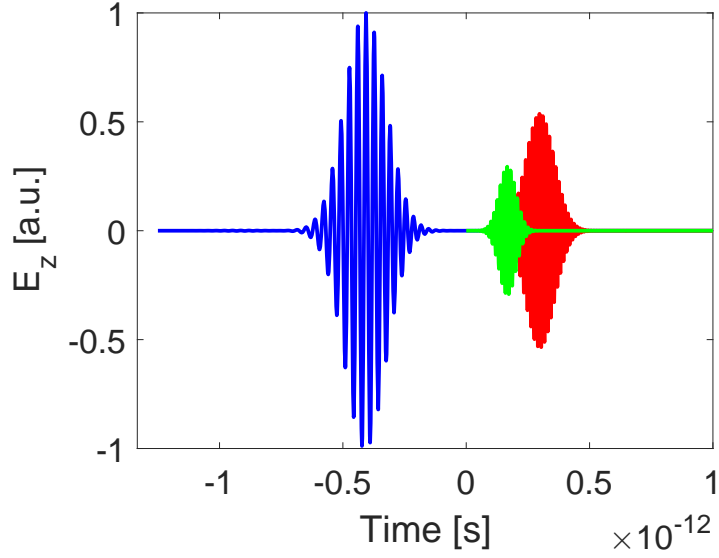
Figure 7.5: Incident (blue), reflected (green) and transmitted (red) pulses at an upward step time boundary. Here the starting Fermi level is $E_{\mathrm{F1}} = 0.1$ eV and the final Fermi level is $E_{\mathrm{F2}} = 0.6$ eV. The time step is located at $t = 0$. The incident and reflected pulses (blue and green) are recorded at one position and the transmitted pulse (red) is recorded at another position, further along the propagation direction.
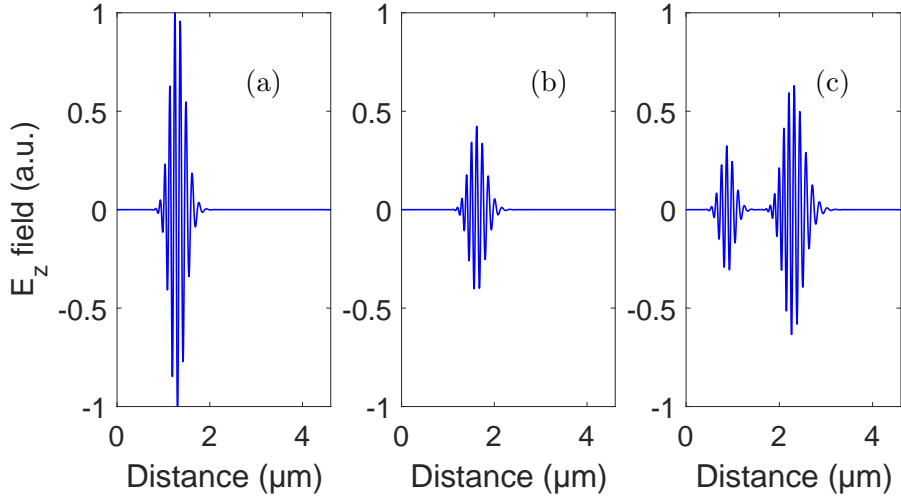
Figure 7.6: Simulations for a plasmonic pulse in an upward time step. The central incident frequency is $\omega_0 = 2\pi\ 30 \times 10^{12}$ rad/s, the plasmon period is $T_p = 2\pi/\omega_0$ and the shock happens at $t = 0$ s. The profile along the sheet is shown at time: (a) $-5T_p$, (b) 0 and (c) $5T_p$. We used $E_{\mathrm{F1}} = 0.1$ eV and $E_{\mathrm{F3}} = 0.6$ eV.

but we only show the field along the sheet, as radiation is negligible because of the large impedance mismatch (Figure 7.7).

Usually, at spatial interfaces, the reflectance (transmittance) is computed by taking the ratio of the reflected (transmitted) power over the incident power, and all these quantities are connected to the field amplitudes at the same frequency. Here
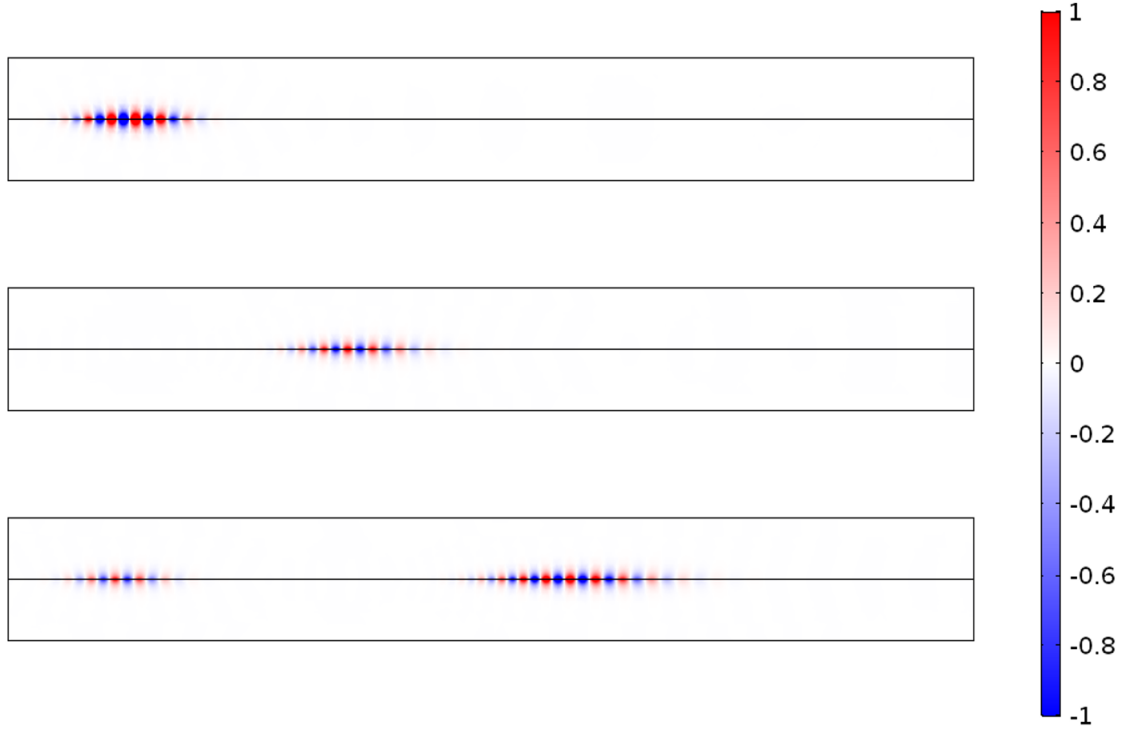
Figure 7.7: Snapshots the E_z field component in 2D simulations before, during, and after the shock (from top to bottom). As it is apparent from the 2D field profiles, radiation losses are negligible during the propagation, and at the temporal interface.

it is not the case: the transmitted and reflected pulses have a different frequency than the incident pulse (except when the initial and final Fermi levels are equal, as in a slab interface that returns to the original E_F). In the case where two pulses have a different frequency, one needs to compensate a spectral shift and a spectral compression or expansion. The electric field amplitudes of the wavepackets are defined as $E_{\alpha,y}^{(\omega_\alpha)}$. The transmission coefficients we computed theoretically are valid for monochromatic plasmons, which means that we need a relation that links the (non-monochromatic) simulation results to the theoretical coefficients.

If we consider an interval $\Delta\omega_1$ in the frequency spectrum, the electric mode amplitudes included in that interval will be converted to the interval $\Delta\omega_2$ after the temporal boundary. This analysis was reported in [117]. For the transmitted wavepacket at a step interface, we have:

$$E_{t,y}^{(\omega_t)}\Delta\omega_t = t_E E_{i,y}^{(\omega_i)}\Delta\omega_i \tag{7.12}$$

where t_E is the monochromatic transmission coefficient. This means that the following transformation must be applied to the simulation results:

$$t_E = f\frac{E_{t,y}^{(\omega_t)}}{E_{i,y}^{(\omega_i)}}, \quad f = \frac{d\omega_t(\omega_i)}{d\omega_i}. \tag{7.13}$$

where $E_{\alpha,y}^{(\omega_\alpha)}$ are the field amplitudes from FEM simulations. From Equation 7.6, $\omega_t = \gamma\omega_i$, so $f = \gamma$. Equation 7.13 allows us to compare our simulation results

to the theoretical predictions of Equation 7.10. Simulations of a step interface (Figure 7.8) from $E_{F1} = 0.1$ eV to $E_{F2} = 0.6$ eV ($\gamma = 2.45$) show that the reflected and transmitted plasmons indeed have a different frequency, in accordance with Equation 7.6. Simulations agree well with the theory (Equation 7.11): $R_{th} = 0.088$, $R_{FEM} = 0.088$, $T_{th} = 0.50$ and $T_{FEM} = 0.49$. Notice that for step time interfaces, the reflectance and transmittance are frequency independent. Moreover, R and T do not depend directly on the initial and final Fermi level, but only on the ratio of these Fermi levels (R and T are functions only of $\gamma = \sqrt{\frac{E_{F2}}{E_{F1}}}$).
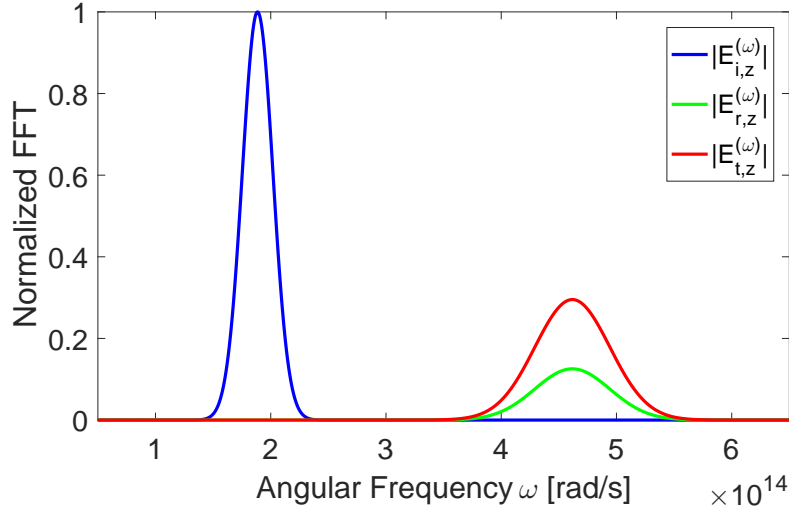
Figure 7.8: Simulated incident (blue), reflected (green) and transmitted (red) E_z fields in the frequency domain for an upward step temporal boundary. Here the starting Fermi level is 0.1 eV and the final Fermi level is 0.6 eV. Amplitudes are normalized to the maximum incident amplitude.

7.2 Downward steps

For steps where $E_{F1} > E_{F2}$ ($\gamma < 1$), one needs to consider different boundary conditions [117]. The sudden diminution of Fermi level corresponds to a reduction of the carrier density, while leaving the velocity of the remaining carriers unchanged. This implies that the current density J_z will be discontinuous at the time interface. The current density can be split into two contributions: $J_z(0^-) = J_{z1} + J_{z2}$, one of which vanishes after the shock $J_z(0^+) = J_{z2}$. These current densities are connected to the Fermi level before and after the temporal interface by the relations $J_z = \sigma(\omega, E_F)E_z$. The boundary condition for the current is

$$\frac{J_z(0^+)}{J_z(0^-)} = \frac{J_{z1}}{J_{z1} + J_{z2}} = \frac{E_{F2}}{E_{F1}}. \tag{7.14}$$

While the current is discontinuous at the temporal interface, the electric field component responsible for the surface current E_z must be continuous, as in Equation 7.3:

$$E_{i,z}^{(\omega_i)} e_{i,z}^{(\omega_i)}(x) e^{-j\beta_i z} = E_{r,z}^{(\omega_r)} e_{r,z}^{(\omega_r)}(x) e^{-j\beta_r z} + E_{t,z}^{(\omega_t)} e_{t,z}^{(\omega_t)}(x) e^{-j\beta_t z}. \tag{7.15}$$

Using the boundary condition for the current density of Equation 7.14 and the continuity of the E_z field (Equation 7.15), one finds the reflection and transmission coefficients at a step interface with $E_{F2} < E_{F1}$:

$$r_E = -\frac{(1-\gamma)}{2}, \quad t_E = \frac{(1+\gamma)}{2}, \tag{7.16}$$

and the transmittance and reflectance read

$$R = \frac{(1-\gamma)^2}{4}, \quad T = \frac{(1+\gamma)^2}{4}, \tag{7.17}$$

Figure 7.9 represents the reflectance and transmittance of Equation 7.17.
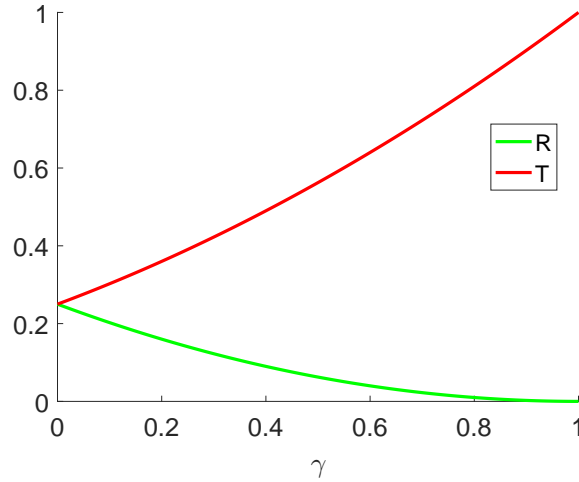
Figure 7.9: Transmittance and reflectance for downward step temporal interfaces (Equation 7.17).

The derivation in this section remains a quasi-static approach, but this time it is supplemented with a microscopic consideration of the carrier behaviour at the interface. However it was proven in [117] that the quasi-static limit is in accordance with a more complete theory, including evanescent modes and radiation.

Since we have studied the behaviour of graphene plasmons at upward and downward step interfaces, we can combine these two cases and plot the transmittance and reflectance of graphene plasmons as a function of γ in Figure 7.10. For both interfaces, the transmittance and reflectance have a limit of $1/4$: For the downward step interfaces, $T = R = 1/4$ for $\gamma = 0$, and for the upward step interfaces, $T = R = 1/4$ for $\gamma \to \infty$. For $\gamma = 0$, E_F is continuous with $T = 1$ and $R = 0$, as there is no shock.

For both up and down modulations, no energy is injected into the system. The losses from the shock can be modeled by $1 - T - R$, which becomes $1/2$ in the limit of strong shocks (γ very large or very small).
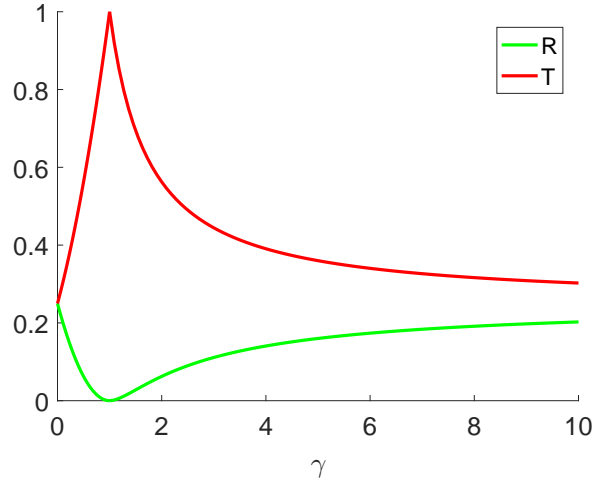
Figure 7.10: Transmittance and reflectance for downward steps ($\gamma < 1$, Equation 7.11) and upward steps ($\gamma > 1$, Equation 7.17).

7.3 Temporal slabs

A slab consists of two successive temporal steps. We will consider one case where the starting and final Fermi levels are equal, and one case where they are different. A temporal slab is represented in Figure 7.11. The graphene Fermi level will go from E_{F1} to E_{F2} and back to E_{F1}. The two temporal steps are separated by the time τ. It is interesting to note that in the case of a spatial slab, interferences occur because of a phase βl (with l the slab length), whereas here the phase is described $\gamma_{12}\omega\tau$ (with $\gamma_{12} = \sqrt{E_{F2}/E_{F1}}$, τ the slab duration, and $\gamma_{12}\omega$ the frequency 'inside' the slab).
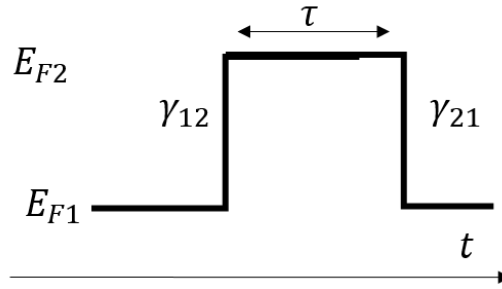
Figure 7.11: Representation of a slab temporal boundary. The initial and final Fermi level are equal, which implies that $\gamma_{12} = \gamma_{21}^{-1}$. The two step boundaries are separated by the slab duration τ.

This type of temporal interface is composed of an upward step and a downward step. To compute the reflectance and transmittance of a temporal slab, one needs to combine the reflection and transmission coefficients for the two different types of steps (Equations 7.16 and 7.10):

$$T = \left| r_{12}r_{21}e^{-j\omega_2\tau} + t_{12}t_{21}e^{j\omega_2\tau} \right|^2 \tag{7.18}$$
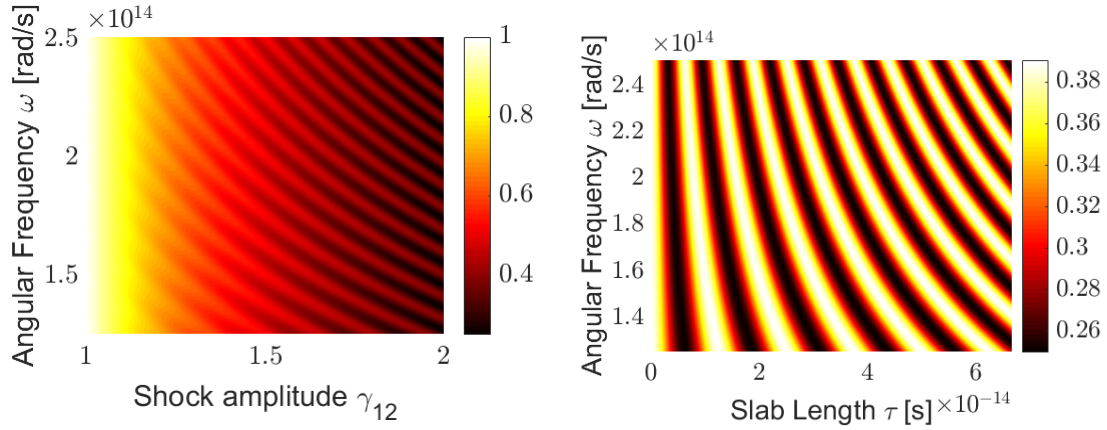
Figure 7.12: Analytical transmittance T of Equation 7.19 as a function of ω and (left) γ_{12} ($\tau = 1.67 \times 10^{-13}$ s), or (right) τ ($\gamma_{12} = 2$).

where $\omega_2 = \gamma_{12}\omega_1$ is the frequency inside the slab, the transmission and reflection coefficients r_{12} and t_{12} are the upward step coefficients from Equation 7.10 while r_{21} and t_{21} are the downward step coefficients from Equation 7.16. Note that unlike in a spatial slab, there cannot be an interaction with the same interface multiple times because of causality. This is why there are only 4 terms in Equation 7.18. Equation 7.18 simplifies to

$$T = \gamma_{21}^2 \left[1 + \frac{1}{4} \left(\gamma_{12} - \gamma_{21} \right)^2 \cos^2 \gamma_{12}\tau \right] . \tag{7.19}$$

Similarly, the reflectance is computed as

$$R = \left| r_{12}t_{21}e^{-j\omega_2\tau} + t_{12}r_{21}e^{j\omega_2\tau} \right|^2 \tag{7.20}$$

and simplifies to

$$R = \frac{\gamma_{21}^2}{4} \left(\gamma_{12} - \gamma_{21} \right)^2 \sin^2 \gamma_{12}\omega\tau \tag{7.21}$$

The reflectance and transmittance of a temporal step only depend on the (square root of the) ratio of the initial and final Fermi levels γ_{12}. In contrast, the slab characteristics depend on the length τ, the amplitude γ_{12} and the incident frequency ω. These parameters allow for a large tunability, see Figures 7.12(a,b). A larger shock (γ_{12} more distant from 1) leads to an overall lower transmittance, but interferences give oscillations (Figure 7.12(a)). For the same reason the slab length allows to tune the reflectance and transmittance (Figure 7.12(b)).

This type of slab interface is a special case: the Fermi level of the graphene sheet is the same before and after the temporal boundary. One can also study another type of temporal slab where the initial and final Fermi levels are different, for example, an interface composed of two upward steps (Figure 7.13). The reflectance and transmittance in this case are given by:

$$T = \frac{1}{4\gamma_{13}^4} \left[\left(\gamma_{12} + \gamma_{23} \right)^2 + \left(1 + \gamma_{13}^2 - \gamma_{12}^2 - \gamma_{23}^2 \right) \cos^2(\gamma_{12}\omega\tau) \right] , \tag{7.22}$$

$$R = \frac{1}{4\gamma_{13}^4} \left[\left(\gamma_{12} - \gamma_{23} \right)^2 + \left(1 + \gamma_{13}^2 - \gamma_{12}^2 - \gamma_{23}^2 \right) \cos^2(\gamma_{12}\omega\tau) \right] \tag{7.23}$$
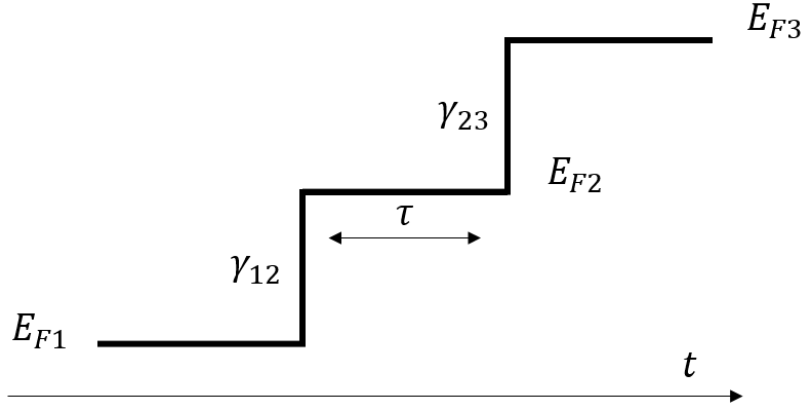
Figure 7.13: Representation of a temporal boundary formed by two upward steps. Here the initial and final Fermi levels are different, and it is necessary to use Equation 7.13 to interpret simulation results in terms of monochromatic transmission and reflection coefficients.

were $\gamma_{13} = \sqrt{E_{F3}/E_{F1}} = \gamma_{12}\gamma_{23}$. We compare these results with numerical simulations in Figure 7.14 for different slab durations τ. The simulation results agree well with the analytical calculations and show that it is possible to control the in-plane scattering of graphene plasmons with temporal boundaries.
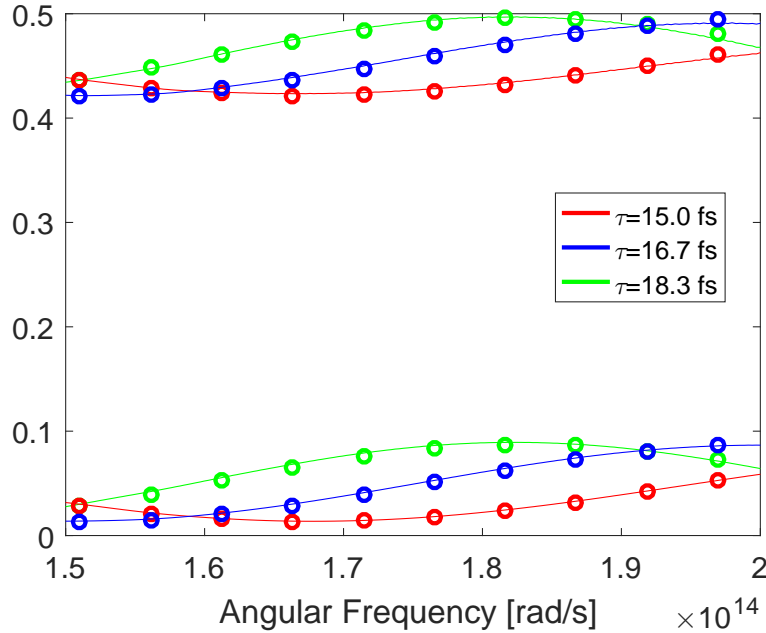
Figure 7.14: Transmittance and reflectance of a time interface consisting of two upward steps for different slab durations τ. Solid lines: Theoretical prediction of Equations 7.22 and 7.23. Dots: FEM simulation results. In all these cases, $T > R$. The successive Fermi levels are $E_{F1} = 0.1$ eV, $E_{F2} = 0.35$ eV and $E_{F3} = 0.6$ eV.

7.4   Conclusion

In these effects the Fermi level variation occurs within a time comparable to the graphene plasmon period, which is experimentally challenging, and the models presented in this chapter suppose that the density of carriers is a step function. This constitutes a limit to the model, but a variation of graphene on a scale of 10 fs was demonstrated [57, 59, 60], so our abrupt model still closely resembles more realistic transitions. One could use lower frequency graphene plasmons to lift this limitation. One may also use a longer slab duration, leading to more oscillations in the transmittance. In the end, if the transmittance oscillates many times in the pulse bandwidth, it is expected that the system will experience an average (increased) transmittance for the whole pulse.

In order to achieve ultrafast switching, one can consider a direct external pump, to excite carriers on a timescale faster than the electron relaxation time (on the order of 10^{-12} s). Alternatively, one could exploit nonlinear Kerr-type effects, or switch to other two-dimensional materials [119].

Using the highly tunable framework of graphene, we described the behaviour of plasmons at temporal interfaces. Our analytical approach leads to very simple relations for reflectance and transmittance, which are in good agreement with rigorous simulations. This process is highly tunable via the duration, shock height and plasmon frequency. Possible applications include frequency selective filters, amplifiers and modulators. The phenomenon is very general, and our analysis can be adjusted for other guided mode resonances, plasmonic or not.

8

Selective frequency conversion via Floquet modes

In this chapter we present a mechanism to achieve efficient and selective frequency conversion using a system of two time-modulated cavities. This setup allows to fine-tune the conversion process by controlling important parameters such as the inter-cavity coupling and the external excitation frequency. Both symmetric and asymmetric (up- or down-conversion) outputs can be targeted at will. We describe the processes extensively, with for example a leading role for the dynamic modes of the coupled system, the Floquet modes.

Ginis et al. examined the possibility to produce a frequency comb by modulating the conductivity of a planar graphene sheet [106]. However, the efficiency of this process is hampered because of the large change in conductivity needed to obtain a significant modulation in the transmission. In Chapter 6 we presented a way to overcome this limitation using a graphene ribbon array [10], with interaction between a single time-modulated resonance and the incident light. A plasmonic resonance in such an array allows to produce combs with a greatly enhanced efficiency, and with a fairly good control [120]. Typically, frequency comb generation is implemented by four-wave mixing [121, 122], with effective implementation in micro-ring resonators [123] or nanophotonic wire waveguides for example [124].

In this chapter we extend the system to two time-modulated coupled resonances, instead of a single one. Importantly, this system turns out to be effective for *selective* frequency conversion, so that instead of an extensive frequency comb, we are targeting conversion towards specific frequencies, by exploiting the interference processes in play. The mechanism and our description are quite general, so that in practice various dielectric or plasmonic implementations, such as graphene ribbons with different widths, can be considered.

We mainly optimize the asymmetric conversion towards a single sideband, and the symmetric conversion towards two equally spaced sidebands. We consider the specific degenerate case first (when the two cavity resonance frequencies are equal), and then compare with the more general non-degenerate case. We elucidate the crucial role of the intermodal coupling constant and the source frequency, using various semi-analytical approaches. It is very interesting that the so-called 'Floquet modes' play an important role in these processes. We determine the band structure of these modes of the dynamic system, and observe for example that the conversion efficiency is greatly enhanced in the neighborhood of Floquet band anti-crossings.

We study the system using the well-established Coupled Mode Theory (CMT) equations for coupled cavities (see Chapter 5). We employ this method with time-dependent resonance frequencies in Section 8.1. We show that this system supports Floquet modes in Section 8.2, and provide a method to obtain their frequencies. We then discuss how to achieve selective frequency conversion in Section 8.3, with an extensive evaluation of the process efficiency. In addition, Section 8.4 explains how a simple three-frequency analysis can determine the system parameters to achieve the desired conversion. Finally, in Section 8.5 we derive an analytic approximation of the band structure of the Floquet modes using a perturbation analysis.

8.1   Setup and Coupled Mode Theory

We study a system of two coupled resonances, which can be created for example by two nearby cavities. Here, the resonance frequency of one of the cavities will be time-modulated, leading to the generation of new frequency components. A sketch of the system is depicted in Figure 8.1(a). A possible way to physically implement this setup could consist of two graphene ribbon arrays with different widths [65, 79] (Figure 8.1(b)), as the conductivity can be dynamically modulated [51] in graphene.

To limit the number of parameters, we consider direct injection (amplitude $s(t)$) into one of the modes, which does not radiate (the so-called dark mode, amplitude $a(t)$), whereas the other mode (the bright one, $b(t)$) radiates, providing the output. We describe this two-cavity setup by a system of coupled equations with CMT [125]:

$$\frac{da(t)}{dt} = j\omega_1 a(t) + j\kappa b(t) + s(t) \tag{8.1}$$

$$\frac{db(t)}{dt} = j\omega_2(t)b(t) + j\kappa a(t) - \gamma b(t) \tag{8.2}$$

where $a(t)$ and $b(t)$ are respectively the dark and bright mode amplitudes, γ is the outcoupling coefficient, κ is the coupling coefficient between the two cavities, $\omega_{1,2}$ are the (potentially time modulated) resonance frequencies, and $s(t)$ is the input,
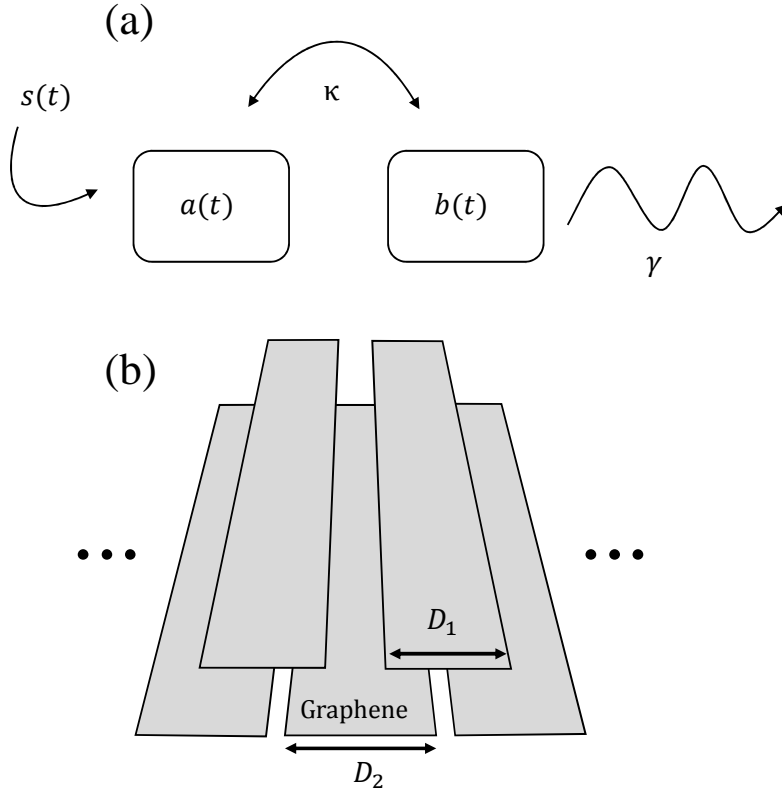
Figure 8.1: (a) Representation of the system of coupled resonances. (b) Possible implementation using two coupled arrays of graphene ribbons. Each cavity corresponds to a plasmonic resonance in the graphene array, where different ribbon widths (D_1 and D_2) provide different resonance frequencies. The ribbons are repeated in the horizontal direction creating two vertically offset gratings.

for which we use a nearly monochromatic gaussian pulse (with central frequency ω_0).

Here the source $s(t)$ can be considered as a dipolar emitter coupling to the field of the dark mode $a(t)$, in the weak-coupling limit. For systems with one or more input waveguides the model can be extended to take external interferences with reflection and transmission into account.

In this model the κ values are real so energy conservation is ensured. In order to get realistic parameter values for the CMT model, we ran Finite-Element Method simulations of a graphene ribbon array [10] (Chapter 6). This allowed us to connect the CMT parameters to the physical properties of graphene arrays. We determined that the plasmon absorption rate in a typical setting can be one order of magnitude smaller than the plasmon outcoupling time, so for simplicity we do not consider these losses in this model.

Usually the resonant frequencies are constants, but here for time modulation they become functions of time, and we will consider a periodic modulation. In this chapter we focus on the case where only the bright mode resonance is modulated:

$$\omega_2(t) = \omega_2 + \delta \sin\left(\Omega t\right) \tag{8.3}$$

with ω_2 the 'static' resonance frequency, δ the modulation amplitude and Ω the modulation frequency. The modulation amplitudes δ we consider here are of the same order of magnitude as Ω. This modulation amplitude can be achieved with modest E_F changes [10], because resonance frequencies in graphene ribbons strongly depend on E_F and because we consider modulation frequencies such that $\omega_{1,2} \gg \Omega$. The phenomena are similar if we modulate the other mode, or if we modulate both modes. Other modulation functions [113], such as step-functions or shocks [11, 126], could also be considered in future work.

This work is distinct from the effects in most modulators: Typically, the modulation frequency is slow and the modulation amplitude is not too high compared to the outcoupling rate [120]. In those cases (the adiabatic limit), the approximation of a time-dependent transmission, neglecting the interaction with the cavity modulation, is often used. However, here the time-dependence is non-trivial, and the light stays trapped in the cavity for a few modulation cycles. In this high-frequency limit, new frequencies are generated and the parameters governing this frequency conversion are investigated in detail further on.

In Chapter 6, with a single-cavity system that is time modulated, it was observed that one obtains a wide frequency comb, with components separated by the modulation frequency Ω. While that setup is useful for generating a wide range of new frequencies, it is more difficult to obtain an efficient conversion to a specific frequency. With the two-cavity setup described here, it becomes possible to obtain more focused features, such as selective frequency conversion.

8.2   Floquet modes

In this section we introduce Floquet modes, as they play an important role to understand and optimize the frequency conversion process further on. Floquet modes are the time analogues of Bloch modes in space, with a time-periodic modulation of the index, instead of a space-periodic index distribution for Bloch modes. In our setup the optical potential (via the resonance frequency $\omega_2(t)$) is periodic in time so the Floquet modes can be defined.

The static non-driven coupled system (i.e. constant frequencies $\omega_{1,2}$) has two modes with frequencies $\omega_\pm = \frac{\omega_1+\omega_2}{2} \pm \frac{1}{2}\sqrt{(\omega_1 - \omega_2)^2 + 4\kappa^2}$. In the degenerate case where $\omega_1 = \omega_2 = \omega_{1,2}$, the two mode frequencies take the simple form $\omega_\pm = \omega_{1,2} \pm \kappa$ (see red dashed lines in Figure 8.2).

With the introduction of time modulation, these frequencies are adjusted, and have multiple Floquet mode branches with frequency difference Ω (see blue solid lines in Figure 8.2). Interestingly, when these branches meet as a function of κ they can lead to anti-crossings (see around $\kappa = \Omega/2$ in Figure 8.2). This is a different effect than bandgaps that appear for propagative Floquet modes [127]. Here we study two coupled localized resonances so no true bandgap is opened.

One way to compute the Floquet mode frequencies is to write Equations 8.1 and 8.2 (without the source term) in matrix form [94]:

$$-j\frac{dF(t)}{dt} = H(t)F(t) \tag{8.4}$$
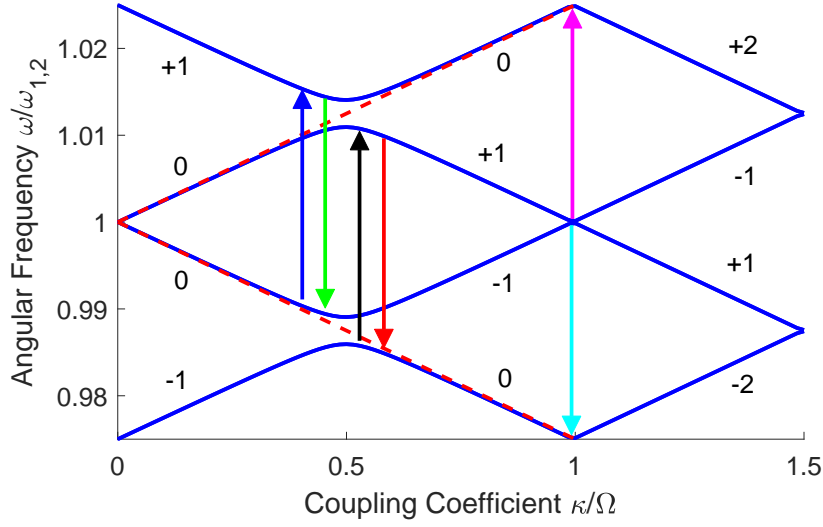
Figure 8.2: Blue lines: Floquet modes of the system for the degenerate case, where $\omega_{1,2} = 2\pi \times 10^{13}$ rad/s, $\Omega = 2\pi \times 2.5 \times 10^{11}$ rad/s and $\delta = \Omega/2$. Dashed red lines: static resonance frequencies for the degenerate case ($\omega_{\pm} = \omega_{1,2} \pm \kappa$). The four arrows near $\kappa = \Omega/2$ represent the transitions of interest that we study in Section 8.3.1 while the two arrows near $\kappa = \Omega$ represent the transitions that we study in Section 8.3.2. An anti-crossing appears at $\kappa = \Omega/2$ where the static modes intersect.

where $F(t)$ is a matrix of eigenvectors and $H(t)$ is the time-modulated Hamiltonian. Floquet's theorem insures that a solution exists in the form

$$F(t) = \Phi(t)e^{jQt} \tag{8.5}$$

where $\Phi(t)$ is a matrix of periodic functions and Q is a constant diagonal matrix containing the Floquet eigenvalues (compare with the typical Bloch mode form). Since $\Phi(t)$ and $H(t)$ are matrices of periodic functions, it is convenient to expand them in Fourier series:

$$F_{ab}(t) = \sum_n F_{ab}^n e^{jn\Omega t} e^{jq_b t} \tag{8.6}$$

$$H_{ab}(t) = \sum_n H_{ab}^n e^{jn\Omega t} \tag{8.7}$$

where q_b are the diagonal elements of Q, $\Omega = 2\pi/T$, and T is the period of $\Phi(t)$ (see Equation 8.3). The indices a and b denote a cavity mode, while index n (and also m in the following equations) represents Fourier components. By injecting these forms into Equation 8.4, one obtains an eigenvalue equation for the (column) eigenvectors $F_{:b}$ (the Floquet modes) and eigenvalues q_b

$$H_F F_{:b} = Q F_{:b} \tag{8.8}$$

with H_F called the Floquet Hamiltonian defined by:

$$\langle an|H_F|bm\rangle = H_{ab}^{n-m} + n\Omega\delta_{ab}\delta_{nm}. \tag{8.9}$$

This infinite Floquet Hamiltonian for our case (only $\omega_2(t)$ modulated as in Equation 8.3) has the following form:

$H_F =$

$$
\begin{bmatrix}
\ddots & \cdots & \cdots & \cdots & \cdots & \cdots & \cdots & \iddots \\
\vdots & \omega_1 - \Omega & \kappa & 0 & 0 & 0 & 0 & \vdots \\
\vdots & \kappa & \omega_2 - \Omega & 0 & \delta/2 & 0 & 0 & \vdots \\
\vdots & 0 & 0 & \omega_1 & \kappa & 0 & 0 & \vdots \\
\vdots & 0 & \delta/2 & \kappa & \omega_2 & 0 & \delta/2 & \vdots \\
\vdots & 0 & 0 & 0 & 0 & \omega_1 + \Omega & \kappa & \vdots \\
\vdots & 0 & 0 & 0 & \delta/2 & \kappa & \omega_2 + \Omega & \vdots \\
\iddots & \cdots & \cdots & \cdots & \cdots & \cdots & \cdots & \ddots
\end{bmatrix}
\tag{8.10}
$$

This time-independent matrix is ordered in a special way: the indices go through a and b before each change in n and m. In that representation, it is clear that the coupling coefficient κ is responsible for the coupling between Floquet modes 'inside' a Fourier component, while the temporal modulation (represented by δ) couples Floquet modes across Fourier components. In other words the coupling between Floquet modes takes the form of a 'cascaded' nearest neighbor transition. For example this means that in order to couple from one Floquet mode to another mode separated by 3Ω, three successive transitions need to occur. This explains why frequency comb components typically decay as they are further away from the source frequency (see example in Figure 8.3).

In order to get an estimate of the Floquet eigenvalues, one truncates the time-independent matrix H_F and numerically computes its eigenvalues. An example is shown in Figure 8.2, where the solid blue lines represent four Floquet mode frequencies in the degenerate case ($\omega_1 = \omega_2$), as a function of the coupling constant κ. As mentioned, the red dashed lines represent the static eigenfrequencies of the degenerate system ($\omega_\pm = \omega_1 \pm \kappa$). The Floquet frequencies form a band structure and can exhibit anti-crossings, leading to bandgap-like features. The modulation amplitude δ is the parameter responsible for the anti-crossing: a larger δ yields a wider anti-crossing.

8.3   Selective frequency conversion

In this central section we examine the structure of the generated frequency combs, and discuss the relevant shaping parameters for interesting cases. Figure 8.3 shows a typical comb produced by the coupled cavities, with the frequency components separated by the modulation frequency Ω. Furthermore, the sideband amplitudes decrease rapidly further away from the excitation frequency ω_0, as the conversion is a cascade process (see e.g. the infinite Floquet matrix of Equation 8.10). In this chapter we mainly focus on the left and right immediate sidebands ($\omega_0 \pm \Omega$), as they

are expected to yield a better conversion efficiency, but some of the results can be generalized to other frequency components as well.
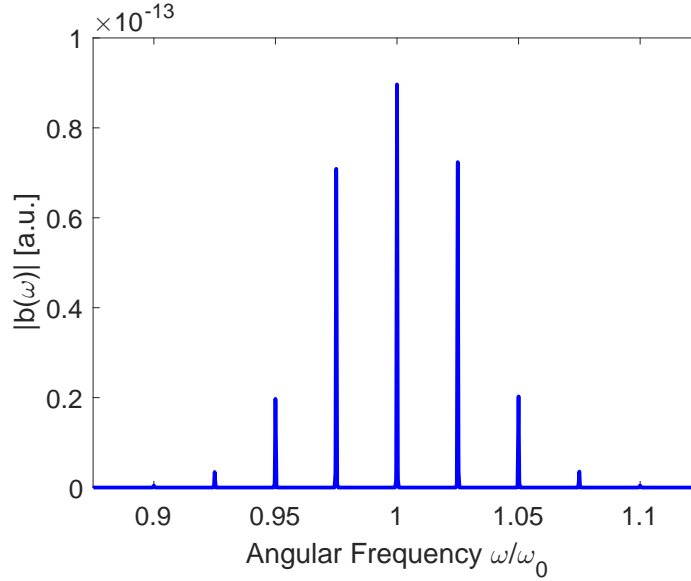
Figure 8.3: Typical frequency comb produced by a time-modulated two-cavity setup. Here $\omega_1 = \omega_2$ and only the bright cavity is modulated. The parameters are such that no particular enhancement is achieved ($\omega_0 = \omega_{1,2} = 2\pi \times 10^{12}$ rad/s, $\Omega = \omega_0/40$, $\kappa = \Omega/2$, $\delta = \Omega/4$ and $\gamma = 2 \times 10^{11}$ rad/s).

The reason why the Floquet modes are so useful here is that the conversion efficiency is much more efficient when we excite a Floquet mode. This holds both for the excitation frequency ω_0, and for the 'destination' frequencies $\omega_0 \pm \Omega$ (one statement leads to the other as the modes are spaced Ω apart). This means that if we excite a combination of κ and ω_0 values directly on a Floquet branch (so a point on the blue lines in Figure 8.2), we are bound to have strong interactions between the components.

This intuition leads to two important cases, which we discuss in detail in the following subsections. The first case corresponds with a κ value around the first anti-crossing ($\kappa \approx \Omega/2$) and when ω_0 is equal to a Floquet mode frequency. This leads to 'transitions' indicated by the four arrows at $\kappa \approx \Omega/2$ in Figure 8.2 (from ω_0 to $\omega_0 \pm \Omega$). Each of these arrows corresponds to a frequency conversion from a Floquet mode to another Floquet mode. We call this case (around $\kappa \approx \Omega/2$) the 'asymmetric conversion' case, as it will be efficient in one direction only, leading to a single large sideband.

The second case (or regime) corresponds with a κ value around the first mode crossing ($\kappa \approx \Omega$), and when ω_0 is equal to a Floquet mode frequency. The transitions of interest here are represented by the two arrows in Figure 8.2 around $\kappa \approx \Omega$. This is the 'symmetric conversion' case, as both sidebands (at $\omega_0 \pm \Omega$) will be generated efficiently.

Furthermore, one expects that the coupling of the source to Floquet modes close to the static modes of the system will be more efficient. This is because the other Floquet harmonics are introduced in the system only via the time perturbation,

whereas the two 0-order Floquet modes are connected to the static modes of the system (see numbers in Figure 8.2 for the mode orders). In the end we typically observe a lower conversion efficiency for transitions that originate from (or transition to) higher order Floquet modes.

8.3.1   Asymmetric conversion

The first interesting case is the asymmetric one, as in extreme cases it leads to a highly selective conversion, where the excitation is efficiently converted towards a single new frequency. Interestingly, we will show that this is most effective at the first bandgap condition (where $\kappa = \Omega/2$). For simplicity we here discuss the degenerate case where $\omega_1 = \omega_2$.

In order to characterize the conversion efficiency, we calculate two figures of merit (FOMs) $\Gamma_\pm = \frac{\gamma |b(\omega_0 \pm \Omega)|}{|s(\omega_0)|}$, which indicate the fraction of excitation converted to the two direct sidebands. Here $b(\omega)$ and $s(\omega)$ are the Fourier components of the bright mode amplitude $b(t)$ and gaussian source $s(t)$, respectively. This FOM is the ratio of mode amplitudes converted from the source to a different frequency component. This fraction is useful to establish the conversion efficiency inside the coupled mode system.

Figure 8.4 shows the FOMs $\Gamma_\pm$ as a function of ω_0 at the anti-crossing ($\kappa = \Omega/2$). In detail, this means we monitor $\Gamma_\pm$ along a vertical line ($\kappa = \Omega/2$) in Figure 8.2. The increased efficiency for four ω_0 values (four peaks for both Γ_+ and Γ_-) is due to the presence of the Floquet modes: the excitation ω_0 sweep cuts through four Floquet branches in this range.

In addition, there is a strong dependence concerning the direction of the transition in Figure 8.4: Γ_+ is large for the two low-frequency peaks, and small for the two high-frequency peaks (and vice versa for Γ_-). This can be understood from Figure 8.2: The two strong up-conversion peaks (Γ_+ is up-conversion) correspond to the blue and black arrows, leading to transitions with 0-order modes involved. The two weak up-conversion peaks at high frequencies actually mean transitions that go upwards beyond the data in Figure 8.4, so concerning higher order modes as destination. Similarly, the two large down-conversion peaks (Γ_-, so red in Figure 8.4) correspond to the green and red arrows in Figure 8.2. Clearly, the coupling of the source to higher order modes is less efficient since these modes only exist because of the perturbation introduced by the time dependence.

The frequency conversion is indeed highly asymmetric and selective in this case, see the example in Figure 8.5, with the comb for parameters corresponding to the second peak in Figure 8.4 ($\omega_0 = 0.9891\ \omega_{1,2}$). The light is efficiently converted to the upper frequency sideband, with few energy in the lower sideband.

Thus, Floquet modes play an important role in the conversion process: when the incident frequency ω_0 matches a Floquet mode frequency, the conversion process is enhanced. Now we describe ways of improving the conversion efficiency when the incident frequency is on a Floquet branch. In this way, we try to exploit the Floquet mode band structure.

To find where the conversion process is most efficient, we monitor the FOMs for a few transitions of interest (see arrows in Figure 8.2). In detail, we move the
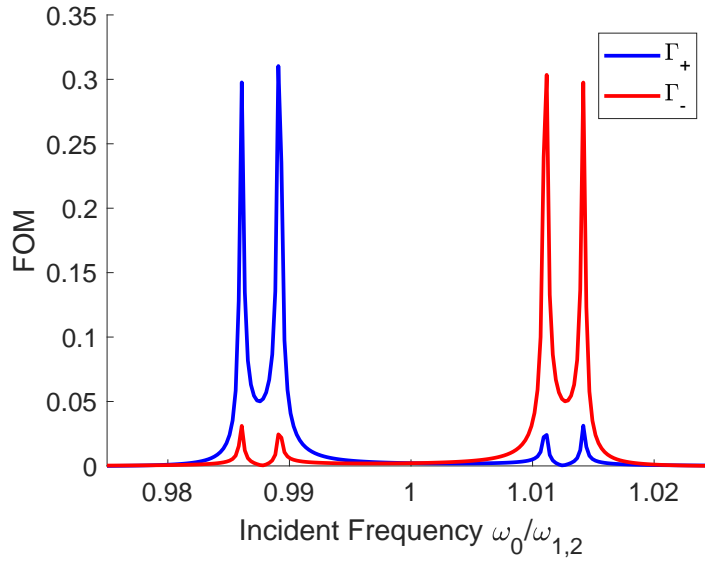
Figure 8.4: Figures of merit $\Gamma_{\pm}$ as a function of the incident frequency ω_0. The frequency conversion is asymmetric at the anti-crossing (when $\kappa = \Omega/2$). When ω_0 is equal to a Floquet mode frequency, the conversion efficiency is enhanced. The difference in conversion efficiency depends on the initial and final mode order: the coupling between source and Floquet modes is better for lower order modes.
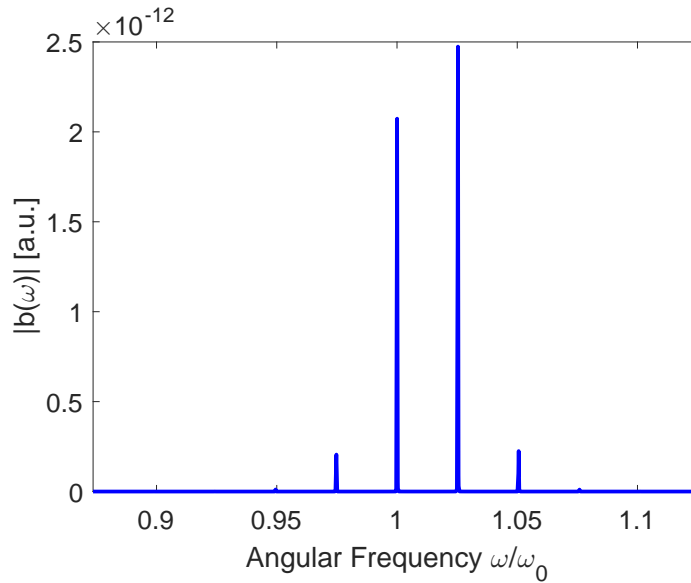
Figure 8.5: Comb produced by a set of parameters corresponding to the second peak of Figure 8.4 ($\omega_0 = 0.9890\ \omega_{1,2}$). The conversion to the upper sideband ($\omega_0 + \Omega$) is more efficient than the conversion to the lower sideband ($\omega_0 - \Omega$) and as a result the comb is asymmetric.

incident frequency *along* a Floquet band by changing the coupling coefficient κ, and we plot the corresponding FOMs in Fig 8.6. This means that we follow the blue lines in Figure 8.2 (mainly around $\kappa = \Omega/2$), so for Figure 8.6 the incident frequency is always equal to a Floquet frequency. The main trend is that all four

transitions have a maximum around $\kappa = \Omega/2$: clearly the conversion is most efficient when one operates at the edge of the anti-crossing. Furthermore, one observes that the blue and red transitions are always somewhat stronger than the green and black transitions. This reflects their different mode order combinations (see the corresponding arrows in Figure 8.2): the blue/red transitions start from modes closest to the center frequency ($\omega_{1,2}$), and arrive at modes away from the center. For the green/black transitions this is inverted, leading to a less efficient process.
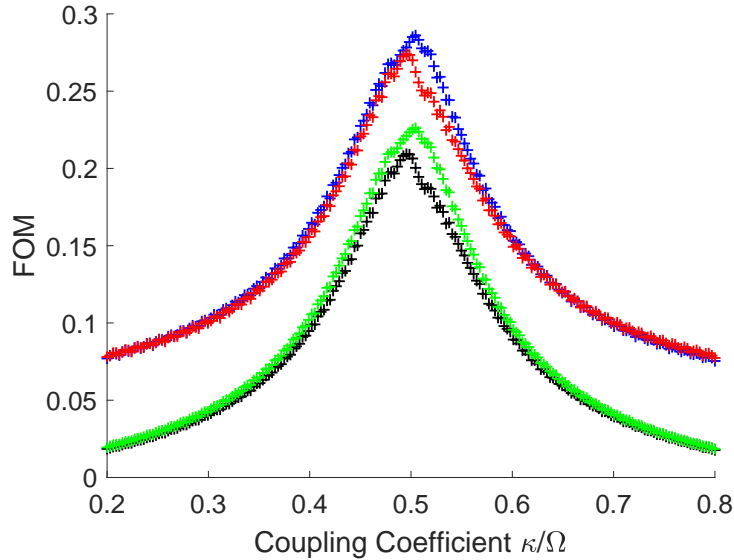
Figure 8.6: Figures of merit $\Gamma_\pm$ for the four transitions highlighted in Figure 8.2 around the bandgap. The conversion efficiency is greater when the incident mode is a 0-order mode and at the band edge (for $\kappa = \Omega/2$).

8.3.2 Symmetric conversion

Another useful regime in the two-cavity system leads to a 'symmetric' frequency conversion, where the two first sidebands are favored and have a similar amplitude. This type of frequency conversion occurs efficiently at the first band crossing (around $\kappa \approx \Omega$), see the arrows in Figure 8.2.

The up- and down-conversion FOMs ($\Gamma_\pm$) are shown in Figure 8.7, so we follow a vertical line in Figure 8.2, around the central frequency. When ω_0 is equal to the Floquet mode frequency (in this degenerate case the modes cross), the conversion efficiency is strongly enhanced (a strong peak for both FOMs). The conversion is quite symmetric, as $\Gamma_+ \approx \Gamma_-$. Due to the perturbation introduced by the time modulation, the bands bend and do not cross exactly at $\kappa = \Omega$, but slightly before. The perturbation analysis of Section 8.5 gives a good estimate of the correct κ value that we use in Figure 8.7 ($\kappa = 0.9948\,\Omega$).

Figure 8.8 shows a comb produced by the parameters corresponding to the central peak of Figure 8.7. Conversion to both sidebands is enhanced, as the two sidebands correspond to Floquet mode frequencies (see band diagram of Figure 8.2 at $\kappa \approx \Omega$).
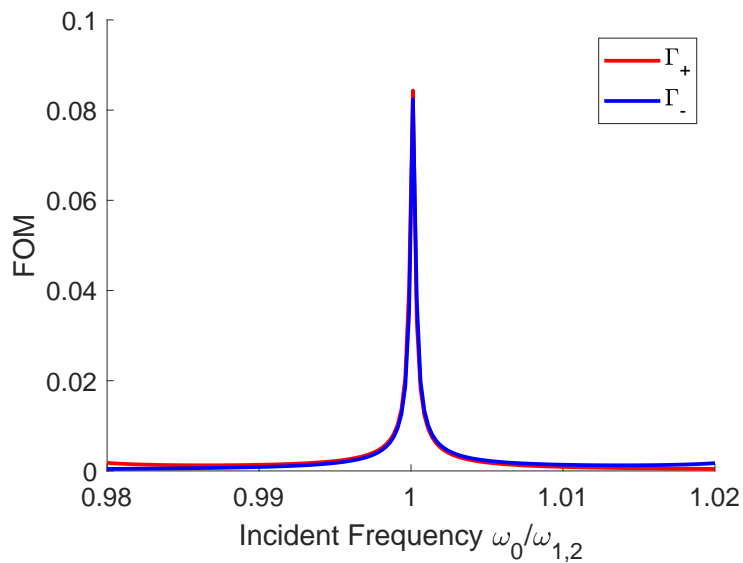
Figure 8.7: Figures of merit $\Gamma_\pm$ as a function of the incident frequency ω_0. In this case, $\delta = \Omega/4$ and $\omega_1 = \omega_2$. At the first band crossing ($\kappa \approx \Omega$), the frequency conversion is efficient and symmetric.

In this case, the incident frequency corresponds to a first-order mode while the two sidebands are zeroth order.
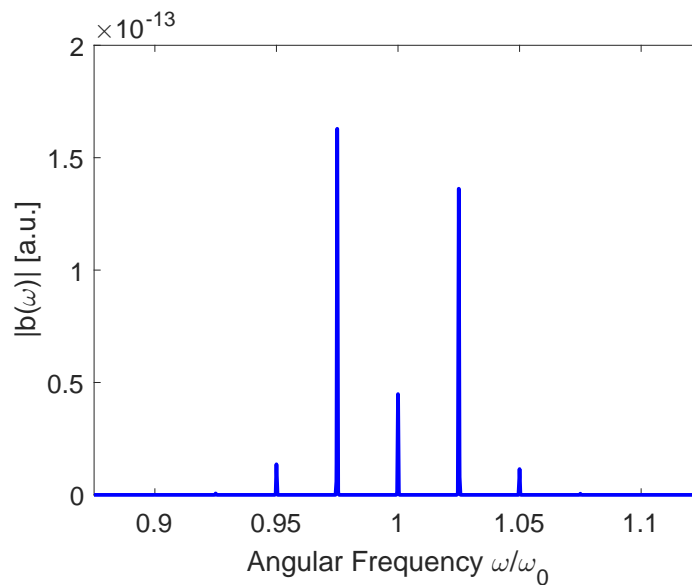
Figure 8.8: Comb produced by a set of parameters corresponding to the central peak of Figure 8.7. The conversion to the upper sideband ($\omega_0 + \Omega$) is nearly as efficient as the conversion to the lower sideband ($\omega_0 - \Omega$).

8.3.3   Non-degenerate case

In the above discussions we presented the degenerate case where $\omega_1 = \omega_2$. Here we briefly discuss the non-degenerate case to show that the same general conclusions apply. Firstly, the band structure is similar, which we can compare in Figure 8.9: the solid line is the degenerate situation, the dashed line is non-degenerate. Clearly, in the non-degenerate case, the Floquet bands no longer cross at $\kappa = 0$ as they did in the degenerate case, as the two cavities now have different resonance frequencies.
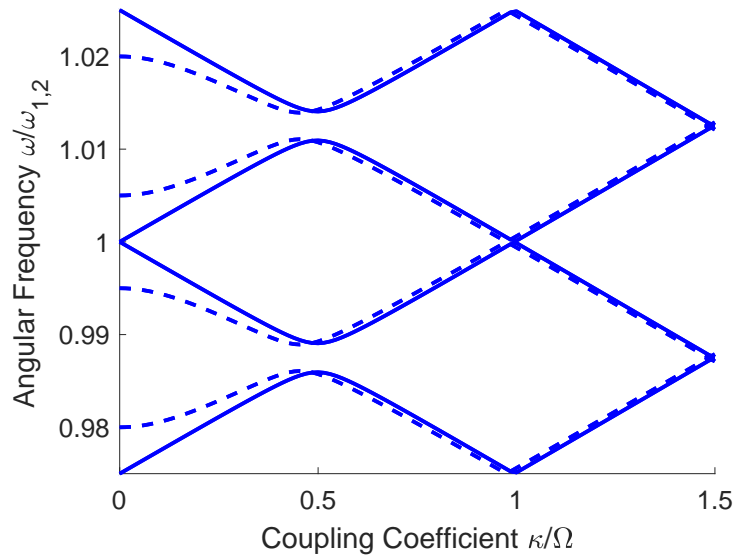
Figure 8.9: Solid blue lines: Floquet modes of the system for the degenerate case (same as in Figure 8.2). Dashed blue lines: non-degenerate case ($\omega_1 \neq \omega_2$). We chose these two frequencies such that $\omega_1 - \omega_2 = 2\Omega/5$.

We then consider the FOMs in the case where $\omega_1 \neq \omega_2$ around the first anti-crossing ($\kappa = \Omega/2$), see Figure 8.10, in order to compare it with the degenerate case (Section 8.3.1, Figure 8.4). Note that in the non-degenerate case, the Floquet bands are slightly shifted towards smaller κ values (compare solid and dashed lines in Figure 8.9). Here as well the conversion efficiency is improved when the source frequency is equal to a Floquet mode. The exact efficiency is different than in the degenerate case (Figure 8.4), because of the slight difference in resonance frequencies. We will see in the next section that this can be predicted by a simple model.

We also computed the FOMs for the symmetric regime ($\kappa \approx \Omega$) in the non-degenerate case, see Figure 8.11. Whereas in the degenerate case the two FOM peaks $\Gamma_\pm$ are maximal at the same frequency (Figure 8.7), here a small gap appears, meaning that the two Floquet modes do not have the same frequency, hence the peak position difference in Figure 8.11. This difference is not simply due to the slight shift of the band structure seen in Figure 8.9, here an anti-crossing opens whereas the two non-degenerate bands cross.
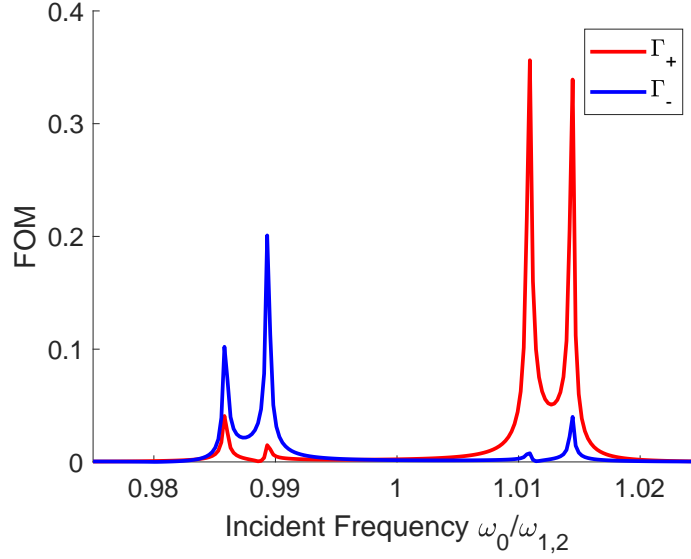
Figure 8.10: Figures of merit $\Gamma_\pm$ as a function of the incident frequency ω_0. In this case, $\delta = \Omega$, $\omega_2 - \omega_1 = 2\Omega/5$ and $\kappa = \Omega/2$ (around the anti-crossing).
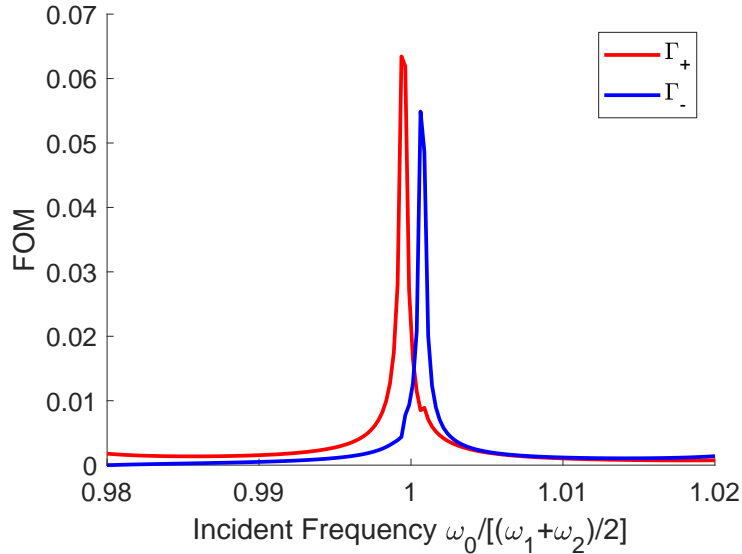
Figure 8.11: Figures of merit $\Gamma_\pm$ as a function of the incident frequency ω_0. In this case, $\delta = \Omega$, $\omega_1 - \omega_2 = 2\Omega/5$ and $\kappa \approx \Omega$ (around the second anti-crossing).

8.4 Three-frequency model

In order to find the correct system parameters that enable selective frequency conversion, we can use a simplified model, where we only consider three frequencies for the two cavity mode amplitudes $a(\omega)$ and $b(\omega)$: at the source frequency ω_0 and at the two sidebands $(\omega_0 - \Omega)$ and $(\omega_0 + \Omega)$. In detail, we consider solutions of the form $f(\omega) = f_- \delta\left[\omega - (\omega_0 - \Omega)\right] + f_0 \delta\left[\omega - \omega_0\right] + f_+ \delta\left[\omega - (\omega_0 + \Omega)\right]$, where f represents the two mode amplitudes a and b. With these assumptions the CMT Equations 8.1-8.3

become:

$$j(\omega_0 - \Omega)a_- = j\omega_1 a_- + j\kappa b_- \qquad (8.11)$$

$$j\omega_0 a_0 = j\omega_1 a_0 + j\kappa b_0 + s_0 \qquad (8.12)$$

$$j(\omega_0 + \Omega)a_+ = j\omega_1 a_+ + j\kappa b_+ \qquad (8.13)$$

$$j(\omega_0 - \Omega)b_- = j\omega_2 b_- + \frac{\delta}{2}b_0 - \gamma b_- + j\kappa a_- \qquad (8.14)$$

$$j\omega_0 b_0 = j\omega_2 b_0 + \frac{\delta}{2}b_- + \frac{\delta}{2}b_+ - \gamma b_0 + j\kappa a_0 \qquad (8.15)$$

$$j(\omega_0 + \Omega)b_+ = j\omega_2 b_+ + \frac{\delta}{2}b_0 - \gamma b_+ + j\kappa a_+ \qquad (8.16)$$

As seen in Equations 8.11-8.16, the coupling coefficient κ accounts for the coupling between dark and bright mode at the same frequency, while the modulation amplitude δ accounts for the coupling between the different frequency components of the bright mode b. Note that this equation system actually corresponds to the 6×6 central part of the Floquet matrix of Equation 8.10. This model has the advantage of being an algebraic system, whereas the previous results were obtained through the numerical resolution of the differential equation system of Equations 8.1 and 8.2. It can be used to rapidly explore various situations, for example the non-degenerate case. However, since we only take into account three frequency components per mode, this model is an approximation, but it can lead to quantitatively correct results, especially in our selective cases.

We compare the results of this simple model with the numerical resolution of Equations 8.1 and 8.2 for two specific cases. The first case is symmetric around ω_0, so we impose $b_- = b_+$ in Equations 8.11-8.16. A set of parameters found with that constraint is $\kappa = \Omega$, $\delta = \Omega/4$ and $\omega_0 = \omega_1 = \omega_2$. This specific case is represented in Figure 8.12(a). In the second case, the parameters are chosen such that the conversion to the lower frequency sideband is maximized. Parameters can be found by imposing $b_0 = b_+ = 0$ in Equations 8.11-8.16, giving for example $\kappa = \Omega/2$, $\omega_1 = \omega_0 - \kappa$, $\delta = \Omega/4$. The results for this second set of parameters are represented in Figure 8.12(b). In both cases a qualitative agreement is found. The difference between the three-frequency model and the numerical results can be explained by the simplicity of the model: we only consider three frequency components while more components are involved in the rigorous system.

This simple model allows for a more systematic approach in tuning the output spectrum: one can impose constraints in Equations 8.11-8.16, and solve for the system parameters that will give a desired response (as we did for Figure 8.12). It also allows to understand the interference effects between the frequency components, as in some cases terms in Equations 8.11-8.16 cancel out, giving a single frequency output, as in Figure 8.12(b). Moreover it is a useful analytic alternative to the numerical resolution of the CMT equations.
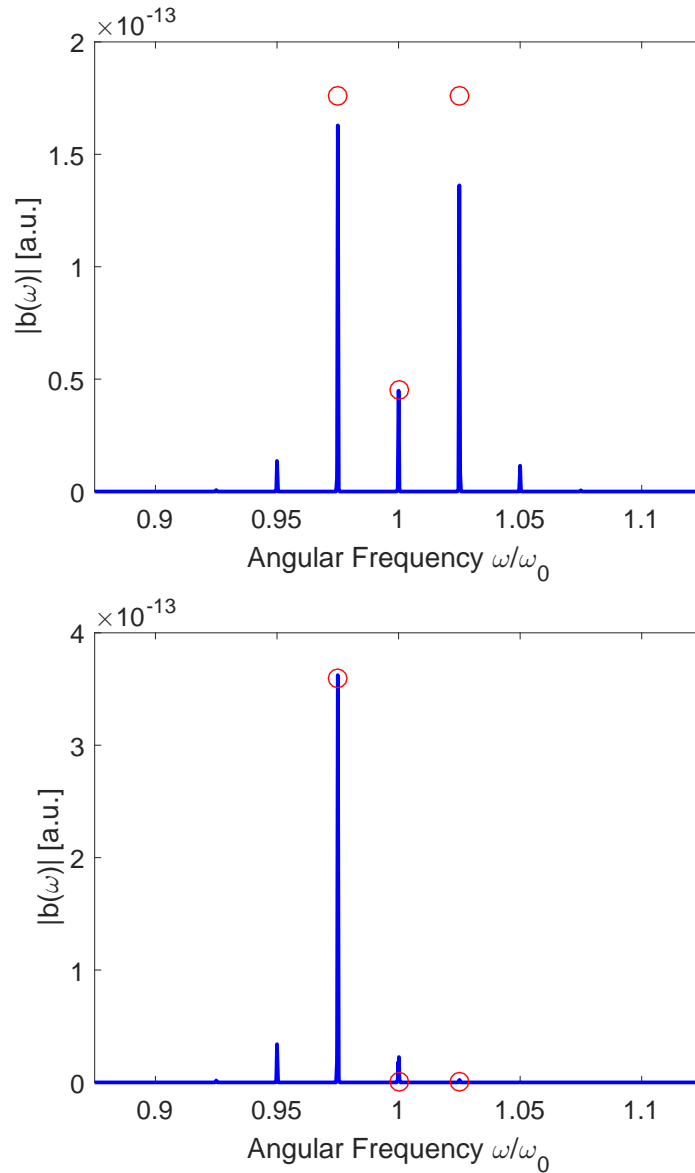
Figure 8.12: Red circles are the results of the three-frequency model while the blue line is the full numerical solution. In (a) we imposed the constraint $b_- = b_+$ so the comb generated is perfectly symmetric. In (b) we imposed the constraint $b_0 = b_+ = 0$, so the frequency conversion is asymmetric.

8.5 Two-level perturbation

To obtain an analytical expression for the Floquet bands we can use a two-level perturbation theory [93, 94, 128]. This is useful to obtain a simple expression for the Floquet bands, so one knows which frequencies are bound to provide a good potential conversion. For simplicity we only discuss the degenerate case.

We approximate the initial Floquet Hamiltonian by a 2×2 Hamiltonian, where the contribution of the other Floquet modes is treated as a perturbation [93]. To do so, we separate the Floquet Hamiltonian of Equation 8.10 into a static matrix H_0 and a perturbation matrix V containing only δ terms (the perturbation method

is described in Section 5.3 and here the H_0 corresponds to E^0 in Equation 5.34).
We apply a transformation to H_0 and V so that H_0 is diagonal and write out the
eigenvalue equation component by component. Then we solve for the eigenvector
components and find that they are the solution of an implicit equation involving
the sum of the eigenvector components. We identify two large terms (corresponding
to the crossing of static modes) and separate them from the rest of the sum. Then
by iteration and by considering the first order of the perturbation, we find the two
resonance frequencies of the nearly degenerate states. As seen in Figure 8.2, the
unperturbed bands $\omega_{1,2} + \kappa$ and $\omega_{1,2} + \Omega - \kappa$ cross at $\kappa = \Omega/2$, and open an anti-
crossing in the Floquet bands. We choose these bands as the two unperturbed states
for the perturbation analysis. After a few manipulations, the perturbed Hamiltonian
becomes:

$$H_2 = \begin{bmatrix} \omega_{1,2} + \Omega - \kappa + \Delta(\kappa) & \delta/4 \\ \delta/4 & \omega_{1,2} + \kappa - \Delta(\kappa) \end{bmatrix} \tag{8.17}$$

where $\Delta(\kappa) = \dfrac{\delta^2}{16(2\kappa + \Omega)}$ is the correction to the 'static' levels induced by the
time modulation. The eigenvalues of H_2 are approximations of the Floquet mode
frequencies, and are given by:

$$\omega_\pm = \omega_{1,2} + \frac{\Omega}{2} \pm \frac{\sqrt{\delta^4 + 64\delta^2\kappa(\Omega + 2\kappa) + 64(\Omega^2 - 4\kappa^2)^2}}{16(2\kappa + \Omega)} \tag{8.18}$$

Since the potential has a periodicity Ω, it is possible to completely describe all the
eigenvalues of the infinite Floquet Hamiltonian with the two eigenvalues of H_2, by
adding multiples of the modulation frequency Ω. In Figure 8.13 we compare the
numerical eigenvalues of the Floquet matrix to the perturbation theory results. We
obtain a very good agreement between the numerical eigenvalues (truncated Equa-
tion 8.10) and the analytical eigenvalues obtained via perturbation theory (Equa-
tion 8.18).

Furthermore, this perturbation analysis allows us to find an analytical approx-
imation for the coupling coefficient κ_c, where the Floquet modes cross for the first
time (around $\kappa = \Omega$). By imposing that the two eigenvalues $\omega_\pm$ of Equation 8.18
must be equal and solving for κ, we find (after neglecting δ^2 terms):

$$\kappa_c = \frac{\Omega}{4}\left(1 + 3\sqrt{1 - \frac{2\delta^2}{9\Omega^2}}\right) \tag{8.19}$$

From this expression, we see that without perturbation the bands indeed cross at
$\kappa = \Omega$ as expected (see Figure 8.2). This is why we employed $\kappa \approx \Omega$ for the band
crossing in the previous sections.

8.6   Conclusion

An efficient and tailored frequency conversion can be achieved with a system of cou-
pled time-modulated cavities. We describe this process using the CMT equations
adapted to time-dependent resonance frequencies. The system supports Floquet
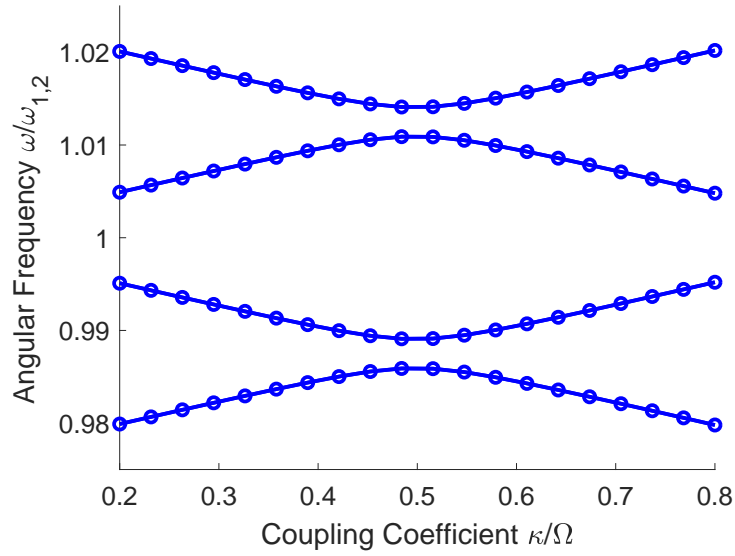
Figure 8.13: Solid lines: Numerical results for the eigenvalues of the Floquet matrix. Circles: Equation 8.18 and with Ω offset. The parameters used are the same as in Figure 8.2.

modes, arising from the time periodicity, which play an important role in the conversion efficiency. Furthermore, their band-like structure is a key element, as the conversion is enhanced in the neighbourhood of (anti-)crossings.

We exploit the coupled-cavity setup to achieve both symmetric and asymmetric frequency conversion, using the important link of these two processes with the Floquet modes. We employ perturbation theory to find an analytic approximation of the Floquet bands. Furthermore, we show how to find useful system parameters for selective frequency conversion using a straightforward three-frequency model.

This frequency conversion mechanism is fairly general, since it only requires two coupled, time-modulated resonances, such as recently demonstrated in [129]. It can thus be applied to a wide range of physical systems, ranging from photonics to acoustics for example.

9

Time-modulated BIC states

In this chapter we study the outcoupling of a time-modulated system of two coupled modes inside a cavity, in a specifically tailored setup. As we saw in Chapter 8, a system modulated periodically in time exhibits Floquet modes, and their eigenfrequencies are separated by the modulation frequency Ω. This time, the system under investigation is coupled to one channel, and we study in more detail the decay mechanism, when the system exhibits a Bound State in the Continuum (BIC).

In contrast, in the two cavity system of Chapter 8, we only considered the case where one cavity supports a dark mode (that does not couple to the ports) and a bright mode (that couples to the continuum). The outcoupling was taken into account only by considering the power escaping from the bright mode. In this chapter, we consider a more general case.

9.1   Static BIC states

Bound States in the Continuum (BICs) are states that remain localized, even though they are connected to a continuum of waves that should allow energy to leak from the mode [130]. Usually, to determine if a mode is perfectly confined, one simple clue is to look at its frequency: if the mode frequency is outside the spectral range of the radiation channels, then the state is considered as decoupled from the radiation

and it is perfectly confined: no energy can escape. An example is a localized defect mode in the bandgap of a photonic crystal. In the opposite case, a state that lies in a continuum of states is often a leaky mode, since its energy can couple to radiation channels. A BIC state is a very peculiar case that does not fall in the two descriptions above: it is a perfectly confined mode, yet inside a continuum of states.

BIC states can be found in a wide variety of physical systems, and one can separate BIC states in several categories. In symmetry-protected BICs, a single state with a given symmetry class can be embedded in a continuum of modes of another symmetry class. In that case, since the two symmetry classes are usually decoupled, no energy exchange occurs between the single mode and the continuum of modes. This kind of BIC state has been studied in sound waves [131, 132], and in water waves [133, 134]. In photonics, a realization of BIC states was implemented by introducing an odd defect mode in a 1D waveguide supporting a continuum of even modes [135–137].

A different common class of bound states are the Fabry-Pérot BICs. When a resonant cavity is coupled to a single waveguide, it can cause unity reflection. If two of these cavities are present in a waveguide, they can act as a pair of perfect mirrors, effectively trapping light in between them. In this structure, BICs are formed when the frequency of the individual resonators and the separation between them is tuned so that the phase acquired during a round-trip is an integer multiple of 2π. In the end this structure closely resembles a Fabry-Pérot cavity formed by two perfectly reflecting mirrors. This type of BIC can be found in water waves [138, 139], and in photonics in a waveguide connected to resonant defects [140].

Another type of bound state is closely related to the Fabry-Pérot BICs: Friedrich-Wintgen BICs. In Fabry-Pérot BICs, the two resonances are separated by a given distance. This is not necessary for the existence of a BIC state: if the two resonances are supported by the same cavity and have different resonance frequencies, with different radiation rates into the same channel, the interference can lead to a BIC. In other words, a multimode cavity coupled to a radiation channel can support BIC states when the system parameters are properly tuned so that destructive interferences occur between the radiations leaving the cavity. In photonics, such BIC states have been studied in multimode cavities coupled to microwave waveguides [141, 142] and in 'dark-state' lasers [143].

In this chapter, the system under investigation consists of a single cavity supporting two modes (Figure 9.1). These two modes are each coupled to two output ports, so we expect Friedrich-Wintgen BICs for some specific cases. This system could represent a multimode cavity coupled to a regular photonic waveguide, or to a photonic crystal waveguide. The cavity can represent a plasmonic mode, for example graphene plasmonic resonances, as we discussed in Chapter 6. We will describe this setup with a CMT model for a multimode cavity, as introduced in Chapter 5:

$$\frac{d\mathbf{a}}{dt} = (j\Omega - \Gamma)\mathbf{a} + K^T \left| s_+ \right\rangle, \tag{9.1}$$

$$\left| s_- \right\rangle = C \left| s_+ \right\rangle + D\mathbf{a}. \tag{9.2}$$

The two modes inside the cavity are represented by their mode amplitudes $a(t)$ and $b(t)$ contained in the vector $\mathbf{a}$, normalized such that $|a(t)|^2$ and $|b(t)|^2$ correspond to the energy of the corresponding modes. These two modes have resonance
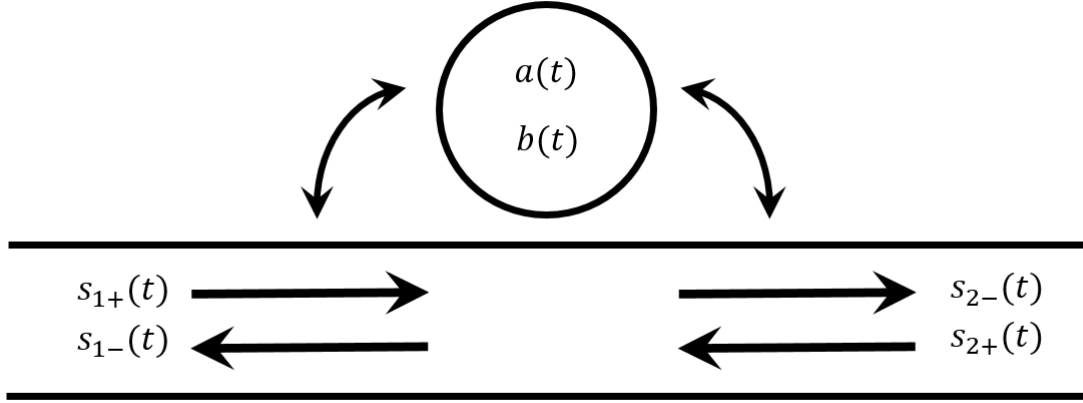
Figure 9.1: Schematic of the system described by Equations 9.1 and 9.2. Typically, this model represents a multimode cavity coupled to a waveguide (2 output ports). A direct channel is also present, taking into account the direct transport process, without interaction with the cavity modes. This system is also suitable to describe a plasmonic cavity (in graphene for example) coupled to plane waves.

frequencies corresponding to the diagonal elements of Ω and are coupled between them by the off-diagonal elements of Ω. The two modes are coupled to input ports $|s_+\rangle$ via the matrix K, and to output ports $|s_+\rangle$ via the matrix D. The matrix C accounts for direct transport between the input and output ports, without interaction with the cavity. As described in Chapter 5, energy conservation, mirror symmetry and time-reversal symmetry impose that:

$$D^+D = 2\Gamma, \tag{9.3}$$

$$K = D, \tag{9.4}$$

$$CD^* = -D. \tag{9.5}$$

Explicitly, by considering Equations 9.3 to 9.5 this system reads:

$$\frac{d}{dt}\begin{pmatrix} a(t) \\ b(t) \end{pmatrix} = \left[j\begin{pmatrix} \omega_1 & \kappa \\ \kappa & \omega_2 \end{pmatrix} - \begin{pmatrix} \gamma_1 & \gamma_0 \\ \gamma_0 & \gamma_2 \end{pmatrix} \right] \begin{pmatrix} a(t) \\ b(t) \end{pmatrix} + \begin{pmatrix} \sqrt{\gamma_1} & \sqrt{\gamma_1} \\ \sqrt{\gamma_2} & \sqrt{\gamma_2} \end{pmatrix} \begin{pmatrix} s_{1+}(t) \\ s_{2+}(t) \end{pmatrix} \tag{9.6}$$

$$\begin{pmatrix} s_{1-}(t) \\ s_{2-}(t) \end{pmatrix} = \begin{pmatrix} r_d & t_d \\ t_d & r_d \end{pmatrix} \begin{pmatrix} s_{1+}(t) \\ s_{2+}(t) \end{pmatrix} + \begin{pmatrix} \sqrt{\gamma_1} & \sqrt{\gamma_2} \\ \sqrt{\gamma_1} & \sqrt{\gamma_2} \end{pmatrix} \begin{pmatrix} a(t) \\ b(t) \end{pmatrix} \tag{9.7}$$

where $\omega_{1,2}$ are the resonance frequencies of modes a and b, respectively, κ is the coupling between the two modes, $\gamma_{1,2}$ are the decay rates, and t_d and r_d are the transmission and reflection coefficients of the direct process. If the two modes have the same parity, $\gamma_0 = \sqrt{\gamma_1\gamma_2}$, but if the two modes have opposite parity, $\gamma_0 = 0$. In this chapter, we will consider the case where the two modes have the same parity, as this leads to interesting interactions with the output ports.

One can define the Hamiltonian of this system as:

$$H = \begin{pmatrix} \omega_1 & \kappa \\ \kappa & \omega_2 \end{pmatrix} + j\begin{pmatrix} \gamma_1 & \sqrt{\gamma_1\gamma_2} \\ \sqrt{\gamma_1\gamma_2} & \gamma_2 \end{pmatrix}. \tag{9.8}$$

We use the convention $e^{j\omega t}$, so eigenvalues $\omega_\pm$ of H such that $\text{Im}(\omega_\pm) > 0$ are the eigenvalues of lossy modes. For the simple case where the modes are degenerate ($\omega_1 = \omega_2 = \omega_{1,2}$ and $\gamma_1 = \gamma_2 = \gamma_{1,2}$), the eigenvalues $\omega_\pm$ of H take the simple form

$$\omega_- = \omega_{1,2} - \kappa \quad \omega_+ = \omega_{1,2} + \kappa + 2j\gamma_{1,2}. \tag{9.9}$$

This simple system already exhibit an interesting feature: one of the two eigenstates (corresponding to the eigenvalue ω_-) is a Friedrich-Wintgen BIC state (see Figure 9.2). The state corresponding to the ω_- eigenvalue is a BIC state because it lies in a continuum of states (the radiation through the ports) and is coupled to them but yet it does not decay into the continuum of modes. The lifetime of an eigenstate can be defined as $\tau_{\text{mode}} = 1/\left(2|\text{Im}(\omega_\pm)|\right)$, which means that a mode with an eigenvalue such that $\text{Im}(\omega_\pm) = 0$ will have an infinite lifetime (and Q-factor). As such, it cannot be excited through an input port and, once excited by other means, does not decay in any of the output ports. Note that in this case, the BIC state exists for all the values of κ. The eigenvectors corresponding to the eigenvalues $\omega_\pm$ are:

$$\boldsymbol{\omega}_- = \begin{pmatrix} -1 \\ 1 \end{pmatrix} \quad \boldsymbol{\omega}_+ = \begin{pmatrix} 1 \\ 1 \end{pmatrix}. \tag{9.10}$$

One can get an intuitive understanding of the BIC state isolation from the ports: the two cavity modes oscillate with opposite phases and radiate into the ports with the same rate since the decay rates of the two cavity modes are equal. This leads to destructive interference and prevents the BIC state from leaking to the output ports.
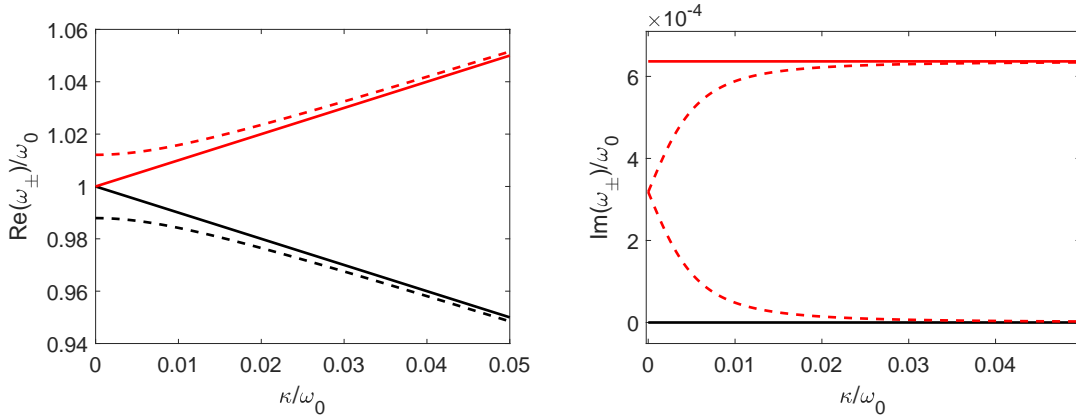
Figure 9.2: Solid lines: eigenvalues $\omega_\pm$ for the degenerate case ($\omega_1 = \omega_2$, $\gamma_1 = \gamma_2$). Dashed lines: eigenvalues $\omega_\pm$ for the non-degenerate case ($\omega_1 \neq \omega_2$, $\gamma_1 = \gamma_2$). We define $\omega_0 = (\omega_1 + \omega_2)/2$. While a BIC state always exists for the degenerate case, in the non-degenerate case both modes have a non-zero imaginary part for all the κ values.

It is then expected that a system in the initial state $\boldsymbol{\omega}_+$ corresponding to the ω_+ eigenvalue will decay into the ports in the degenerate case since its eigenvalue always has a non-zero imaginary part. We solved the system of Equations 9.6 and 9.7 for an initial state $\boldsymbol{\omega}_+$ in Figure 9.3 and $\boldsymbol{\omega}_-$ in Figure 9.4.
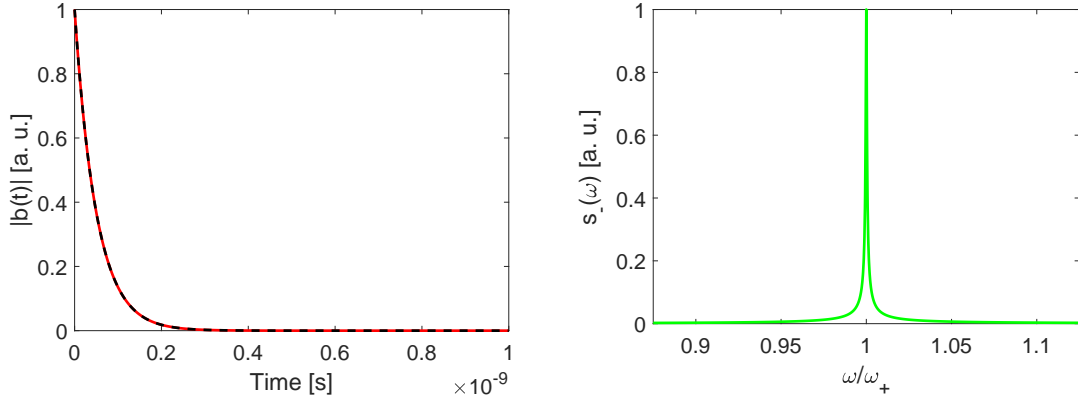
Figure 9.3: Left: Evolution of the (modulus of the) $\boldsymbol{\omega}_+$ eigenstate in the time domain. The red line is the numerical resolution of the CMT system of equations while the black dashed line is the theoretical result obtained with the imaginary part of the eigenvalue. Right: output in the frequency domain (we use the notation s_- for the output port since $s_{1-}(t) = s_{2-}(t)$. The outgoing wave has the frequency of the eigenvalue ω_+.

Once excited, both initial states oscillate at frequency $\mathrm{Re}(\omega_\pm)$ and decay with a rate $\mathrm{Im}(\omega_\pm)$. The $\boldsymbol{\omega}_+$ state decays into the ports and the outgoing wave is centered around the frequency ω_+. For the $\boldsymbol{\omega}_-$ state however, no outgoing wave is present, and all the energy stays trapped in the BIC mode, even though both cavities are coupled to output ports.
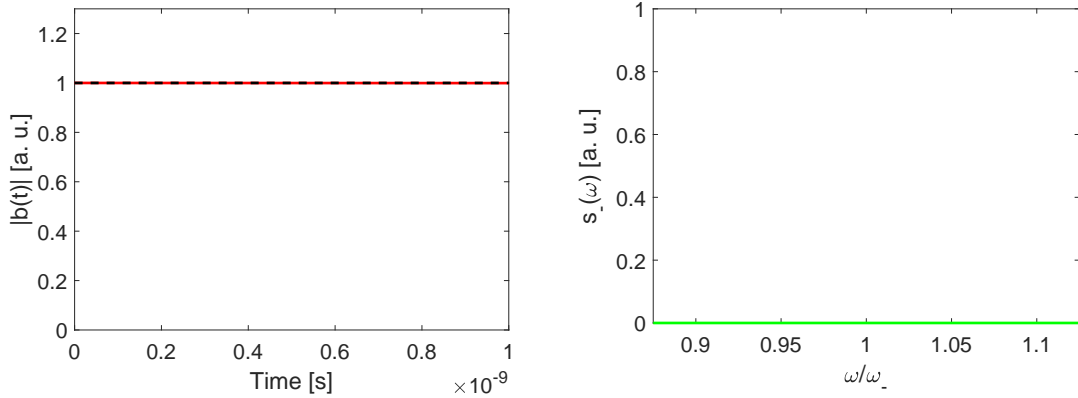
Figure 9.4: Left: Evolution of the (modulus of the) $\boldsymbol{\omega}_-$ eigenstate in the time domain. Light stays trapped into the eigenstate and does not decay, since the imaginary part of the eigenvalue is equal to zero. Right: output in the frequency domain. No wave leaves the eigenstate through the output port.

In the general case, a BIC mode in a system of two coupled cavities will exist when the following condition is fulfilled [130]:

$$\kappa(\gamma_1 - \gamma_2) = \sqrt{\gamma_1 \gamma_2}(\omega_1 - \omega_2). \tag{9.11}$$

From this expression, one finds that all the degenerate systems ($\omega_1 = \omega_2$ and $\gamma_1 = \gamma_2$)

will support a BIC state, for all κ values. For non-degenerate systems however, a
BIC state will only exist for one value of κ. We illustrate this in Figure 9.5.
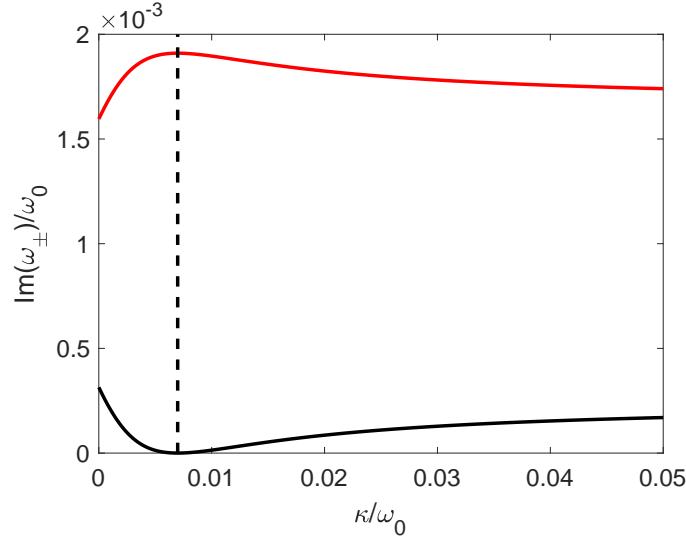
Figure 9.5: Imaginary part of the eigenvalues $\omega_\pm$ as a function of the coupling
coefficient κ. A BIC state appears when the condition of Equation 9.11 is fulfilled
(vertical dashed line). At that value, one of the eigenvalues imaginary part vanishes.
In this case, $\omega_2 - \omega_1 = 7.8 \times 10^{11}$ rad/s, $\gamma_1 = 2 \times 10^{10}$ rad/s, $\gamma_2 = 10\gamma_1$ and
$\omega_0 = (\omega_1 + \omega_2)/2$.

9.2   Dynamic BIC states

In this section we investigate the behaviour of BIC states in time-modulated struc-
tures. The system we use is the same as in Figure 9.1, but this time the resonance
frequencies ω_1 and ω_2 will be time-modulated. This modulation will be periodic,
meaning that the Hamiltionian of Equation 9.8 will also be periodic. As we saw in
Chapter 8, a Hamiltonian in that case supports Floquet modes, and we presented a
method to find its eigenvalues. We will use the same tools in this chapter.

First, we are interested in finding the imaginary part of the Floquet eigenvalues.
In the previous chapter, we only focused on the real part of these eigenvalues since
we were studying the interference effects between the two cavity modes. Here, we
will study the losses of the Floquet modes, governed by the imaginary part of the
corresponding Floquet eigenvalue. We will first consider the case where one of the
cavity modes is modulated. The time modulation for the cavity resonance frequency
is:

$$\omega_2(t) = \omega_2 + \delta \sin(\Omega t) \tag{9.12}$$

with ω_2 the 'static' resonance frequency, δ the modulation amplitude and Ω the
modulation frequency. The modulation amplitudes δ we consider here are of the
same order of magnitude as Ω.

Using the tools from the previous chapter, we can represent the Floquet eigen-
values (real and imaginary parts) as a function of κ in Figure 9.6. These Floquet

mode are different than the 'static' modes: as previously, the resonance frequencies are adjusted, and there are multiple Floquet branches, separated by the modulation frequency Ω.
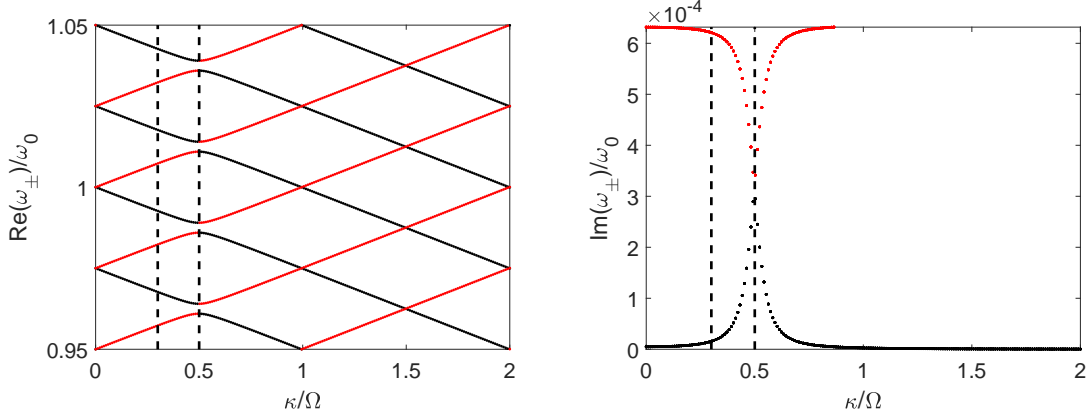
Figure 9.6: (Left:) Real and (Right:) imaginary part of the Floquet mode eigenfrequencies. Black (red) lines represent modes with a lower (higher) imaginary part. An anti-crossing appears at $\kappa = \Omega/2$. At that value, the modes mix and have the same decay rate. For $\kappa \to \infty$ and $\kappa \to 0$, one of the Floquet modes is nearly a BIC state. Here $\omega_1 = \omega_2$, $\gamma_1 = \gamma_2 = 2 \times 10^{10}$ rad/s and only the second cavity mode is modulated (following Equation 9.12). The black dashed lines denote the cases used in Figure 9.7.

In Figure 9.6, an anti-crossing appears at $\kappa = \Omega/2$, where the unperturbed modes (see Figure 9.2) would cross. The Floquet modes can be separated in two branches: one branch (red) in Figure 9.6 with a 'bright' nature, and one (black) with a lower imaginary part of the eigenvalues (partially 'dark'). For a given κ, all the bright and dark branches have the same imaginary part of their eigenvalue, respectively, while the real part of their eigenvalue is separated by $n\Omega$, where n is an integer. The bright and dark Floquet branches follow the static system modes of Figure 9.2.

When the system is excited in a superposition of static states $(\boldsymbol{\omega}_+ + \boldsymbol{\omega}_-)$, the initial state will decay with two different rates into the port, corresponding to the two different imaginary parts of the Floquet modes. The black lines in the Floquet diagram of Figure 9.6 denote the two cases where the decay into the output port is represented in Figure 9.7.

From Figure 9.7, we see that the two Floquet modes decay at very different rates into the output port. The bright mode decays very rapidly from the cavity, leaving only the dark mode inside, which decays at a much slower rate if the two Floquet modes have a different imaginary part. However, at the anti-crossing ($\kappa = \Omega/2$), the two branches have the same imaginary part and therefore decay at the same rate. So, in general, time modulation seems to break the BIC character, as the original BIC mode becomes mixed with the non-BIC mode.

We also study the two-cavity system where the two resonance frequencies are time-modulated. If they are both modulated in phase, so $\omega_1 = \omega_2$ and $\gamma_1 = \gamma_2$, then at all times, the two cavity modes have the same frequency and decay rate, and thus the system is at all times doubly degenerate. The Floquet modes of that
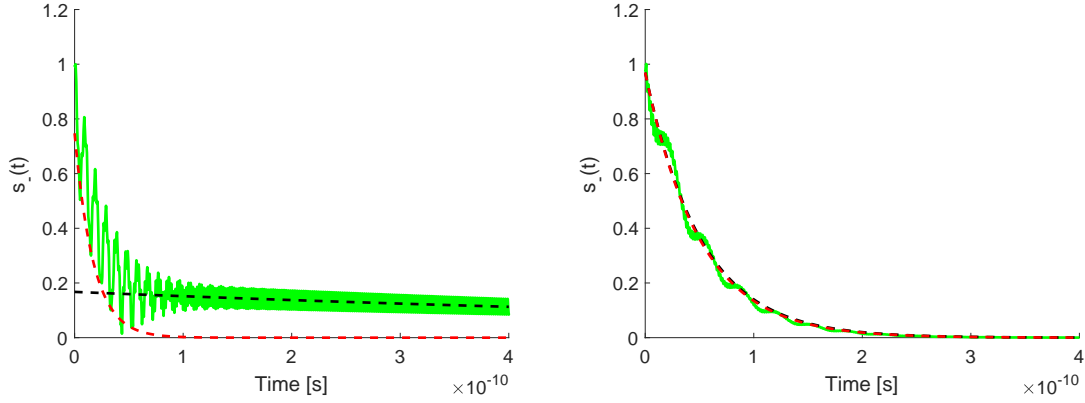
Figure 9.7: Left: Double exponential decay of the cavity modes into the output port. We used the system parameters from Figure 9.6, and $\kappa/\Omega = 0.3$ (black dashed line on the Floquet diagram). Right: Same parameters values but this time, since we are at the anti-crossing ($\kappa = \Omega/2$), the two modes decay with the same rate. The red (black) dashed curves are exponentials with a decay rate corresponding to the bright (dark) Floquet branches.

system are represented in Figure 9.8. In this case, the Floquet modes are simply the
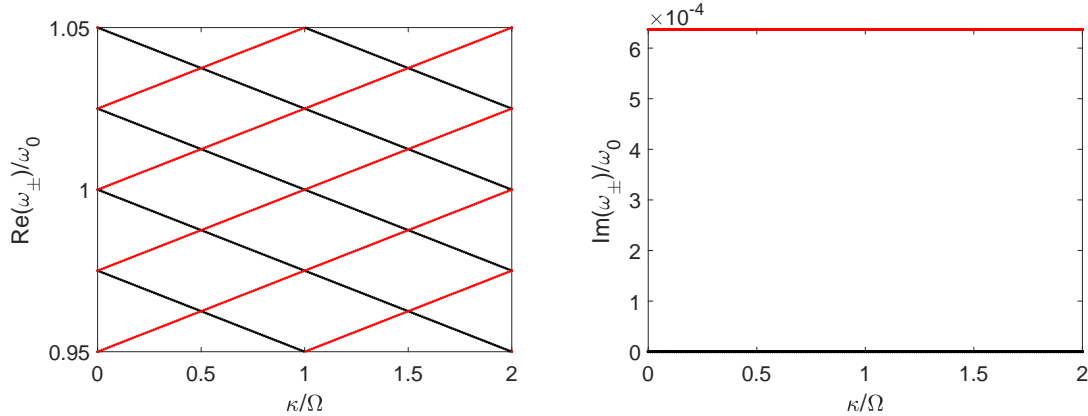
Figure 9.8: (Left:) Real and (Right:) imaginary part of the Floquet mode eigenfrequencies where $\omega_1(t) = \omega_2(t)$ and $\gamma_1 = \gamma_2$. Unlike the case where only one mode is modulated, here the crossing of the unperturbed modes does not open an anticrossing. The values used for this figure are the same as in Figure 9.6 (except that both modes are identically modulated). In this case, the Floquet modes on the 'dark' branch always correspond to a BIC state, much like the static case of Figure 9.2.

static system modes separated by the modulation frequency Ω. Moreover, one of the modes is a BIC state for all κ values because condition 9.11 is instantaneously correct at all times. This is a first sign that a particular time modulation can restore the BIC character.

    If the two initial cavity modes have the same (real part of the) resonance frequency, but a different decay rate, and when only one of the two modes is modulated, the system is no longer degenerate. Then an anti-crossing appears at $\kappa = \Omega/2$ where

the eigenfrequencies of the two Floquet branches have the same imaginary part (Figure 9.9). Unlike the case represented in Figure 9.6, here there is no quasi-BIC state
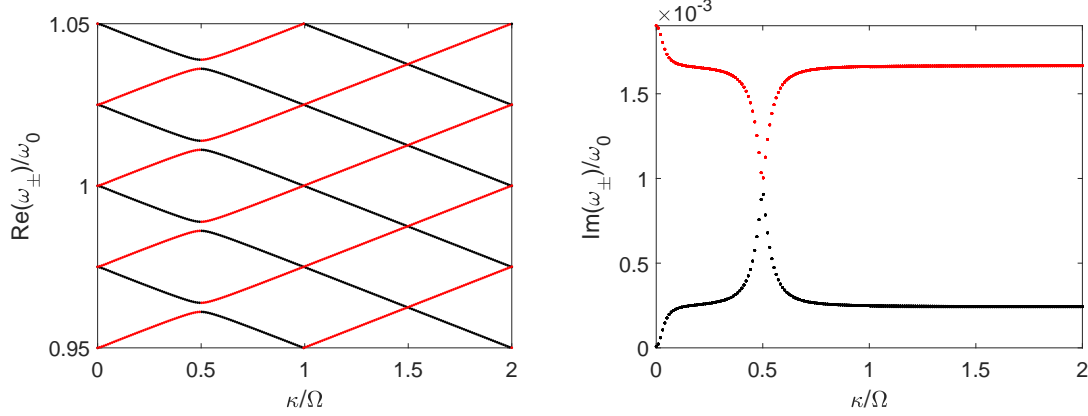
Figure 9.9: (Left:) Real and (Right:) imaginary part of the Floquet mode eigenfrequencies where $\gamma_1 = 2 \times 10^{10}$ rad/s and $\gamma_2 = 5\gamma_1$. Only the second mode is modulated. Since $\gamma_1 \neq \gamma_2$, the condition of Equation 9.11 is only fulfilled when $\kappa = 0$.

for $\kappa \to \infty$. This is because the condition of Equation 9.11 cannot be fulfilled: the left hand side of Equation 9.11 is non-zero, while the right hand side is zero because the two cavities have the same resonance frequency. However a BIC state still exists at $\kappa = 0$.

From Equation 9.11, it seems that it is possible to obtain a 'dynamic BIC state' for any κ value by choosing a modulation that satisfies

$$\omega_2(t) = \omega_1(t) - \kappa \frac{\gamma_1 - \gamma_2}{\sqrt{\gamma_1 \gamma_2}}. \tag{9.13}$$

By choosing an $\omega_2(t)$ that satisfies Equation 9.13 for a given $\omega_1(t)$, the Floquet diagrams are modified (Figure 9.10). A BIC state exists even when $\omega_1 \neq \omega_2$ and $\gamma_1 \neq \gamma_2$. In contrast, the dynamic BIC state in Figure 9.8 was obtained because the 'static' system was degenerate, which is no longer the case here. The 'static' modes of that system are modified since the unperturbed frequency of the second mode is now a function of κ ($\omega_2 \to \omega_2 - \kappa(\gamma_1 - \gamma_2)/\sqrt{\gamma_1 \gamma_2}$), while the unperturbed frequency of the first mode stays unchanged.

As seen in Figure 9.10, the dark branch of the Floquet modes only contains BIC states, which do not couple with the continuum. Their eigenvectors actually correspond to those of the static system (Equation 9.10). As in the static system supporting a BIC state, if an eigenvector is excited in the BIC state, it will stay trapped in the cavity, even if the system is non-degenerate and if a time modulation is present. We check this by solving the system of Equations 9.1 and 9.2 with the initial state $\boldsymbol{\omega}_-$ from Equation 9.10. The time evolution of the cavity mode $b(t)$ and the output s_- in the frequency domain are shown in Figure 9.11.
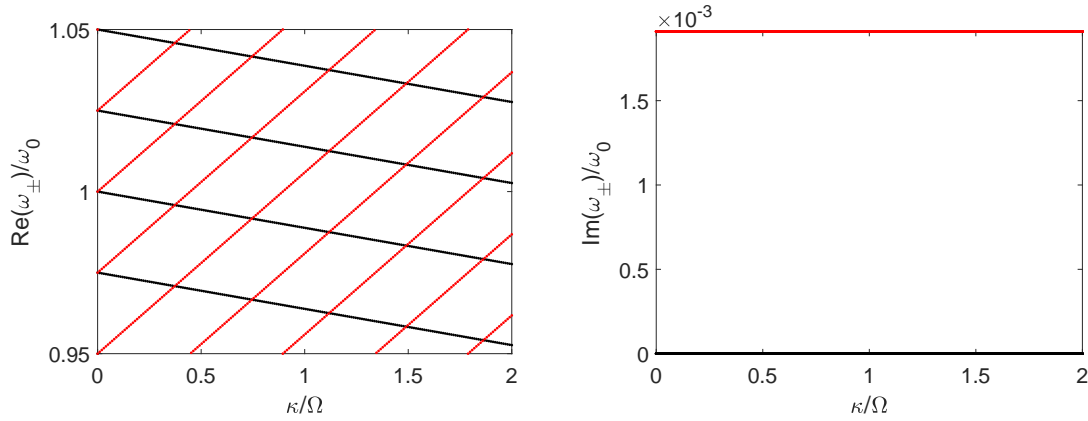
Figure 9.10: (Left:) Real and (Right:) imaginary part of the Floquet mode eigenfrequencies where ω_1 is modulated as in Equation 9.12, ω_2 follows Equation 9.13, $\gamma_1 = 2 \times 10^{10}$ rad/s and $\gamma_2 = 5\gamma_1$. The Floquet eigenvalues follow the 'static' eigenvalues of the system with an added $n\Omega$ frequency, with n an integer. A BIC state is present for all the κ values.
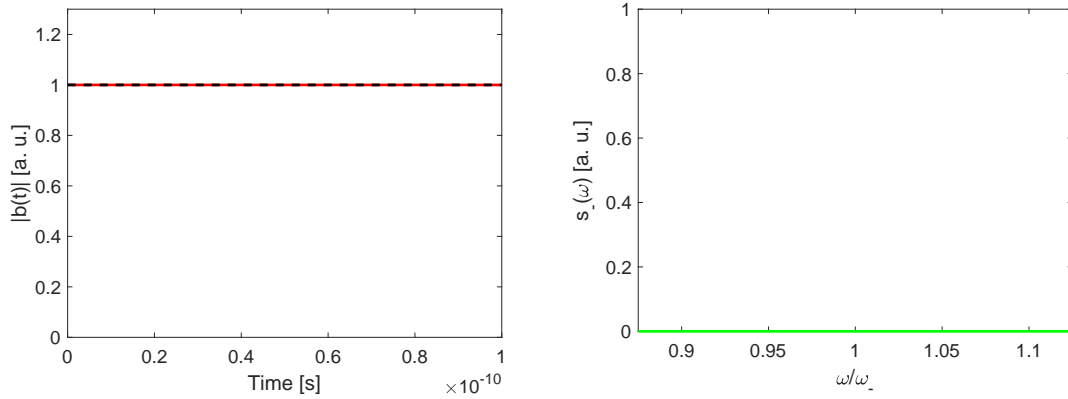
Figure 9.11: Left: Time domain evolution of the (modulus of the) cavity mode b. Once in the initial state $\boldsymbol{\omega}_-$, the system evolves at the eigenfrequency ω_- without any decay into the output ports. Right: Output s_- in the frequency domain. Since the system is in a BIC state at all times, no light leaks through the ports, even though the system is time-modulated. In this figure, the first mode frequency is modulated around $\omega_1 = 2\pi \times 10^{13}$ rad/s, $\gamma_1 = 2 \times 10^{10}$ rad/s and $\gamma_2 = 5\gamma_1$.

9.3   Conclusion

In this section, we studied dynamic Floquet modes in a multimode coupled cavity. We first described the modes of a 'static' system where in some cases BIC states can exist. Once excited, these modes stay trapped inside the cavity and do not leak through the output ports.

We then studied in detail the Floquet modes when this system is time-modulated, using the tools of Chapter 8 to obtain the Floquet eigenfrequencies. The two main Floquet branches are different, as one is formed of 'dark' modes, while the other is composed of 'bright' modes. However, typically, a time-modulated static BIC will

obtain a leaky character, as it mixes with the radiative mode.

The latter can be repaired though. The condition for the existence of a BIC state in a 'static' system can be generalized to a dynamical system, where the resonance frequencies of the cavity modes are time-modulated in a specific way. This dynamic BIC state does not decay into the output ports.

When both a bright and a dark mode are simultaneously excited, these modes decay at different rates, dictated by the value of the imaginary part of the Floquet eigenfrequency.

10

Conclusion and outlook

Throughout this thesis we studied the interaction of light, plasmonic modes and temporal modulation. In particular, we employed the versatile platform of graphene plasmonics that allows to dynamically change the material properties. We studied different types of plasmonic structures: single resonances, coupled cavities, multimode cavities and propagating graphene plasmons. This variety of time-modulated structures enables a wide range of physical phenomena, such as frequency comb generation, frequency conversion and dynamic bound states. For practical implementation, temporal modulation offers a promising alternative to magnetic and non-linear materials, leading towards a compact and efficient platform for novel phenomena and applications.

We started in Chapter 6 by studying the interaction of a plane wave with a time-modulated single-mode plasmonic cavity in graphene nanoribbons, which generates a frequency comb. The frequency separation between the frequency components of the comb is equal to the modulation frequency applied to the cavity. We first studied the static system with a CMT model. The parameters of this model were extracted from FEM simulations of the array (in the frequency domain), by fitting the transmission spectrum to the CMT prediction. We then used the CMT model in the time domain, where the resonance frequency of the cavity was modulated. We found a good agreement between the dynamic CMT model and time domain FEM simulations, proving that a simple CMT model can describe the complex interplay

between light, plasmonic resonances and time modulation. Using the time domain CMT model, we discussed the parameters that influence the shape of the comb, and investigated the cavity dynamics. It was determined that the ribbon architecture can be much more efficient for comb generation than the previously reported planar graphene device.

In Chapter 7 we studied the behaviour of graphene plasmons incident on a time boundary, a sudden change in the graphene conductivity. At such a temporal interface the material properties change everywhere at the same time, so the field profile and the wavevector of the propagating modes is conserved, which implies that the frequency changes. We compared different modeling approaches in the literature and discussed their scope of application. We derived the reflection and transmission coefficients at a time interface for several types of interfaces (upward and downward steps and slabs). We also compared our results with time domain FEM simulations and found a good agreement between the theoretical predictions and the simulation results.

Next in Chapter 8, we extended the work of Chapter 6 by considering a system of two time-modulated cavities. This time, instead of frequency comb generation, we focused on frequency conversion. To this end, we studied figures of merit characterizing the conversion efficiency, as a function of the coupling between the two cavities. We also determined the Floquet modes of the dynamic system, as they play an important role in the frequency conversion process. We presented a method to determine the eigenfrequencies of the Floquet modes, and a perturbation technique to get an analytical expression for the Floquet branches. We also used a simple three-frequency model to investigate the interferences between the cavity modes, explaining why the conversion process is more efficient in some specific cases. Interestingly, we showed that the conversion efficiency is maximum at the edge of the anti-crossings opened by the time modulation in the Floquet diagrams, so that a single output frequency can be targeted.

Finally, in Chapter 9, we studied in more detail the decay mechanisms of Floquet modes in a multimode time-modulated cavity. Such a system with two static cavities can exhibit bound states in the continuum, modes that do not decay even if they lie in a continuum of radiation states. We reviewed the conditions for such bound states to exist, involving the coupling, decay rate and resonance frequencies of the modes. We then showed that these states can persist in a system with a particular modulation for both modes. We studied the losses of the Floquet modes in the general case, and found that the two different Floquet branches have very different decay rates. We verified that the bound states do not decay even in the presence of a time modulation by using a time-dependent CMT model.

A very important follow up to these theoretical propositions would be an experimental implementation. To this end, the graphene platform employed throughout this thesis is ideal for several reasons. The graphene Fermi level can be changed at GHz rates, and permits shifts in the resonance frequency of graphene plasmonic resonances of the order of THz. The frequency of operation is in the plasmonic regime of graphene, which ranges from mid-infrared to far-infrared. The initial resonance frequency can be tuned by using ribbon lengths ranging from hundreds of nanometers to micrometers, covering the mid-infrared to far-infrared ranges. The

initial Fermi level of graphene also allows to tune the initial resonance frequency of the plasmonic mode. Typical values for the Fermi level range from 0 to 1 eV. All these experimental parameters are already available in today's technology.

The main advantage of the time-modulation approach presented in this thesis is its tunability: both the graphene and the time modulation allow for a wide range of degrees of freedom. The use of plasmonic resonances also allows to interact very strongly with light, and to apply the time-modulation to a volume limited to the area where the plasmonic mode is supported. Even though graphene seems an ideal platform to implement time-dependent effects, the same analysis can be carried out for other types of resonances and time-dependent materials. For example lithium niobate has been used for a long time as electro-optic modulators in silicon photonics, and could be used to implement time-modulated effects on that platform.

Limitations to this approach also exist. For example it can be difficult to modulate the graphene Fermi-level at rates higher than tens of GHz by electrical gating. To lift this limitation, one needs to use fast pulsed lasers at optical frequencies, but the modulation of graphene at these rates remains a challenge. Moreover, losses in graphene have been an important limiting factor for graphene plasmonics since its early developments. This is expected to limit the performance of comb generation and frequency conversion presented in this thesis, as they decrease the quality factor of the graphene plasmonic resonance. The experimental realization of the ideas presented in this thesis thus remains a challenge, but also an important opportunity to achieve photonics effects that previously required non-linear or magnetic materials.

Potential applications range from direct implementation of frequency comb generation and frequency conversion using time-modulated graphene plasmonic resonances to more involved ones. For example the time-modulated BIC states could be used to realize lasers, as they have a theoretically infinite lifetime. These lasers could actually produce frequency combs as the Floquet modes present in this setup are separated by the modulation frequency. One other application would be tunable lasers that use the interferences between Floquet modes, as used in the thesis for frequency conversion.

Since the physical principles used here are very general, the results obtained in this thesis could be transposed to different fields. One can mention acoustics, where the resonance of a cavity can be mechanically modulated. These results offer a new indication that time-modulation could be an alternative to the use of non-linear and magnetic materials to achieve diverse optical effects. Even if challenging, the use of graphene plasmonics to this end is a promising platform. The generality of results obtained with time-modulation indicates that we could see time-modulated devices in very different fields in the years to come.

Bibliography

[1] M. M. Waldrop, "The chips are down for moore's law," *Nature*, vol. 530, pp. 144–147, 2016.

[2] B. Raghavan and J. Ma, "The energy and emergy of the internet," in *Proceedings of the 10th ACM Workshop on Hot Topics in Networks*, HotNets-X, (New York, NY, USA), pp. 9:1–9:6, ACM, 2011.

[3] D. Jalas, A. Petrov, M. Eich, W. Freude, S. Fan, Z. Yu, R. Baets, M. Popović, A. Melloni, J. D. Joannopoulos, and et al., "What is and what is not an optical isolator," *Nature Photonics*, vol. 7, no. 8, pp. 579–582, 2013.

[4] D. L. Sounas and A. Alu, "Non-reciprocal photonics based on time modulation," *Nature Photonics*, vol. 11, no. 12, pp. 774–783, 2017.

[5] S. A. Maier, *Plasmonics: Fundamentals and Applications*. Springer US, 2007.

[6] Y. Wei, H. Ebendorff-Heidepriem, and J. T. Zhao, "Recent advances in hybrid optical materials: Integrating nanoparticles within a glass matrix," *Advanced Optical Materials*, vol. 0, no. 0, p. 1900702, 2019.

[7] J. Homola, S. S. Yee, and G. Gauglitz, "Surface plasmon resonance sensors: review," *Sensors and Actuators B: Chemical*, vol. 54, no. 1, pp. 3–15, 1999.

[8] L. Liu, Z. Han, and S. He, "Novel surface plasmon waveguide for high integration," *Optics Express*, vol. 13, no. 17, pp. 6645–6650, 2005.

[9] M. Jablan, H. Buljan, and M. Soljacic, "Plasmonics in graphene at infrared frequencies," *Physical Review B*, vol. 80, p. 245435, 2009.

[10] G. Altares Menendez and B. Maes, "Frequency comb generation using plasmonic resonances in a time-dependent graphene ribbon array," *Physical Review B*, vol. 95, p. 144307, 2017.

[11] G. Altares Menendez and B. Maes, "Time reflection and refraction of graphene plasmons at a temporal discontinuity," *Optics Letters*, vol. 42, no. 23, pp. 5006–5009, 2017.

[12] H. Fukuda, K. Yamada, T. Shoji, M. Takahashi, T. Tsuchizawa, T. Watanabe, J. Takahashi, and S. Itabashi, "Four-wave mixing in silicon wire waveguides," *Optics Express*, vol. 13, no. 12, pp. 4629–4637, 2005.

[13] Q. Xu, V. R. Almeida, and M. Lipson, "Micrometer-scale all-optical wavelength converter on silicon," *Optics Letters*, vol. 30, no. 20, pp. 2733–2735, 2005.

[14] M. Skorobogatiy and J. D. Joannopoulos, "Rigid vibrations of a photonic crystal and induced interband transitions," *Physical Review B*, vol. 61, pp. 5293–5302, 2000.

[15] E. J. Reed, M. Soljačić, and J. D. Joannopoulos, "Reversed doppler effect in photonic crystals," *Physical Review Letters*, vol. 91, p. 133901, 2003.

[16] M. Notomi and S. Mitsugi, "Wavelength conversion via dynamic refractive index tuning of a cavity," *Physical Review A*, vol. 73, p. 051803, 2006.

[17] M. Notomi, H. Taniyama, S. Mitsugi, and E. Kuramochi, "Optomechanical wavelength and energy conversion in high-Q double-layer cavities of photonic crystal slabs," *Physical Review Letters*, vol. 97, no. 2, 2006.

[18] S. F. Preble, Q. Xu, and M. Lipson, "Changing the colour of light in a silicon resonator," *Nature Photonics*, vol. 1, no. 5, pp. 293–296, 2007.

[19] R. A. Soref and B. R. Bennett, "Kramers-kronig analysis of electro-optical switching in silicon," *Proceedings SPIE0704 Integrated Optical Circuit Engineering IV*, vol. Proc. SPIE 0704, 1987.

[20] T. Kampfrath, D. M. Beggs, T. P. White, A. Melloni, T. F. Krauss, and L. Kuipers, "Ultrafast adiabatic manipulation of slow light in a photonic crystal," *Physical Review A*, vol. 81, no. 4, p. 043837, 2010.

[21] D. M. Beggs, T. F. Krauss, L. Kuipers, and T. Kampfrath, "Ultrafast tilting of the dispersion of a photonic crystal and adiabatic spectral compression of light pulses," *Physical Review Letters*, vol. 108, no. 3, p. 033902, 2012.

[22] H. W. Tan, H. M. van Driel, S. L. Schweizer, and R. B. Wehrspohn, "Influence of eigenmode characteristics on optical tuning of a two-dimensional silicon photonic crystal," *Physical Review B*, vol. 72, no. 16, p. 165115, 2005.

[23] M. Castellanos Munoz, A. Y. Petrov, L. O'Faolain, J. Li, T. F. Krauss, and M. Eich, "Optically induced indirect photonic transitions in a slow light photonic crystal waveguide," *Physical Review Letters*, vol. 112, no. 5, 2014.

[24] D. M. Beggs, I. H. Rey, T. Kampfrath, N. Rotenberg, L. Kuipers, and T. F. Krauss, "Ultrafast tunable optical delay line based on indirect photonic transitions," *Physical Review Letters*, vol. 108, no. 21, p. 213901, 2012.

[25] R. Fleury, D. L. Sounas, C. F. Sieck, M. R. Haberman, and A. Alu, "Sound isolation and giant linear nonreciprocity in a compact acoustic circulator," *Science*, vol. 343, no. 6170, pp. 516–519, 2014.

[26] Z. Yu and S. Fan, "Complete optical isolation created by indirect interband photonic transitions," *Nature Photonics*, vol. 3, no. 2, pp. 91–94, 2009.

[27] D. L. Sounas, C. Caloz, and A. Alu, "Giant non-reciprocity at the subwavelength scale using angular momentum-biased metamaterials," *Nature Communications*, vol. 4, p. 2407, 2013.

[28] H. Lira, Z. Yu, S. Fan, and M. Lipson, "Electrically driven nonreciprocity induced by interband photonic transition on a silicon chip," *Physical Review Letters*, vol. 109, p. 033901, 2012.

[29] K. Gallo, G. Assanto, K. R. Parameswaran, and M. M. Fejer, "All-optical diode in a periodically poled lithium niobate waveguide," *Applied Physics Letters*, vol. 79, no. 3, pp. 314–316, 2001.

[30] M. Soljacic, C. Luo, J. D. Joannopoulos, and S. Fan, "Nonlinear photonic crystal microdevices for optical integration," *Optics Letters*, vol. 28, no. 8, pp. 637–639, 2003.

[31] Y. Shi, Z. Yu, and S. Fan, "Limitations of nonlinear optical isolators due to dynamic reciprocity," *Nature Photonics*, vol. 9, p. 388, 2015.

[32] D. Correas-Serrano, J. S. Gomez-Diaz, D. L. Sounas, Y. Hadad, A. Alvarez-Melcon, and A. Alu, "Nonreciprocal graphene devices and antennas based on spatiotemporal modulation," *IEEE Antennas and Wireless Propagation Letters*, vol. 15, pp. 1529–1532, 2016.

[33] B. Wang, J. Teng, and X. Yuan, "Inelastic scattering of surface plasmons in oscillating metallic waveguides," *Applied Physics Letters*, vol. 98, no. 26, p. 263111, 2011.

[34] C. Ruppert, F. Förster, A. Zrenner, J. B. Kinzel, A. Wixforth, H. J. Krenner, and M. Betz, "Radio frequency electromechanical control over a surface plasmon polariton coupler," *ACS Photonics*, vol. 1, no. 2, pp. 91–95, 2014.

[35] L. Lu, J. D. Joannopoulos, and M. Soljacic, "Topological photonics," *Nature Photonics*, vol. 8, no. 11, pp. 821–829, 2014.

[36] Z. Wang, Y. Chong, J. D. Joannopoulos, and M. Soljacic, "Observation of unidirectional backscattering-immune topological electromagnetic states," *Nature*, vol. 461, no. 7265, pp. 772–775, 2009.

[37] K. Fang, Z. Yu, and S. Fan, "Realizing effective magnetic field for photons by controlling the phase of dynamic modulation," *Nature Photonics*, vol. 6, no. 11, pp. 782–787, 2012.

[38] A. B. Khanikaev, S. Hossein Mousavi, W.-K. Tse, M. Kargarian, A. H. MacDonald, and G. Shvets, "Photonic topological insulators," *Nature Materials*, vol. 12, no. 3, pp. 233–239, 2012.

[39] R. R. Nair, P. Blake, A. N. Grigorenko, K. S. Novoselov, T. J. Booth, T. Stauber, N. M. R. Peres, and A. K. Geim, "Fine structure constant defines visual transparency of graphene," *Science*, vol. 320, no. 5881, pp. 1308–1308, 2008.

[40] L. A. Falkovsky and A. A. Varlamov, "Space-time dispersion of graphene conductivity," *The European Physical Journal B*, vol. 56, no. 4, pp. 281–284, 2007.

[41] L. A. Falkovsky, "Optical properties of graphene," *Journal of Physics: Conference Series*, vol. 129, p. 012004, 2008.

[42] H. Liu, Y. Liu, and D. Zhu, "Chemical doping of graphene," *Journal of Materials Chemistry*, vol. 21, pp. 3335–3345, 2011.

[43] J. Ristein, "Surface transfer doping of semiconductors," *Science*, vol. 313, no. 5790, p. 1057, 2006.

[44] F. Schedin, A. K. Geim, S. V. Morozov, E. W. Hill, P. Blake, M. I. Katsnelson, and K. S. Novoselov, "Detection of individual gas molecules adsorbed on graphene," *Nature Materials*, vol. 6, p. 652, 2007.

[45] T. O. Wehling, K. S. Novoselov, S. V. Morozov, E. E. Vdovin, M. I. Katsnelson, A. K. Geim, and A. I. Lichtenstein, "Molecular doping of graphene," *Nano Letters*, vol. 8, no. 1, pp. 173–177, 2008.

[46] B. Guo, Q. Liu, E. Chen, H. Zhu, L. Fang, and J. R. Gong, "Controllable n-doping of graphene," *Nano Letters*, vol. 10, no. 12, pp. 4975–4980, 2010.

[47] K. S. Novoselov, A. K. Geim, S. V. Morozov, D. Jiang, Y. Zhang, S. V. Dubonos, I. V. Grigorieva, and A. A. Firsov, "Electric field effect in atomically thin carbon films," *Science*, vol. 306, no. 5696, pp. 666–669, 2004.

[48] L. Ren, Q. Zhang, J. Yao, Z. Sun, R. Kaneko, Z. Yan, S. Nanot, Z. Jin, I. Kawayama, M. Tonouchi, J. M. Tour, and J. Kono, "Terahertz and infrared spectroscopy of gated large-area graphene," *Nano Letters*, vol. 12, no. 7, p. 3711, 2012.

[49] F. Wang, Y. Zhang, C. Tian, C. Girit, A. Zettl, M. Crommie, and Y. R. Shen, "Gate-variable optical transitions in graphene," *Science*, vol. 320, no. 5873, pp. 206–209, 2008.

[50] X. Gan, R.-J. Shiue, Y. Gao, K. F. Mak, X. Yao, L. Li, A. Szep, D. Walker, J. Hone, T. F. Heinz, and et al., "High-contrast electrooptic modulation of a photonic crystal nanocavity by electrical gating of graphene," *Nano Letters*, vol. 13, no. 2, p. 691–696, 2013.

[51] C. T. Phare, Y. Daniel Lee, J. Cardenas, and M. Lipson, "Graphene electro-optic modulator with 30 GHz bandwidth," *Nature Photonics*, vol. 9, no. 8, pp. 511–514, 2015.

[52] C.-F. Chen, C.-H. Park, B. W. Boudouris, J. Horng, B. Geng, C. Girit, A. Zettl, M. F. Crommie, R. A. Segalman, S. G. Louie, and F. Wang, "Controlling inelastic light scattering quantum pathways in graphene," *Nature*, vol. 471, p. 617, 2011.

[53] Z. Fang, S. Thongrattanasiri, A. Schlather, Z. Liu, L. Ma, Y. Wang, P. M. Ajayan, P. Nordlander, N. J. Halas, and F. J. García de Abajo, "Gated tunability and hybridization of localized plasmons in nanostructured graphene," *ACS Nano*, vol. 7, no. 3, pp. 2388–2395, 2013.

[54] P. A. George, J. Strait, J. Dawlaty, S. Shivaraman, M. Chandrashekhar, F. Rana, and M. G. Spencer, "Ultrafast optical-pump terahertz-probe spectroscopy of the carrier relaxation and recombination dynamics in epitaxial graphene," *Nano Letters*, vol. 8, no. 12, pp. 4248–4251, 2008.

[55] D. K. Efetov and P. Kim, "Controlling electron-phonon interactions in graphene at ultrahigh carrier densities," *Physical Review Letters*, vol. 105, no. 25, p. 256805, 2010.

[56] T. Li, L. Luo, M. Hupalo, J. Zhang, M. C. Tringides, J. Schmalian, and J. Wang, "Femtosecond population inversion and stimulated emission of dense dirac fermions in graphene," *Physical Review Letters*, vol. 108, no. 16, p. 167401, 2012.

[57] M. Trushin, A. Grupp, G. Soavi, A. Budweg, D. De Fazio, U. Sassi, A. Lombardo, A. C. Ferrari, W. Belzig, A. Leitenstorfer, and D. Brida, "Ultrafast pseudospin dynamics in graphene," *Physical Review B*, vol. 92, no. 16, p. 165429, 2015.

[58] J. C. Johannsen, S. Ulstrup, F. Cilento, A. Crepaldi, M. Zacchigna, C. Cacho, I. C. E. Turcu, E. Springate, F. Fromm, C. Raidel, T. Seyller, F. Parmigiani, M. Grioni, and P. Hofmann, "Direct view of hot carrier dynamics in graphene," *Physical Review Letters*, vol. 111, no. 2, p. 027403, 2013.

[59] I. Gierz, J. C. Petersen, M. Mitrano, C. Cacho, I. C. E. Turcu, E. Springate, A. Stohr, A. Kohler, U. Starke, and A. Cavalleri, "Snapshots of nonequilibrium dirac carrier distributions in graphene," *Nature Materials*, vol. 12, p. 1119, 2013.

[60] S. Ulstrup, J. C. Johannsen, F. Cilento, J. A. Miwa, A. Crepaldi, M. Zacchigna, C. Cacho, R. Chapman, E. Springate, S. Mammadov, F. Fromm, C. Raidel, T. Seyller, F. Parmigiani, M. Grioni, P. D. C. King, and P. Hofmann, "Ultrafast dynamics of massive dirac fermions in bilayer graphene," *Physical Review Letters*, vol. 112, no. 25, p. 257401, 2014.

[61] G. Rohde, A. Stange, A. Muller, M. Behrendt, L.-P. Oloff, K. Hanff, T. J. Albert, P. Hein, K. Rossnagel, and M. Bauer, "Ultrafast formation of a fermidirac distributed electron gas," *Physical Review Letters*, vol. 121, no. 25, p. 256401, 2018.

[62] S. Bae, H. Kim, Y. Lee, X. Xu, J.-S. Park, Y. Zheng, J. Balakrishnan, T. Lei, H. Ri Kim, Y. I. Song, Y.-J. Kim, K. S. Kim, B. Ozyilmaz, J.-H. Ahn, B. H. Hong, and S. Iijima, "Roll-to-roll production of 30-inch graphene films for transparent electrodes," *Nature Nanotechnology*, vol. 5, p. 574, 2010.

[63] Y. Zhang, L. Gomez, F. N. Ishikawa, A. Madaria, K. Ryu, C. Wang, A. Badmaev, and C. Zhou, "Comparison of graphene growth on single-crystalline and polycrystalline ni by chemical vapor deposition," *Journal of Physical Chemistry Letters*, vol. 1, no. 20, pp. 3101–3107, 2010.

[64] X. Li, W. Cai, J. An, S. Kim, J. Nah, D. Yang, R. Piner, A. Velamakanni, I. Jung, E. Tutuc, S. K. Banerjee, L. Colombo, and R. S. Ruoff, "Large-area synthesis of high-quality and uniform graphene films on copper foils," *Science*, vol. 324, no. 5932, p. 1312, 2009.

[65] A. N. Abbas, G. Liu, B. Liu, L. Zhang, H. Liu, D. Ohlberg, W. Wu, and C. Zhou, "Patterning, characterization, and chemical sensing applications of graphene nanoribbon arrays down to 5 nm using helium ion beam lithography," *ACS Nano*, vol. 8, no. 2, pp. 1538–1546, 2014.

[66] S. Ryu, J. Maultzsch, M. Y. Han, P. Kim, and L. E. Brus, "Raman spectroscopy of lithographically patterned graphene nanoribbons," *ACS Nano*, vol. 5, no. 5, pp. 4123–4130, 2011.

[67] V. Sidorkin, E. van Veldhoven, E. van der Drift, P. Alkemade, H. Salemink, and D. Maas, "Sub-10-nm nanolithography with a scanning helium beam," *Journal of Vacuum Science & Technology B: Microelectronics and Nanometer Structures Processing, Measurement, and Phenomena*, vol. 27, no. 4, p. 18, 2009.

[68] M. C. Lemme, D. C. Bell, J. R. Williams, L. A. Stern, B. W. H. Baugher, P. Jarillo-Herrero, and C. M. Marcus, "Etching of graphene devices with a helium ion beam," *ACS Nano*, vol. 3, no. 9, pp. 2674–2676, 2009.

[69] D. C. Bell, M. C. Lemme, L. A. Stern, J. R. Williams, and C. M. Marcus, "Precision cutting and patterning of graphene with helium ions," *Nanotechnology*, vol. 20, no. 45, p. 455301, 2009.

[70] L. Novotny, *Principles of Nano-Optics*. Cambridge University Press, 2006.

[71] Y. V. Bludov, A. Ferreira, N. M. R. Peres, and M. I. Vasilevskiy, "A primer on surface plasmon-polaritons in graphene," *International Journal of Modern Physics B*, vol. 27, no. 10, p. 1341001, 2013.

[72] A. Marini, I. Silveiro, and F. J. Garcia de Abajo, "Molecular sensing with tunable graphene plasmons," *ACS Photonics*, vol. 2, no. 7, pp. 876–882, 2015.

[73] D. Rodrigo, O. Limaj, D. Janner, D. Etezadi, F. J. Garcia de Abajo, V. Pruneri, and H. Altug, "Mid-infrared plasmonic biosensing with graphene," *Science*, vol. 349, no. 6244, p. 165, 2015.

[74] A. Y. Nikitin, F. Guinea, F. J. Garcia-Vidal, and L. Martin-Moreno, "Surface plasmon enhanced absorption and suppressed transmission in periodic arrays of graphene ribbons," *Physical Review B*, vol. 85, p. 081405, 2012.

[75] S. Thongrattanasiri, F. H. L. Koppens, and F. J. Garcia de Abajo, "Complete optical absorption in periodically patterned graphene," *Physical Review Letters*, vol. 108, p. 047401, 2012.

[76] L. Ju, B. Geng, J. Horng, C. Girit, M. Martin, Z. Hao, H. A. Bechtel, X. Liang, A. Zettl, Y. R. Shen, and F. Wang, "Graphene plasmonics for tunable terahertz metamaterials," *Nature Nanotechnology*, vol. 6, no. 10, pp. 630–634, 2011.

[77] J. L. Garcia-Pomar, A. Y. Nikitin, and L. Martin-Moreno, "Scattering of graphene plasmons by defects in the graphene sheet," *ACS Nano*, vol. 7, no. 6, pp. 4988–4994, 2013.

[78] J. Chen, M. L. Nesterov, A. Y. Nikitin, S. Thongrattanasiri, P. Alonso-González, T. M. Slipchenko, F. Speck, M. Ostler, T. Seyller, I. Crassee, F. H. L. Koppens, L. Martin-Moreno, F. J. García de Abajo, A. B. Kuzmenko, and R. Hillenbrand, "Strong plasmon reflection at nanometer-size gaps in monolayer graphene on sic," *Nano Letters*, vol. 13, no. 12, pp. 6210–6215, 2013.

[79] A. Y. Nikitin, T. Low, and L. Martin-Moreno, "Anomalous reflection phase of graphene plasmons and its influence on resonators," *Physical Review B*, vol. 90, no. 4, p. 041407, 2014.

[80] J. D. Joannopoulos, S. G. Johnson, J. N. Winn, and R. D. Meade, *Photonic crystals: Molding the flow of light.* Photonic Crystals: Molding the Flow of Light (Second Edition), Princeton University Press, 2008.

[81] H. A. Haus, *Waves and Fields in Optoelectronics.* Prentice Hall, 1983.

[82] S. Fan, W. Suh, and J. D. Joannopoulos, "Temporal coupled-mode theory for the fano resonance in optical resonators," *Journal of the Optical Society of America A*, vol. 20, no. 3, p. 569, 2003.

[83] Z. Yu, A. Raman, and S. Fan, "Fundamental limit of nanophotonic light trapping in solar cells," *Proceedings of the National Academy of Sciences*, vol. 107, no. 41, pp. 17491–17496, 2010.

[84] W. Suh, Z. Wang, and S. Fan, "Temporal coupled-mode theory and the presence of non-orthogonal modes in lossless multimode cavities," *IEEE Journal of Quantum Electronics*, vol. 40, no. 10, pp. 1511–1518, 2004.

[85] U. Fano, "Effects of configuration interaction on intensities and phase shifts," *Physical Review*, vol. 124, no. 6, pp. 1866–1878, 1961.

[86] U. Fano, "Sullo spettro di assorbimento dei gas nobili presso il limite dello spettro d'arco," *Il Nuovo Cimento (1924-1942)*, vol. 12, no. 3, pp. 154–161, 1935.

[87] M. F. Limonov, M. V. Rybin, A. N. Poddubny, and Y. S. Kivshar, "Fano resonances in photonics," *Nature Photonics*, vol. 11, p. 543, 2017.

[88] M. I. Tribelsky and A. E. Miroshnichenko, "Giant in-particle field concentration and fano resonances at light scattering by high-refractive-index particles," *Physical Review A*, vol. 93, no. 5, p. 053837, 2016.

[89] M. V. Rybin, K. B. Samusev, I. S. Sinev, G. Semouchkin, E. Semouchkina, Y. S. Kivshar, and M. F. Limonov, "Mie scattering as a cascade of fano resonances," *Optics Express*, vol. 21, no. 24, pp. 30107–30113, 2013.

[90] A. N. Poddubny, M. V. Rybin, M. F. Limonov, and Y. S. Kivshar, "Fano interference governs wave transport in disordered systems," *Nature Communications*, vol. 3, p. 914, 2012.

[91] S. Fan, "Sharp asymmetric line shapes in side-coupled waveguide-cavity systems," *Applied Physics Letters*, vol. 80, no. 6, pp. 908–910, 2002.

[92] P. Yu, T. Hu, H. Qiu, F. Ge, H. Yu, X. Jiang, and J. Yang, "Fano resonances in ultracompact waveguide fabry-perot resonator side-coupled lossy nanobeam cavities," *Applied Physics Letters*, vol. 103, no. 9, p. 091104, 2013.

[93] J. H. Shirley, *Interaction of a Quantum System with a Strong Oscillating Field*. PhD thesis, California Institute of Technology, 1963.

[94] J. H. Shirley, "Solution of the schrödinger equation with a hamiltonian periodic in time," *Physical Review*, vol. 138, pp. B979–B987, 1965.

[95] Comsol AB, "Comsol Multiphysics v 5.2." www.comsol.com.

[96] A. C. Polycarpou, "Introduction to the finite element method in electromagnetics," *Synthesis Lectures on Computational Electromagnetics*, vol. 1, no. 1, pp. 1–126, 2006.

[97] A. N. Grigorenko, M. Polini, and K. S. Novoselov, "Graphene plasmonics," *Nature Photonics*, vol. 6, no. 11, pp. 749–758, 2012.

[98] P. Tassin, T. Koschny, M. Kafesaki, and C. M. Soukoulis, "A comparison of graphene, superconductors and metals as conductors for metamaterials and plasmonics," *Nature Photonics*, vol. 6, no. 4, pp. 259–264, 2012.

[99] F. J. Garcia de Abajo, "Graphene plasmonics: Challenges and opportunities," *ACS Photonics*, vol. 1, no. 3, pp. 135–152, 2014.

[100] G. Rosolen and B. Maes, "Graphene ribbons for tunable coupling with plasmonic subwavelength cavities," *Journal of the Optical Society of America B*, vol. 31, no. 5, pp. 1096–1102, 2014.

[101] M. T. Wade, X. Zeng, and M. A. Popovic, "Wavelength conversion in modulated coupled-resonator systems and their design via an equivalent linear filter representation," *Optics Letters*, vol. 40, no. 1, pp. 107–110, 2015.

[102] K. Fang, Z. Yu, and S. Fan, "Photonic aharonov-bohm effect based on dynamic modulation," *Physical Review Letters*, vol. 108, p. 153901, 2012.

[103] M. Zhang, B. Buscaino, C. Wang, A. Shams-Ansari, C. Reimer, R. Zhu, J. M. Kahn, and M. Lonar, "Broadband electro-optic frequency comb generation in a lithium niobate microring resonator," *Nature*, vol. 568, no. 7752, pp. 373–377, 2019.

[104] A. Rueda, F. Sedlmeir, M. Kumari, G. Leuchs, and H. G. L. Schwefel, "Resonant electro-optic frequency comb," *Nature*, vol. 568, no. 7752, pp. 378–381, 2019.

[105] Y. Hadad, D. L. Sounas, and A. Alu, "Space-time gradient metasurfaces," *Physical Review B*, vol. 92, p. 100304, 2015.

[106] V. Ginis, P. Tassin, T. Koschny, and C. M. Soukoulis, "Tunable terahertz frequency comb generation using time-dependent graphene sheets," *Physical Review B*, vol. 91, p. 161403, 2015.

[107] T. Low and P. Avouris, "Graphene plasmonics for terahertz to mid-infrared applications," *ACS Nano*, vol. 8, no. 2, p. 1086, 2014.

[108] A. E. Miroshnichenko, S. Flach, and Y. S. Kivshar, "Fano resonances in nanoscale structures," *Reviews of Modern Physics*, vol. 82, no. 3, pp. 2257–2298, 2010.

[109] W. M. Robertson, G. Arjavalingam, R. D. Meade, K. D. Brommer, A. M. Rappe, and J. D. Joannopoulos, "Measurement of photonic band structure in a two-dimensional periodic dielectric array," *Physical Review Letters*, vol. 68, no. 13, pp. 2023–2026, 1992.

[110] M. Merano, "Fresnel coefficients of a two-dimensional atomic crystal," *Physical Review A*, vol. 93, p. 013832, 2016.

[111] N. K. Emani, T. Chung, X. Ni, A. V. Kildishev, Y. P. Chen, and A. Boltasseva, "Electrically tunable damping of plasmonic resonances with graphene," *Nano Letters*, vol. 12, no. 10, pp. 5202–5206, 2012.

[112] F. Morgenthaler, "Velocity modulation of electromagnetic waves," *IEEE Transactions on Microwave Theory and Techniques*, vol. 6, no. 2, p. 167, 1958.

[113] Y. Sivan and J. B. Pendry, "Time reversal in dynamically tuned zero-gap periodic systems," *Physical Review Letters*, vol. 106, p. 193902, 2011.

[114] M. I. Bakunov, A. V. Maslov, and S. B. Bodrov, "Splitting and radiation of a surface plasmon by resonant ionization in a thin semiconductor coating," *Journal of the Optical Society of America B*, vol. 18, no. 8, pp. 1180–1188, 2001.

[115] V. Bacot, M. Labousse, A. Eddi, M. Fink, and E. Fort, "Time reversal and holography with spacetime transformations," *Nature Physics*, vol. 12, no. 10, p. 972–977, 2016.

[116] J. Wilson, F. Santosa, M. Min, and T. Low, "Temporal control of graphene plasmons," *Physical Review B*, vol. 98, no. 8, p. 081411, 2018.

[117] A. Maslov and M. Bakunov, "Temporal scattering of a graphene plasmon by a rapid carrier density decrease," *Optica*, vol. 5, no. 12, pp. 1508–1515, 2018.

[118] J. T. Mendoça and P. K. Shukla, "Time refraction and time reflection: Two basic concepts," *Physica Scripta*, vol. 65, no. 2, p. 160, 2002.

[119] Q. H. Wang, K. Kalantar-Zadeh, A. Kis, J. N. Coleman, and M. S. Strano, "Electronics and optoelectronics of two-dimensional transition metal dichalcogenides," *Nature Nanotechnology*, vol. 7, no. 11, pp. 699–712, 2012.

[120] M. Minkov, Y. Shi, and S. Fan, "Exact solution to the steady-state dynamics of a periodically modulated resonator," *APL Photonics*, vol. 2, no. 7, p. 076101, 2017.

[121] T. J. Kippenberg, R. Holzwarth, and S. A. Diddams, "Microresonator-based optical frequency combs," *Science*, vol. 332, no. 6029, p. 555, 2011.

[122] X. Liu, B. Kuyken, G. Roelkens, R. Baets, R. M. Osgood Jr, and W. M. J. Green, "Bridging the mid-infrared-to-telecom gap with silicon nanophotonic spectral translation," *Nature Photonics*, vol. 6, p. 667, 2012.

[123] P. Del'Haye, A. Schliesser, O. Arcizet, T. Wilken, R. Holzwarth, and T. J. Kippenberg, "Optical frequency comb generation from a monolithic microresonator," *Nature*, vol. 450, p. 1214, 2007.

[124] B. Kuyken, T. Ideguchi, S. Holzner, M. Yan, T. W. Hansch, J. Van Campenhout, P. Verheyen, S. Coen, F. Leo, R. Baets, G. Roelkens, and N. Picqué, "An octave-spanning mid-infrared frequency comb generated in a silicon nanophotonic wire waveguide," *Nature Communications*, vol. 6, p. 6310, 2015.

[125] A. Pick, Z. Lin, W. Jin, and A. W. Rodriguez, "Enhanced nonlinear frequency conversion and purcell enhancement at exceptional points," *Physical Review B*, vol. 96, p. 224303, 2017.

[126] D. K. Kalluri, *Electromagnetics of Time Varying Complex Media: Frequency and Polarization, Second Edition.* CRC Press, 2010.

[127] N. Wang, Z.-Q. Zhang, and C. T. Chan, "Photonic floquet media with a complex time-periodic permittivity," *Physical Review B*, vol. 98, no. 8, p. 085142, 2018.

[128] H. Salwen, "Resonance transitions in molecular beam experiments. i. general theory of transitions in a rotating magnetic field," *Physical Review*, vol. 99, pp. 1274–1286, 1955.

[129] M. Zhang, C. Wang, Y. Hu, A. Shams-Ansari, T. Ren, S. Fan, and M. Lončar, "Electronically programmable photonic molecule," *Nature Photonics*, vol. 13, no. 1, pp. 36–40, 2019.

[130] C. W. Hsu, B. Zhen, A. D. Stone, J. D. Joannopoulos, and M. Soljacic, M., "Bound states in the continuum," *Nature Reviews Materials*, vol. 1, pp. 16048–, 2016.

[131] R. Parker, "Resonance effects in wake shedding from parallel plates: Some experimental observations," *Journal of Sound and Vibration*, vol. 4, no. 1, pp. 62–72, 1966.

[132] R. Parker, "Resonance in wake shedding from parallel plates: Calculation of resonant frequencies," *Journal of Sound and Vibration*, vol. 5, pp. 330–343, 1967.

[133] F. Ursell, "Trapping modes in the theory of surface waves," *Mathematical Proceedings of the Cambridge Philosophical Society*, vol. 47, no. 2, pp. 347–358, 1951.

[134] D. S. Jones, "The eigenvalues of $\nabla^2 u + \lambda u = 0$ when the boundary conditions are given on semi-infinite domains," *Mathematical Proceedings of the Cambridge Philosophical Society*, vol. 49, no. 4, pp. 668–684–, 1953.

[135] S. Longhi, "Transfer of light waves in optical waveguides via a continuum," *Physical Review A*, vol. 78, no. 1, p. 013815, 2008.

[136] F. Dreisow, A. Szameit, M. Heinrich, R. Keil, S. Nolte, A. Tünnermann, and S. Longhi, "Adiabatic transfer of light via a continuum in optical waveguides," *Optics Letters*, vol. 34, no. 16, pp. 2405–2407, 2009.

[137] Y. Plotnik, O. Peleg, F. Dreisow, M. Heinrich, S. Nolte, A. Szameit, and M. Segev, "Experimental observation of optical bound states in the continuum," *Physical Review Letters*, vol. 107, no. 18, p. 183901, 2011.

[138] M. McIver, "An example of non-uniqueness in the two-dimensional linear water wave problem," *Journal of Sound and Vibration*, vol. 315, pp. 257–266, 1996.

[139] C. Linton and P. McIver, "Embedded trapped modes in water waves and acoustics," *Wave Motion*, vol. 45, no. 1-2, pp. 16–29, 2007.

[140] K.-K. Voo, "Trapped electromagnetic modes in forked transmission lines," *Wave Motion*, vol. 45, no. 6, pp. 795–803, 2008.

[141] T. Lepetit, E. Akmansoy, J.-P. Ganne, and J.-M. Lourtioz, "Resonance continuum coupling in high-permittivity dielectric metamaterials," *Physical Review B*, vol. 82, no. 19, p. 195307, 2010.

[142] T. Lepetit and B. Kante, "Controlling multipolar radiation with symmetries for electromagnetic bound states in the continuum," *Physical Review B*, vol. 90, no. 24, p. 241103, 2014.

[143] C. M. Gentry and M. A. Popovic, "Dark state lasers," *Optics Letters*, vol. 39, no. 14, pp. 4136–4139, 2014.